Check for updates

Strategies for performance and stability advancement in multicomponent perovskite photovoltaics

Femi Igbari, [ID] * Muhammad Bilal [ID] and Zhe Li [ID] *

The unique photophysical properties of halide perovskites have placed them ahead of other photovoltaic (PV) materials in the areas of photoconversion efficiency (PCE) and energy level alignment with common contacts. The PCE is currently closing in on the predicted theoretical limit. However, the poor stability of this class of materials under ambient conditions is a drawback. It has limited the extensive exploitation of their properties and has slowed down their uptake in the global PV market. Notably, the unique properties have been attributed to the optimal orbital overlap between the lead cation (Pb^{2+}) and halide anion making up the inorganic framework of the crystal lattice. Although Pb is toxic, its presence is key to the unique opto-electronic properties of halide perovskites. Therefore, it must be retained while measures are taken to stabilize the lattice so as to suppress Pb leakage and the migration of other ionic components. One way to approach this is by multiple lattice site substitution which yields a multi-component perovskite (ABX_3) configuration, where the A-, B- and X-sites are occupied by more than one element which can synergistically compensate for the composition-induced instability through an increase in ion migration activation energy. The resulting multi-component perovskite (MCP) is commonly known as multi-cation mixed-halide perovskite. Therefore, in this review, we discuss the various approaches adopted recently to achieve higher stability in MCPs. The approaches are grouped into the focus areas of material identification, composition engineering, materials engineering, defect passivation, phase stabilization, photophysical property enhancement and device engineering. We discuss the challenges in stability evaluation of perovskite PV devices. Finally, we draw conclusions based on the various reports and give an outlook on pertinent research directions to further advance the PV applications of MCPs.

1 Introduction

Halide perovskites are known for their unique properties which include high optical absorption coefficients,[1] tunable bandgaps,[1–3] high carrier mobility,[4] long carrier diffusion lengths,[5] low exciton binding energies[6] and high photoluminescence (PL) quantum yield.[7] They have found applications in solar cells,[4,5,8–10] photodetectors,[11] light emitting

School of Engineering and Materials Science (SEMS), Queen Mary University of London, London, E1 4NS, UK. E-mail: o.igbari@qmul.ac.uk; zhe.li@qmul.ac.uk

Femi Igbari focuses on the understanding of reversible processes in multicomponent perovskites towards achieving sustainability in corresponding photovoltaic devices. This is a build-up on his previous work as a PhD Student and Researcher at Soochow University, Slovak Academy of Sciences and Polish Academy of Sciences. He is currently a UKRI Fellow at the School of Engineering and Materials Science, Queen Mary University of London. Femi is a recipient of the Horizon Europe Guarantee Funding having successfully applied for the Marie Sklodowska-Curie Actions Postdoctoral Fellowships. He has also previously attracted funding from the China Scholarship Council and the National Natural Science Foundation of China.

Femi Igbari

32964 | *J. Mater. Chem. A*, 2025, **13**, 32964–33011

This journal is © The Royal Society of Chemistry 2025

diodes,[12] lasers,[13] radiation sensors[14] etc. In particular, halide perovskite-based solar cells have attained an unprecedented photoconversion efficiency (PCE) of ca. 27% in just over a decade of their emergence.[15] This can be attributed to their fascinating photophysical properties coupled with strategic optimization measures such as composition, morphological, crystal phase, structural and interface engineering. Their PCE now rivals those based on silicon (Si) heterostructures. They have achieved this feat with easier, cost effective, more facile and industrially viable fabrication processes. Halide perovskites allow composition engineering which favors bandgap tunability from ca. 1.5 eV to ca. 3.2 eV, paving the way for their application as absorber layers in top and bottom sub-cells of an all-perovskite tandem solar cell.[16,17] The tandem structure yields efficiencies which surpass the Shockley–Queisser limit (33.7%) predicted for single junction solar cells.[18,19]

A halide perovskite lattice is represented as ABX_3. The A-site is occupied by monovalent organic cations such as methyl-ammonium (MA^+), formamidinium (FA^+), guanidinium (GA^+) etc. as well as monovalent inorganic cations such as cesium (Cs^+), rubidium (Rb^+), potassium (K^+) etc. Similarly, the B-site is occupied by divalent inorganic cations such as lead cation (Pb^{2+}) and tin cation (Sn^{2+}). The X-site is occupied by halides such as chloride (Cl^-), bromide (Br^-) or iodide (I^-). The B-site cation is octahedrally coordinated with 6 X-site halides to form a corner-sharing $[BX_6]^{4-}$ complex while the A-site cation occupies the cuboctahedral void formed by the corner-sharing $[BX_6]^{4-}$ complex and compensates the negative charge on the complex, stabilizing the resulting 3D perovskite lattice.[20] Due to the poor stability of halide perovskites, the lattice structural integrity can be easily compromised by intrinsic and extrinsic factors such as ion migration and moisture respectively, resulting in degradation and loss of photoactive properties. Incidentally, each lattice site can be occupied by more than one cation (A- and B-sites) and more than one halide (X-site) to form a multi-component perovskite (MCP) configuration commonly referred to as a multi-cation mixed-halide perovskite.[8–10,21,22] Such structures can be easily fabricated through post-synthetic lattice-site exchange or cross-exchange as well as through bottom-up synthetic processes where stoichiometric ratios of the precursor materials are reacted.[23,24]

The ease with which the components fit into their respective lattice sites to maintain the 3D perovskite structure integrity can be predicted by the Goldschmidt tolerance factor (t) obtainable from the equation $t = (r_A + r_X)/\sqrt{2}(r_B + r_X)$, where r_A, r_B and r_X are the ionic radii of the components of A-, B-, and X-sites, respectively.[25,26] For the 3D structure to be maintained, t must be close to unity, specifically in the range of $0.8 < t < 1.0$. Although t is effective in predicting the phase stability of various perovskite compositions, it is an empirical method. Hence, it has limitations as there are many other possible compositions beyond its scope, raising the need for an advanced, accurate and all-encompassing technique for stability prediction of the 3D perovskite structure. The inorganic octahedral metal-halide framework, made of the $[BX_6]^{4-}$ complex, is mainly responsible for the optoelectronic properties of perovskites while the A-site cation influences the stability and physicochemical properties.[27,28] Since the A-site cations form an ionic bond with the $[BX_6]^{4-}$ complex, they do not contribute states to the band edges. Such states result from the covalent bonding in the $[BX_6]^{4-}$ complex formed by the hybridization of the B-site and X-site orbitals.[26] Moreover, A-site cations can indirectly influence the perovskite band structure through the B–X bond length and angle changes, octahedral tilting and steric interactions. For example, the bandgap decreases when the smaller ionic radius Cs^+ is replaced with the larger ionic radius MA^+ due to a decrease in the Pb–X–Pb bond angle.[29]

Achieving an MCP favours improved material stability. Having more than one cation in the A-site creates synergistic compensations amongst the constituent cations by adjusting t to ensure the stable incorporation of ordinarily incompatible cations and to maintain the 3D structure. For instance, FA^+ is thermodynamically too large and should not fit into the cuboctahedral space at room temperature. Such incorporation should yield a non-photoactive phase. Moreover, mixing the FA^+ cations with other cations of different sizes and shapes favourably alters t and stabilizes the photoactive α-phase at room temperature.[30,31] Such lattice site composition changes to maintain a 3D perovskite structure are also evident in the X-site as t, which can be increased by the partial substitution of the larger FA^+ with a smaller cation such as MA^+, decreases after partially substituting the larger I^- with the smaller Br^- in the $(FAPbI_3)_{1−x}(MAPbBr_3)_x$ perovskite.[32,33] Hence, increases in t caused by the A-site substitutions can be compensated and brought within the ideal range by substitutions in the X-site, leading to the realization of 3D structural integrity in MCPs.

Beyond the empirical t, theoretical techniques to predict the stability of perovskites also exist. For example, Sun et al. searched for optimum MCP compositions to achieve decent stability against stressors through machine learning.[34] In particular, the expansion of compositional space through stability prediction using machine learning can be based on models predicting specific quantities such as the enthalpy of mixing and octahedral distortions from an extensive dataset of first-principles calculations validated by experimental results.[34–36] The prediction is independent of precursor material types or concentrations. Notably, both empirical and theoretical methods are limited when individually applied. The empirical methods can easily prove the feasibility of a given perovskite configuration albeit with low-throughput. Similarly, the theoretical method can predict a large number of possible configurations with high-throughput though it is unable to practically demonstrate their stability. Therefore, a combination of empirical and theoretical techniques capable of effectively leveraging on the high-throughput predictions and corresponding experimental proofs of concept cannot be over-emphasized in the determination of optimized perovskite compositions. In addition to the mixed A-site cations and X-site halides, mixed metal cations in the B-site and their influence on the perovskite opto-electronic properties and 3D structural stability have been explored.[37–44]

Notably, the need to achieve high stability of MCPs has been on the front burner recently owing to the goal of adequately exploiting their fascinating opto-electronic properties which is

This journal is © The Royal Society of Chemistry 2025

J. Mater. Chem. A, 2025, 13, 32964–33011 | 32965

limited by poor structural stability. Current research work has taken various approaches to extend the frontiers of knowledge relating to the stability of MCPs with focus on areas such as materials discovery and modification strategies.[45–47] These efforts have also paid attention to the behavior of this class of materials in the presence and absence of stressors such as temperature,[48–50] humidity,[50–52] oxygen[50] and light.[50,53–55] In particular, studies have revealed that MCPs are ionic materials and their degradation is directly related to stress-induced ion migration which must be suppressed to achieve highly functional materials and devices.[48–56] Burns $et\ al.$ demonstrated a reduction in the ion migration through a partial substitution of I^- with Cl^- in the X-site of the perovskite lattice.[57] A- and X-site substitutions of perovskite such as $FAPbI_3$ to achieve $Cs_{0.05}(FA_{0.83}MA_{0.17})_{0.95}Pb(I_{0.83}Br_{0.17})_3$ further revealed that an increase in the activation energies (E_a) of the mobile ions within the lattice is responsible for the suppression of ion migration,[22] suggesting the merits of multiple ion substitution on the degradation of halide perovskites. Furthermore, Yang $et\ al.$ showed the effectiveness of additives in ensuring high stability in solar cells based on MCPs.[58] The additives form an ionic polymer network capable of passivating defects and immobilizing ions by creating chemical bonding, electrostatic and steric physical barriers. Defects act as degradation catalysts. Hence, other ways to reduce defects, reported by Li $et\ al.$, include the control of film crystallization through a coordination bond formation between such additives and the Pb^{2+} of the MCP.[24] The organic cation ($e.g.$, FA^+) migration is also suppressed by forming hydrogen (H) bonding with the additive.

Uncontrolled crystallization causes incomplete conversion of PbI_2 to perovskite during annealing. Moreover, by balancing the chemical interaction rate with the wettability of substrates, the crystallization kinetics can be effectively controlled. Therefore, the formation of multiple chemical bonds such as H bond, coordination bond and ionic bond between additive components and the organic cations, Pb^{2+} and Sn^{2+} components of perovskite strengthens interfacial contacts and passivates the defects.[59] The additive's moderate hydrophobicity also inhibits heterogeneous nucleation and favors perovskite crystallization. As shown by Cacovich $et\ al.$,[60] an absence of PL peak shifts indicates the suppression of defect-induced phase segregation and surface recombination. Furthermore, defects formed due to the uncontrollable crystallization based on B-site cation mixing can also be suppressed as demonstrated by Shen $et\ al.$ through multi-functional additive engineering by controlling the perovskite crystal growth via H and coordination bonding with Pb^{2+} and Sn^{2+}.[38] It inhibits Sn^{2+} oxidation and alleviates interface stress.

Evidently, the development of MCPs is multifaceted and various strategies have been proposed to achieve the highest quality in this class of materials. Therefore, in this review article, we discuss the various strategies recently reported to advance the stability MCPs starting with the identification of new materials as well as the exploration of optimal functionalities in existing ones based on computational and experimental techniques. We also discuss measures of stability improvements in existing configurations through composition

engineering, materials engineering, defect passivation, phase stabilization, photophysical property enhancement and device engineering. We conclude with a summary and an outlook on future research directions to further advance the PV applications of MCPs.

2 Material identification

The search for an optimum composition in MCPs requires a combination of systematic experimental and computational studies.[3,46,49,61] To achieve environmentally stable and device-efficient perovskite semiconductors, compliant source materials must be prioritized. The source materials must have the capacity to yield perovskites exhibiting decent stability against stressors.

MCPs are ionic compounds composed of multiple cations ($i.e.$, organic and/or metal ions) and anions (halides) in the applicable A-, B- and X-sites. The synergistic effects of the multiple components confer better stability on MCPs relative to the single-cation single-halide perovskite configurations. Moreover, the multi-component characteristics require a careful control to minimize conflicting composition dynamics capable of jeopardizing their thermodynamic stability. For example, differences in ion mobility E_a can trigger ion migration which is a major degradation pathway in halide perovskites.[62] Hence, we focus on both the cationic and anionic components in identifying suitable MCPs as this is also crucial to the other characteristics such as the morphology, photophysics and device performance of MCPs. In particular, careful control of alloying and structural properties can yield photostable perovskites with optimized photophysics as shown in Fig. 1(a) which is the photon energy (E_{ph}) changes as a function of excitation time for $Cs_yFA_{(1-y)}Pb(Br_{0.4}I_{0.6})_3$ films. At $y = 0.20$, E_{ph} shows only a marginal change over the 30 min of excitation while a large decline can be seen at $y = 0.05$ and 0.60 indicating higher structural stability and less severe halide segregation at $y = 0.20$ unlike at the lower and higher Cs ratios. Similarly, a decline in structural stability as well as increase in alloy energetic disorder and electron–phonon coupling are responsible for the steady increase in the FWHM of the PL spectra up to $x = 0.8$ followed by a slight decrease for $Cs_{0.17}FA_{0.83}Pb(Br_x-I_{(1-x)})_3$, from the 100% iodide ($x = 0$) to 100% bromide ($x = 1$) range as shown in Fig. 1(b). Therefore, it is evident that rational processing of both the cationic and anionic components of MCPs is crucial to the identification of suitable material configurations.

To identify such perovskite materials, a physics-constrained sequential learning framework exhibiting superior search efficiency has been explored.[34] It can identify stable MCPs by fusing data from high-throughput experimental degradation tests and first-principles calculations of phase thermodynamics into an end-to-end Bayesian optimization algorithm using probabilistic constraints. 1.8% of the compositional space of $Cs_xMA_y-FA_{1-x-y}PbI_3$ perovskite was sampled and the $Cs_{0.17}MA_{0.03}-FA_{0.80}PbI_3$ configuration exhibiting an FA-rich and Cs-poor region, Region I in Fig. 1(d), shows the highest chemical and structural stability. It is also ca. 17 and 3 times more stable than
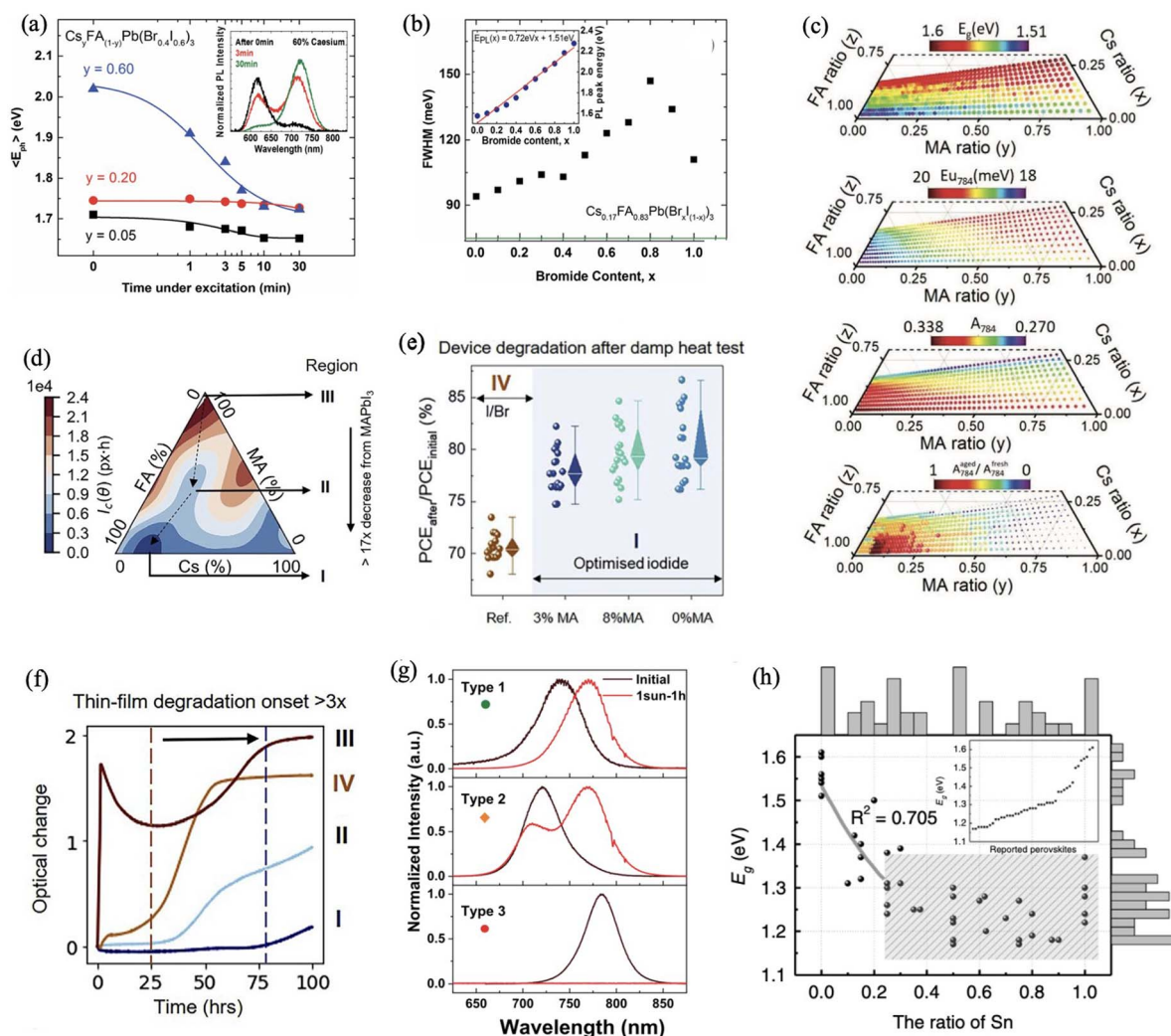
32966 | J. Mater. Chem. A, 2025, 13, 32964–33011

This journal is © The Royal Society of Chemistry 2025

Fig. 1 (a) Changes in average PL emission photon energy (E_{ph}) of $Cs_yFA_{(1-y)}Pb(Br_{0.4}I_{0.6})_3$ films at $y = 0.05$, $y = 0.20$ and $y = 0.60$. (b) FWHM of the PL emission spectra of $Cs_{0.17}FA_{0.83}Pb(Br_xI_{(1-x)})_3$ films as a function of Br^- content x. Inset shows the correlation between PL peak energy and Br^- content with fitting function. Reproduced from ref. 62 with permission from The Royal Society of Chemistry, copyright 2017. (c) Ranges of bandgap (E_g), Urbach energy (E_{u784}), absorbance (A) and aged to fresh absorbance ratio ($A_{aged784}/A_{fresh784}$) of $Cs_xMA_yFA_zPbI_3$ alloys at 520 locations. Reproduced from ref. 63 with permission from Wiley-VCH GmbH, copyright 2023. (d) Non-linear instability landscape ($I_c(\theta)$) within the $Cs_xMA_yFA_{1-x-y}PbI_3$ compositional space with stability in the order of Region I > Region II > Region III. (e) Comparison of percentage ratios of PCEs after damp heat degradation tests between Region IV I/Br-based PSCs and Region I I-based PSCs. (f) Optical changes as a function of degradation time showing Region I as the most stable region. Reproduced from ref. 34 with permission from Elsevier Inc., copyright 2021. (g) Normalized PL peaks of the photodegradation of materials showing three different degradation pathways denoted as Type 1, Type 2 and Type 3. Reproduced from ref. 21 with permission from Elsevier Inc., copyright 2023. (h) Fitted plot of bandgap (E_g) as a function of Sn : Pb ratio for 43 reported perovskites and histograms indicating corresponding distributions with respect to Sn : Pb ratio and bandgap. Inset is the bandgap values of the perovskites in ascending order. Reproduced from ref. 77 with permission from Springer Nature Ltd, copyright 2022.

$MAPbI_3$ and the widely reported $Cs_{0.05}(MA_{0.17}FA_{0.83})_{0.95}Pb(I_{0.83}Br_{0.17})_3$ respectively. Fig. 1(d) shows a non-linear instability landscape ($I_c(\theta)$) within the $Cs_xMA_yFA_{1-x-y}PbI_3$ compositional space. The instability index (I_c) shows a descending trend from Region III to I with the downward arrow indicating the magnitude of the stability of $Cs_{0.17}MA_{0.03}FA_{0.80}PbI_3$ against $MAPbI_3$. Hence, provided MA ratio is kept low and t is close to unity, some MA-containing triple-cation compositions can exhibit comparable I_c with their CsFA-based counterparts. The superior stability of Region I is further evident from the least change in optical properties

relative to prolonged exposure to stressors as shown in Fig. 1(f). The synergistic contribution of halide ratio to the stability is evident in Fig. 1(e) as the devices based on Region I composition outperform those based on other compositions during the degradation test as their "after PCE to initial PCE" ratios are closer to 100%.

The scope of compositional space can be expanded through a high-throughput optical characterization technique which identifies, studies and establishes a library of tunable alloys through composition grading. Graded layers of $CsPbI_3$, $MAPbI_3$ and $FAPbI_3$ were deposited by Moradi *et al.* on top of each other

This journal is © The Royal Society of Chemistry 2025

J. Mater. Chem. A, 2025, **13**, 32964–33011 | **32967**

at different gradient directions (*i.e.*, perpendicular for MAPbI$_3$ on CsPbI$_3$ followed by opposite for FAPbI$_3$ on MAPbI$_3$) to achieve a stack of CsPbI$_3$/MAPbI$_3$/FAPbI$_3$ through slot-die coating.[63] The resulting spatially varied compositions of Cs$_x$MA$_y$FA$_{1-x-y}$-PbI$_3$ single film were screened using a high-throughput robotized optical spectrometer. The organic cations, MA$^+$ and FA$^+$, support the perovskite structure stability, while the inorganic cation, Cs$^+$, supports the crystallization of pin-hole free films. By studying the stability of the alloys against moisture, targeted stable perovskite configurations can be obtained. In particular, Fig. 1(c) shows the changes in bandgap (E_g), Urbach energy (E_{u784}), absorbance (A) and aged to fresh absorbance ratio ($A_{aged784}/A_{fresh784}$) of Cs$_x$MA$_y$FA$_z$PbI$_3$ alloys at 520 locations. It can be seen that the properties vary between 1.51 and 1.6 eV, 18 and 20 meV, 0.270 and 0.338, and 0 and 1 respectively from the FA-rich region to the MA- and Cs-rich regions. The increase in bandgap and decrease in absorbance can be attributed to lattice shrinkage due to the transition from the larger FA$^+$ to the smaller MA$^+$ and Cs$^+$.[64,65] The relatively small Urbach energy at 784 nm indicates low energy disorder suitable for high performance in cells.[66,67] The more the deviation of $A_{aged784}/A_{fresh784}$ from unity, the higher the instability of alloys in the region. Hence, Cs$_x$MA$_y$FA$_z$PbI$_3$ is stable provided $x < 0.1$; $0.1 < y < 0.25$; $0.75 < z < 0.9$ with near-unity t.

A similar strategy is the high throuput measurements of multi-cation mixed-halide perovskites formulated and palletized on a chip by Wang *et al.* to quantitatively determine their structure–property relationships.[21] Mapping a series of FA$_{1-y}$Cs$_y$Pb(I$_{1-x}$Br$_x$)$_3$ perovskite to composition ratios, structure, bandgap, crystallographic phase and photostability facilitates the identification of perovskite alloys exhibiting a pure cubic phase, optimal defect chemistry, superior stability and adequate bandgap *ca.* 1.7 eV, suitable for perovskites on Si tandem solar cells. The normalized PL peaks in Fig. 1(g) show that the photodegradation of the materials follows three different pathways which are seen as a red-shifted single emission peak (Type 1), red-shifted double emission peaks (Type 2) and a complete loss of emission peak (Type 3). Moreover, most compositions undergo Type 1 photodegradation, indicating a low instability score. In particular, FA$_{0.775}$Cs$_{0.225}$-Pb(I$_{0.749}$Br$_{0.251}$)$_3$ was found to exhibit the most superior photostability which can be attributed to the low concentration of halide vacancy.[68–70]

The datasets obtained from these methods can be processed by density functional theory (DFT) and used to train surrogate models to achieve better property prediction and perform inverse design using genetic algorithm.[71] The datasets can be based on properties such as decomposition energies, bandgaps and PV efficiencies of a large number of MCPs compared with similar properties obtained from first-principles functionals. Also, the DFT and experimental datasets for each property can be used to train multi-fidelity random forest regression models using descriptors that one-hot encode, such as composition, phase and fidelity, which also include known elemental or molecular properties of the components occupying the A-, B- and X-sites of the perovskite lattice. The resulting optimized models, which can be combined with genetic algorithm using

an objective function, can predict thousands of experimentally promising compounds exhibiting low decomposition energy, suitable bandgap and efficiency.

Furthermore, due to the oversimplifications associated with single-parameter empirical descriptors such as t, models capable of providing a comprehensive view of the structures over a wide compositional space are a better choice. Stability predictions through machine-learning based on models predicting specific quantities such as the enthalpy of mixing and octahedral distortions coupled with an extensive dataset of first-principles calculations validated by experimental results have proven to facilitate the determination of the optimal mixing ratio of the cations and anions irrespective of the type and concentration. Park *et al.* built a model to predict the properties of perovskites made of B-site cations such as Ge^{2+}, Sn^{2+}, Pb^{2+}, X-site halides, *i.e.*, I$^-$, Br$^-$, Cl$^-$, and a range of A-site cations such as MA$^+$ and dimethylammonium DMA$^+$.[72] Using DFT, calculations of enthalpy-of-mixing for eight concentrations of each pair of ions selected were made. The dataset obtained gave trends capable of training a cubic-phase stability predictor and mapping the entire concentration range. The analyses of the experimental MA$_x$DMA$_{1-x}$PbI$_3$ showed that the effective ionic radius of DMA$^+$ is significantly larger than that of MA$^+$. Hence its weighted-average radius and deviation from cubic structure are expected to show a monotonic increase with increasing concentration due to t.[73,74] However, a non-monotonic behavior can be achieved at small DMA$^+$ (<2 mol%) concentrations.

Similarly, mixing Sn^{2+} and Pb^{2+} in the B-site yields bandgap tunable perovskites capable of realizing near infra-red optoelectronics. The attendant non-linear bandgap changes as a function of Sn : Pb ratio (*i.e.*, bandgap bowing) have been attributed to structural and chemical effects due to changes in compositional characteristics.[75–77] As shown in Fig. 1(h), the wide deviation of R^2 (0.705, gray line) from ideality and the disordered shaded area reveal the difficulty of determining the relationship between Sn : Pb ratio and bandgap through traditional methods. The limited knowledge from such methods can be advanced with machine learning which can give deeper insight into the phenomenon towards effective material control and optimization. This has been achieved by Cai *et al.* with the MASn$_x$Pb$_{1-x}$I$_3$ perovskite series through structural evolution and SHAP library analyses, revealing that the bandgap bowing involves an initial rapid drop in bandgap value at lower Sn concentration ($\leq$0.2 Sn : Pb ratio) followed by a plateaued low-bandgap region at higher Sn concentration.[77] It also shows that the bowing effect facilitates deviation of PV parameters such as J_{sc} and V_{oc} from the Shockley–Queisser theory which can be attributed to crystallographic distortion-induced deep-level traps and enhanced +2 to +4 oxidation susceptibility due to increasing Sn content. The machine learning predictions and experimental validation pinpoint an optimal Sn : Pb ratio of 0.6 for high-performance PSCs.

As shown in Table 1, Pb-halide perovskites exhibiting various compositions have been reported to-date, with remarkable progress in the aspects of device efficiency. Although substantial progress has also been reported for the material and device stability, a lot of improvement is still required in this aspect in

32968 | *J. Mater. Chem. A*, 2025, **13**, 32964–33011

This journal is © The Royal Society of Chemistry 2025

Table 1 PCEs and stability details of various MCPs as a result of the processing strategies

Compound	Strategy	PCE (%)	Stability comment	Ref
Cs$_{0.17}$MA$_{0.03}$FA$_{0.80}$PbI$_3$	Machine learning based on fused experimental and first-principles data	19.1	3 times more stable than Cs$_{0.05}$(MA$_{0.17}$FA$_{0.83}$)$_{0.95}$Pb(I$_{0.83}$Br$_{0.17}$)$_3$	34
FA$_{0.775}$Cs$_{0.225}$Pb(I$_{0.749}$Br$_{0.251}$)$_3$	High-throughput measurements of palletized samples	19.20	Best photostability within the FA$_{1-y}$Cs$_y$Pb(I$_{1-x}$Br$_x$)$_3$ series	21
FA$_{0.75}$MA$_{0.25}$PbI$_3$	Machine learning based on first principles and experimental data; inverse design using genetic algorithm	20	Highest frequency of occurrence in the chemical space	71
MA$_x$DMA$_{1-x}$PbI$_3$@x ≤ 2 mol%	Machine learning		Formation of a stable cubic MA–DMA mixed phase at ≤2 mol% DMA incorporation	72
(FAPbI$_3$)$_{1-x}$(MAPbBr$_3$)$_x$ at x = 0.8 mol%	Time-resolved spectroscopic study	25.38	Lowest structural disorder compared with other ratios	83
Cs$_{0.25}$FA$_{0.25}$MA$_{0.50}$Pb(Br$_x$Cl$_{1-x}$)	DFT study of Br$_x$Cl$_{1-x}$, Cl$_x$I$_{1-x}$ and Br$_x$I$_{1-x}$ halide combinations		Lowest positive excess energy and highest intramolecular coulombic attraction	84
(AzrH)PbBr$_x$I$_{3-x}$	Single crystal and powder X-ray diffraction analyses		Lattice constant follows Vegards's law as it is directly dependent on the Br content	3
Cs$_y$FA$_{(1-y)}$Pb(Br$_x$I$_{(1-x)}$)$_3$	Finetuning Cs$^+$ ratio to pinpoint a stable region		Stable at 0.10 < y < 0.30. Exhibits high crystallinity, long charge-carrier lifetimes and high mobilities	62
MAPbI$_3$:Cl	Composition-dependent effect of electron beam on the photocurrent properties		Photocurrent properties independent of electron beam unlike in MAPbI$_3$	57
Cs$_{0.05}$(FA$_{0.83}$MA$_{0.17}$)$_{0.95}$Pb(I$_{0.83}$Br$_{0.17}$)$_3$	Electrochemical impedance spectroscopy of the multi-site ion substitution effect		Significant increase in iodide diffusion activation energy	22
CsPbI$_2$Cl	Investigation of the correlated motion of A-site cation relative to the PbX sublattice (X = Cl, Br, I)		Lower thermal atomic fluctuation with the introduction of Cl due to its higher electronegativity and smaller size	28
CsPb$_{0.875}$Zn$_{0.125}$Cl$_3$	First principles calculation of Zn doping into the all-inorganic CsPb$_{0.875}$Zn$_{0.125}$X$_3$ (X = Cl, Br, and I) perovskite	20.58	Highest mechanical strength	90
MAPbI$_{2.91}$Br$_{0.09}$	Spray deposition using a ternary channel pumping system and vacuum-assisted annealing	17.07	Highest crystal quality of the MAPbI$_{3-x}$Br$_x$ series	92
FA$_{0.85}$Cs$_{0.15}$PbI$_3$	Investigation of the role of cation composition in the thermal stability of perovskite thin films	16.8	Most stable compositions against thermal stress, stable PCE at 85 °C for 1000 h	97
MA$_{0.2}$FA$_{0.8}$PbI$_3$	Crystallization of FA/MA perovskite using a viscous precursor solution of MA	11.10	Rapidly crystallized stable 3D α-phase FA/MA perovskite	99
Cs$_{0.17}$(FA$_{0.91}$MA$_{0.09}$)$_{0.83}$Pb(I,Br)$_3$	Increasing the damp-heat resistance of solar cells	20.82	Retention of ca. 80% of initial PCE after 500 h at 85 °C and 85% RH	103
Cs$_{0.2}$FA$_{0.8}$Pb((I$_{0.82}$Br$_{0.18}$)$_{0.97}$Cl$_{0.03}$)$_3$	Introduction of low percentages of Cl$^-$	22.6	Elimination of photoinduced halide segregation, improved crystallization	105
CsFa-perovskite	Replacing CsBr with cesium formate as the Cs precursor	20.01	Better crystallization and phase stability under illumination, reduced trap-state density	106
FA(Pb$_{0.5}$Sn$_{0.5}$)I$_3$	Achieving 3D MCP from the 2D MCP template through cation exchange	9.77	Successful in situ cation exchange yields stoichiometric composition and preferred orientation in the 3D MCP	111
Cs$_{0.11}$[(HC(NH$_2$)$_2$)$_{0.83}$(CH$_3$NH$_3$)$_{0.17}$]$_{0.9}$Pb(I$_{0.83}$Br$_{0.17}$)$_3$	Additive engineering and ink-jet printing under ambient conditions	11.4	Crystallization of pure perovskite phase under ambient conditions	133
K$_x$Rb$_{0.05}$Cs$_{0.10}$FA$_{0.85-x}$PbI$_3$	Using NH$_4$Cl to achieve uniform distribution of alkali metal cations (K$^+$/Rb$^+$/Cs$^+$)	22.53	Large monolithic grains, suppressed PbI$_2$ formation	116

This journal is © The Royal Society of Chemistry 2025

J. Mater. Chem. A, 2025, 13, 32964–33011 | 32969

Table 1 (Contd.)

Compound	Strategy	PCE (%)	Stability comment	Ref
$FA_{0.7}MA_{0.3}Pb_{0.5}Sn_{0.5}I_3$	Addition of ammonium citrate to mixed Sn–Pb perovskite precursors for crystal growth	20.95	Enhanced crystallinity, reduced interface stress, inhibited Sn^{2+} oxidation and mitigated interfacial defects	38
Sn–Pb perovskite	Introduction of 1-ethyl-3-methylimidazolium iodide into the mixed Sn–Pb perovskite precursor	22.87	Mitigation of Sn^{2+} to Sn^{4+} oxidation. Regulated film formation	122
$FA_{1−n}Cs_nPb(I_{1−x}Br_x)_3$	4 source combinatorial vacuum deposition using a non-rotating sample holder	~15	Deposition of more than 100 films with different compositions in a single run	123
$MAPb[I_{1−x}Br_x]_3$	Simplified dual-source vacuum deposition	19.4	Thermally stable after 3500 h at 85 °C	124
MACl treated FA-based perovskite	MACl vapor treatment-induced recrystallization, crystal growth direction finetuning and growth rate control	21.29	Pinhole-free highly crystalline films with large and uniformly distributed grains	102
$Cs_{0.05}(MA_{0.17}FA_{0.83})_{0.95}Pb(I_{0.83}Br_{0.17})_3$	Morphology analysis of perovskite grains using software "GrainD"		Polycrystalline perovskite films possess a lognormal grain size distribution	125
$FA_{0.85}MA_{0.15}Pb(I_{0.85}Br_{0.15})_3$	Experimental and theoretical evaluation of the aging process in the precursor solution		Formation of N-methylformamidinium adduct and non-photoactive hexagonal polytypes (6H and 4H)	126
$Cs_{0.05}FA_{0.85}MA_{0.1}Pb(I_{0.97}Br_{0.03})_3$	Introduction of Lewis base additives in the precursor solution	23.06	Prevention of aging through weak interactions between Lewis base additives and reactive A-site cations	24
$Cs_{0.05}FA_{0.85}MA_{0.1}Pb(I_{0.97}Br_{0.03})_3$	Introduction of diethyl (hydroxymethyl) phosphonate in a perovskite precursor solution	22.91	Improved stability of precursor solution. Retention of ca. 81% of initial efficiency after 50 days	134
$Cs_{0.40}FA_{0.60}Pb(Br_{0.17}I_{0.83})_3$	Using in situ GIWAXS to gain insights into the formation of MCPs based on coordinative solvents	17.6	Inhibition of the 2H/4H hexagonal phase formation	135
$Cs_{0.05}MA_{0.05}FA_{0.9}PbI_3$	Incorporation of N,N-dimethylmethyleneiminium chloride into the perovskite precursor solution	23.2	Suppression of phase segregation. Retention of 87.0% of initial PCE after ~1900 h at 85 °C and 85% RH	136
$Cs_{0.05}FA_{0.8}MA_{0.15}Pb(I_{0.745}Br_{0.255})_3$	Use of methylenediammonium dichloride additive in the perovskite precursor solution	35.7	Improved phase stability under prolonged light and heat exposure	137
$(FAPbI_3)_{1−x}(MAPbBr_{3−y}Cl_y)_x$	Using cellulose derivatives for perovskite crystallization engineering	24.71	Prolonged carrier lifetimes. Retention of >91.3% of initial PCE after 3000 h under ambient conditions	138
$Cs_{0.1}MA_{0.3}FA_{0.6}Pb_{0.5}Sn_{0.5}I_3$	Using molecule anchoring, interlayer and post-treatment strategies to grow perovskite film	27.1	Vertically aligned crystals, homogeneous crystallization, optimized interfaces	37
$FA_{0.75}MA_{0.25}SnI_3$	Healing multi-vacancy defects by an ionic compensation strategy	10.41	Improved crystal quality and surface morphology	171
$Cs_{0.05}FA_{0.79}MA_{0.16}Pb(I_{0.67}Br_{0.33})_3$	Construction of 2D/3D perovskite heterostructures to passivate defects and regulate interface properties	19.8	Superior moisture stability. Reduced ion migration	173
2D/3D multi-cation perovskite	Introduction of phenylammonium hydroiodide salts with different alkyl chain lengths into the PSC precursor solution	22.68	Retention of >90% of initial PCE	164
$(MAPbBr_3)_{0.05}(FAPbI_3)_{0.95}$	Resolving 2D/3D interface formation during spin-coating using in situ GIWAXS	21.9	Improved interface stability	176
$(C_4H_9NH_3)_x(3BrC_3H_6NH_3)_{2−x}CuCl_{2+x}Br_{2−x}$	Use of multiple cations to control the structural properties of Cu^{2+}-based 2D perovskites		Enhanced moisture stability. Improved Cu^{2+} reduction resistance. Higher crystallization	2

32970 | J. Mater. Chem. A, 2025, 13, 32964–33011

This journal is © The Royal Society of Chemistry 2025

Table 1 (Contd.)

Compound	Strategy	PCE (%)	Stability comment	Ref
$Cs_{0.05}FA_{0.95}PbI_3$	Incorporation of phenformin hydrochloride into the precursor solution with post-deposition treatment	24.67	Improved crystallization. Retention of 90% of initial PCE after 864 h at 85 °C	142
$Rb_{0.02}(FA_{0.95}Cs_{0.05})_{0.98}PbI_{2.91}Br_{0.03}Cl_{0.06}$	Using (5-mercapto-1,3,4-thiadiazol-2-ylthio) acetic acid to modify MA-free perovskite films	21.92	Retention of 99% of initial PCE after 1776 h under RH of 10–20%	98
$Cs_{0.05}(FA_{0.85}MA_{0.15})_{0.95}Pb(I_{0.85}Br_{0.15})_3$	Addition of 1-propionate-4-amino-1,2,4-triazolium tetra-fluoroborate additive to triple-cation perovskites	21.35	Retention of 85% of initial PCE after exposure to air for 4000 h under RH of 40 ± 5%	153
$FA_{1-x}MA_xPbI_3$	Using a pyridine-containing polymeric agent to manage multiple defects in perovskite surfaces	22.02	Retention of 90% of initial PCE after 2200 h under ambient conditions	139
$Cs_{0.04}(FA_{0.83}MA_{0.17})_{0.95}Pb(I_{0.83}Br_{0.17})_3$	Mixed-cation mixed-halide post-treatment	17.62	Secondary grain growth through Ostwald ripening	144
$Cs_{0.025}FA_{0.825}MA_{0.15}Pb(I_{0.85}Br_{0.15})_3$	Using (4-fluorobenzamide and 4-chlorobenzamide) to achieve multi-functional passivation in perovskite films	21.35	Retention of >90% of initial PCE after 2160 h under 50 ± 5% RH	154
$FACsPbI_3$	Synergistic cation and anion control of PbI_6 octahedra using vinylaniline trifluoromethanesulfonate	24.35	Retention of 91.38% of initial PCE at 25 °C and 20–30% RH	145
$CsPbI_{3-x}Br_x$	Using phenylethylammonium to achieve improved quality in an all-inorganic perovskite film	14.75	Retention of 83% of initial PCE after 400 h under 15 ± 5% RH	163
$Cs_{0.175}FA_{0.750}MA_{0.075}Pb(I_{0.880}Br_{0.120})_3$	Multifunctional passivation through antisolvent additive engineering	20.72	Retention of 51% of initial PCE after 129 days at 25 ± 5 °C under 45 ± 5–55 ± 5% RH	148
$FA_{0.9}Cs_{0.1}PbI_3$	Addition of ethylene diamine tetramethylene phosphonic sodium into the precursor solution of perovskite	19.156	Retention of ca. 90% of initial PCE after 1000 h at 25 °C and 40 ± 5% RH	158
$(FAPbI_3)_{0.85}(MAPbBr_3)_{0.15}$	Using natural alkaloid passivation agents, i.e., adenine and cytosine for defect management	22.07	Retention of 90% of initial PCE after 80 days under 50 ± 5% RH	172
$Cs_{0.05}(FA_{0.98}MA_{0.02})_{0.95}Pb(I_{0.98}Br_{0.02})_3$	Functionalizing multication halide perovskite interfaces with ferrocenyl-bis-thiophene-2-carboxylate	25.0	Retention of 98% of initial PCE after 1500 h at room temperature in N_2 with continuous 1-sun illumination	162
$Cs_{0.25}FA_{0.75}Pb(I_{0.85}Br_{0.15})_3$	DLTS and DFT correlation of perovskite/polymer multi-mode interactions with specific deep-trap states	24.32	No degradation at 85 °C for >1000 h in N_2	143
$FA_{0.95}Cs_{0.05}PbI_3$	Suppression of defect formation during ambient printing using 2-thiazole formamidine hydrochloride additive	23.72	Retention of 95% of initial PCE after 2088 h storage under ambient conditions	152
FAMACsRb perovskite	Achieving phase purity and black cubic FA-based perovskites by blending with smaller inorganic cations	20.24	Increased percentage of cubic phase and enlarged homogeneous crystallites	187
$FA_{0.85}Cs_{0.1}Rb_{0.05}PbI_3$	Investigation of thermal- and moisture-induced degradation of perovskites using in situ photoelectron spectroscopy		Increased thermal stability and ion migration barrier	188
$Cs_{0.15}FA_{0.85}PbI_3$	Revealing the origins of perovskite solar cell degradation through combined experimental and theoretical methods		High stability under white light illumination	54

This journal is © The Royal Society of Chemistry 2025

J. Mater. Chem. A, 2025, **13**, 32964–33011 | **32971**

Table 1 (*Contd.*)

Compound	Strategy	PCE (%)	Stability comment	Ref
$Cs_{0.05}(MA_{0.15}FA_{0.85})_{0.95}Pb(I_{0.84}Br_{0.16})_3$	Investigation of the chemical and structural evolution of perovskite thin-film after aging under controlled humidity		Photophysical changes due to the formation of PbI_2, $CsPb(I_{0.9}Br_{0.1})_3$ and $CsPb_2(I_{0.74}Br_{0.26})_5$	51
$Cs_{0.02}MA_{0.17}FA_{0.81}PbI_{2.49}Br_{0.51}$	Mechanochemically synthesizing mixed cation perovskite powders to prevent phase transition	24.56	Structurally stable without significant degradation after 70 days under ambient conditions	190
$Rb_{0.06}Cs_{0.08}FA_{0.78}MA_{0.08}Pb(I_{0.92}Br_{0.08})_3$	Engineering multi-cation halide perovskite composition via two-step sequential deposition	22.30	Retention of *ca.* 92% of initial PCE after 400 h under N_2 at room temperature	191
$(FA_{0.73}MA_{0.27})Pb(I_{0.945}Br_{0.055})_3$	*In situ* spectroscopic study of the role of free radicals in the degradation of perovskite		Rise in spin concentration increases degradation rate. No free radicals until the final stages of degradation	194
$Cs_{0.05}FA_{0.79}MA_{0.16}Pb(I_{0.83}Br_{0.17})_3$	Interfacial modification using organophosphorus ligands and antisolvent processing	18.29	Retention of *ca.* 85% of initial PCE after 2000 h under 50% RH, at 25 °C in air	179
$Cs_{0.4}MA_{0.2}DMA_{0.4}PbI_3$	Vacuum deposition of inorganic perovskite thin film by incorporating dimethylammonium iodide	14.80	Improved stability at 85 °C under 1 sun illumination	195
$Rb_{0.05}Cs_{0.10}FA_{0.85}PbI_3$	Thermally induced degradation of perovskite films *via* spectroscopic ellipsometry between 80 °C and 120 °C		Highly stable at 120 °C but degrades faster at lower temperatures due to phase instability	197
$MA_{0.1}Cs_{0.05}FA_{0.85}PbI_3$	Experimental and machine learning study of temperature-dependent stability and reversibility	19.30	Retention of *ca.* 100% of initial PCE after 1800 h under illumination at 30 °C	49
$Cs_{0.06}FA_{0.79}MA_{0.15}Pb(I_{0.85}Br_{0.15})_3$	Interface energy level alignment and defect passivation using dipole molecules (chlorine-terminated silanes)	20.30	Suppressed ion migration attributed to improved stability against light and moisture	180
$Cs_{0.1}(FA_{0.83}MA_{0.17})_{0.9}Pb(I_{0.83}Br_{0.17})_3$	Investigating the solar spectrum-dependent light-induced degradation in triple-cation PSCs	18	Retention of 100% of initial PCE in the dark under N_2 after 250 h. Significant degradation under light exposure	198
$Cs_{0.1}MA_{0.15}FA_{0.75}PbI_3$	Investigation of γ ray dosage tolerance of multi-cation perovskites		Phase segregation to MA^+- and FA^+-rich domains	199
$Cs_{0.12}FA_{0.88}Pb_{0.99}Cu_{0.01}I_{2.99}$	Enhancing light and radiation hardness by partially substituting Pb^{2+} with Cu^+ in perovskite solar cells	19.6	Cu^+ enhances photostability and tolerance to γ-rays and high energy electrons	200
$Cs_{0.04}Rb_{0.04}(FA_{0.65}MA_{0.35})_{0.92}Pb(I_{0.85}Br_{0.14}Cl_{0.01})_3$	Investigation of the radiation resistance in PSCs under extreme short-pulse proton irradiation conditions	18.01	Improved immunity to extreme high-intense short-pulse proton irradiation	201
$Cs_{0.1}MA_{0.15}FA_{0.75}PbI_3$	Investigation of nanoscale cation dynamics in perovskite films during electric-field-induced aging		FA^+ is preserved after 40 days while MA^+ is completely decomposed after 24 days	204
$MA_{0.5}Cs_{0.5}PbBr_{1.5}I_{1.5}$	Introducing multiple cations into the A-site and alloying halides in the X-site		Suppressed halide mobilities	205
$CsPbI_2Br$ and $Cs_{1.2}PbI_2Br_{1.2}$	Investigation of photodegradation *via in situ* atomic force microscopy		Nucleation of selectively expelled iodoplumbate as a separate I-rich phase at grain boundaries	53
$Cs_{0.05}(FA_{0.85}MA_{0.15})_{0.95}Pb(I_{0.95}Br_{0.05})_3$	Elimination of ion migration-induced degradation by incorporating multifunctional poly(ionic-liquid) additives	22.22	Retention of 80% of initial PCE after 1500 h under AM 1.5 G light soaking	58
$Cs(PbSnSrMnZn)Br_3$	Incorporation of multiple cations to synthesise high-quality all-inorganic entropy stabilized perovskite nanocrystals		Retention of emission characteristics and monodispersity after 8 months of aging in air	207
$FA_{0.85}MA_{0.1}Cs_{0.05}PbI_{2.55}Br_{0.45}$	Controlled incorporation of MA^+, Cs^+ and Br^- into $FAPbI_3$ lattice		Growth of inch-sized stable perovskite single crystals. Lower ion migration	208

Table 1 (*Contd.*)

Compound	Strategy	PCE (%)	Stability comment	Ref
CsFAMAPbIBr	Numerical study of the post-growth passivation treatments of perovskite using formamidinium bromide	24.62	Reduced recombination losses	210
$Cs_{0.10}MA_{0.15}FA_{0.75}PbI_3$	Comparatively studying azaadamantane-based molecular modifiers as stabilizing additives for perovskites		Prevention of photolysis product formation. Stable after 5000 h of continuous light exposure	211
$Cs_{0.03}FA_{0.945}MA_{0.025}Pb(I_{0.975}Br_{0.025})_3$	Introduction of N-acetyl-L-phenylalanine into PbI_2 precursor solution	25.05	Retention of 94% of initial PCE after 40 days of storage in ambient under 20% RH	212
$Cs_xMA_yFA_{1-x-y}PbI_3$	Recovering Pb from the glass substrate of discarded PSCs using ultrasonic water leaching technique		Removal of 99.84% of Pb after the first two cycles of ultrasonic water leaching	215
$Cs_{0.05}MA_{0.14}FA_{0.81}Pb(I_{0.9}Br_{0.1})_3$	Building a stable device irrespective of the perovskite absorber layer used	21.3	Retention of $ca.$ 90% of initial PCE after 1500 h under $50 \pm 10\%$ RH	217
$FAPb_{0.963}Sn_{0.037}I_3$	Enhancing multiple exciton generation and photon-energy threshold in mixed Sb–Pb perovskite nanocrystals		Slow cooling of hot carriers and reduced hot-carrier traps after Sn doping	220
$Cs_{0.05}(MA_{0.14}FA_{0.86})_{0.95}Pb(I_{0.84}Br_{0.16})_3$	Studying the effect of Ar^+ sputtering thinning on chemical composition and optoelectronic properties of perovskite		No phase segregation	60
$Cs_{0.06}FA_{0.79}MA_{0.15}Pb(I_{0.85}Br_{0.15})_3$	Investigating low-frequency carrier kinetics in perovskite solar cells		Carrier hopping exhibits localized and non-Debye type relaxation	221
$Cs_{0.1}FA_{0.9}PbI_{2.7}Br_{0.3}$	Overcoming limited carrier diffusion in inverted PSCs through band engineering	20.3	Retention of 89% of initial PCE after 250 h at 85 °C in N_2	8
$CsPbI_2Br$	Intercalating a chromium-based metal–organic framework into an inorganic perovskite Pb–I framework	17.02	Retention of >80% of initial PCE after 1000 h at 85 °C in air and 30% RH	9
$Cs_{0.05}MA_{0.08}FA_{0.87}Pb(I_{0.92}Br_{0.08})_3$	Evaluation of various literature strategies under standardized operational stability tests at 70 °C		HTL adversely impacts solar cell operational stability at elevated temperatures	48
$Cs_{0.05}(MA_{0.17}FA_{0.83})_{0.95}Pb(I_{0.83}Br_{0.17})_3$	Numerical investigation of perovskite solar cells to harmonize the trade-off between high PCE and stability	34.75	Optimized absorber layer properties, $e.g.$, thickness, doping ratio and bandgap energy improves device quality	256
$MA_{1-x}FA_xPbI_{3-y}Cl_y$	Introducing RbCl and choline chloride for structural intercalation of PbI_2 in a two-step sequential deposition	21.68	Retention of 91.5% of initial PCE after 840 h in N_2	233
$CsPbIBr_2$	Improving device performance through cation/anion co-doping	10.78	Retention of 98% of initial PCE after 7 days at an RH of 20–30%	249
$CsPbIBr_2$	Revealing the implication of rubidium and acetate (cation/anion) co-doping into inorganic perovskites	16.79	Enhanced performance parameters	250
$CsPbI_{1.5}Br_{1.5}$	Controlling the effects of FA^+ and MA^+ to improve the quality of $PbBr_2$-rich perovskite films	14.11	Retention of 85% of initial PCE after 1000 h in N_2	251
$Rb_xCs_{1-x}PbI_{1.75}Br_{1.25}$	Suppression of phase segregation through lattice distortion in perovskites	24.33	Increased ion-migration energy barrier. Retention of 80% of initial PCE after 420 h under ambient conditions	206
$CsPbI_2Br$	Simultaneously incorporating choline zwitterions into ETL and perovskite layer for high-efficiency PSCs	17.06	Retention of 92% of initial PCE after 500 h in N_2	235

This journal is © The Royal Society of Chemistry 2025

J. Mater. Chem. A, 2025, **13**, 32964–33011 | **32973**

Table 1 (Contd.)

Compound	Strategy	PCE (%)	Stability comment	Ref
$Cs_x\{FA_{0.4}MA_{0.6}\}_{1-x}PbI_{2.8}Br_{0.2}$	Evaluating the design and optimization of 4-terminal solar cell configurations using a capacitance simulator	29.34	HTM-free carbon-based devices, optimized perovskite thickness and doping ratio enhance the performance	248
CsFA perovskite	Using the hybrid evaporation-solution method to achieve stable, efficient and scalable PSCs	21.06	MABr-free PSCs show higher stability retaining 80% of initial PCE after 1600 h at 85 °C at 45–55% RH	234
$Cs_{0.05}(FA_{0.85}MA_{0.15})_{0.95}Pb(I_{0.85}Br_{0.15})_3$	Fabrication of highly efficient PSCs with a multi-cation hybrid ETL (SnO_2@Na:Cs) using continuous spin-coating	22.06	Improved perovskite crystallinity	237
$(FAPbI_3)_{0.927}(MAPbBr_3)_{0.073}$	Modifying SnO_2 ETL with ammonium citrate	21.58	Retention of 88% of initial PCE after 1000 h in the dark and at an RH of 10–25%	159
$(FA_{0.98}MA_{0.02})_{0.95}Cs_{0.05}Pb(I_{0.95}Br_{0.02})_3$	Modifying the SnO_2/perovskite interface with phosphorylcholine chloride	24.34	Retention of 91.44% of initial PCE after 1200 h at 25 °C and 25% RH	231
$Cs_{0.1}MA_{0.9}Pb(I_{0.9}Br_{0.1})_3$	Doping lanthanum into SnO_2 to improve the quality and performance of the perovskite layer under ambient conditions		Improved resistance against moisture	160
$FAPbI_3$ with 0.8 mol% $MAPbBr_3$	Modulating perovskite crystallization and interface defect passivation using guanidinium iodide	23.02	Retention of 71% of initial PCE after >900 h in a dark environment at 25 °C and RH of 30–40%	238
$Rb_{0.03}Cs_{0.05}FA_{0.90}MA_{0.05}PbI_3$	Introducing a series of fluorine-substituted succinic acid derivatives into the NiO_x/perovskite interface	25.92	Retention of 73% of initial PCE after 600 h at 85 °C	186
$Cs_{0.10}FA_{0.90}PbI_3$	Using dyes as self-assembled monolayers between transparent conductive oxide and perovskite layers	24.40	Retention of 91% of initial PCE after 1000 h at 85 °C in the dark	241
CsMAFA-based perovskite	Introducing poly(p-vinylbenzyl trimethylammonium hexafluorophosphate) into the NiO_x/perovskite interface	24.72	Retention of 88.5% of initial PCE after 1078 h at 85 °C in N_2	141
$(FA_{0.95}Cs_{0.05}PbI_3)_{0.975}(MAPbBr_3)_{0.025}$	Studying isomerism effects on passivation and charge transport using carbazolyl bisphosphonate additives	25.88	Retention of 95% of initial PCE after 1000 h at room temperature in N_2	185
$CsPbI_2Br$	Simultaneous perovskite/TiO_2 and perovskite/electrode interface passivation using perfluoropropionic acid	14.15	Retention of 84.59% of initial PCE after 30 days in N_2	236
$Cs_xMA_yFA_zPbI_3$	Fabrication of PSCs using compositionally tunable and solution processed perovskite alloys	22.20	J_{sc} loss is minimized with increased FA^+ and Cs^+ while an optimized MA^+ ratio is required to minimize V_{oc} loss	63
$FA_xCs_{1-x}PbI_3$	Strain regulation in thicker films with significantly long carrier lifetime	23.50	Efficiency enhancement in the corresponding solar cell through a strain regulation strategy	245
$Rb_{0.05}Cs_{0.05}MA_{0.05}FA_{0.85}Pb(I_{0.95}Br_{0.05})_3$	Predicting 6 months outdoor ageing tests of solar cells with indoor accelerated stability test	25.58	Self-assembled monolayer HTL enhances operational stability at high temperatures and under outdoor conditions	
$Cs_{0.01}FA_{0.94}MA_{0.05}PbI_{2.85}Br_{0.15}$	Fabrication of corresponding solar cell in ambient air through mixed antisolvent treatment	22.06	Reduced hysteresis and retention of more than 90% of initial PCE after 1300 h without encapsulation	255
2D $Cs_2PbI_2Cl_2$ capping agent	Interface stabilization for accelerated ageing of the corresponding solar cell	17.40	No degradation at 35 °C. Degraded only by 20% at 110 °C after 2100 hours under constant illumination	259

order to achieve commercialization and market viability. It is imperative to move beyond the state-of-the-art towards the discovery of new and more effective perovskite systems capable of further advancing the field. Hence, the important role of hybrid computational and experimental studies in the prediction, identification and development of new MCPs cannot be over emphasized.

3 Composition engineering

MCPs exhibit better device performance and when prepared at optimal composition ratio they can achieve better stability than the simple perovskite compounds. In fact, the best PCEs reported to-date are from PSCs based on MCP absorber layers.[24,78–80] The improved quality and fascinating properties stem from the synergistic effects of the constituent elements which confer better opto-electronic properties and can suppress ion migration-induced degradation.[22,81] Moreover, despite these merits, this class of materials is still plagued with several structural, morphological and photophysical challenges which limit its PV performance. Although the multi-component nature of the materials is an advantage, it can also be the origin of their challenges as it triggers competing and uncontrollable compositional dynamics.

In particular, the competing degradation dynamics of the constituent cations in $Cs_xMA_yFA_{1-x-y}PbI_3$ perovskites can be revealed by crystallographic studies based on synchrotron X-ray scattering.[34] It shows that the chemical decomposition and lattice disorder can be significantly minimized by using fewer elements and a maximum MA^+ ratio of 8%. This is important due to the poor chemical stability of MA^+ (through ion migration) and poor structural stability of Cs^+ (through phase separation). This is also applicable to mixed X-site halides such as in $(FAPbI_3)_{1-x}(MAPbBr_3)_x$. The thin film can be prepared by counteracting the inherent lattice disorder of the $FAPbI_3$ precursor material with the addition of $MAPbBr_3$ at different mole ratios of x, i.e., 0, 0.5, 0.8, 1, 2.5, 10, and 20 mol%. It reveals a composition ratio dependent control of the lattice disorder. As shown in Fig. 2(a), the lattice disorder is greatly suppressed at an optimal $MAPbBr_3$ ratio ($x = 0.8$ mol%) while higher ratios lead to the formation of grain boundaries. Time-resolved transient absorption spectroscopy also shows that lattice disorder can dictate carrier dynamics and optoelectronic properties of the material. Fig. 2(b) shows a blue shift of the negative photobleaching at different delay time bands near 800 nm, indicating increase in bandgap.

Since the valence band maximum (VBM) of perovskites consists of metal cation s-orbitals and halide anion p-orbitals and the conduction band minimum (CBM) consists mainly of metal cation p-orbitals,[82] substituting I with a higher electronegative Br reduces the potential energy of the VBM leading to bandgap enlargement. Also, the wrinkles observed in the photo-induced absorption band (insets) with increasing $MAPbBr_3$ ratio indicate additional transition peaks. Hence beyond the introduction of the grain boundary, the disorder in crystal structure also creates additional transition states which cause hot carrier trapping and recombination. A decrease in the

disorder leads to decreases in trap density and charge-carrier losses, prolonged carrier lifetime, higher mobility and longer diffusion length.[83]

Tailoring the composition of MCPs offers flexibility of tuning the material properties and device performance. In particular, varying the halide ratio in a mixed halide configuration can have a profound effect on the structural and opto-electronic properties of the perovskite. For the triple-cation mixed-halide perovskite $Cs_{0.25}MA_{0.25}FA_{0.50}Pb(X_xX'_{1-x})_3$ where X = I, Br, Cl, with $0 \leq x \leq 1$, of all the configurations, $Cs_{0.25}MA_{0.25}FA_{0.50}Pb(Br_xCl_{1-x})_3$ exhibits the least excess energy hence the highest stability due to the smallest difference in ionic radius between Br^- and Cl^- as well as the highest coulombic attraction between Pb^{2+} and Cl^-.[84] Substituting the A-site triple-cations with a single slightly bulky cation such as aziridinium cation $AzrH^+$ to obtain $(AzrH)PbBr_xI_{3-x}$ perovskite, electronic spectroscopy shows that the bandgap of the material can be easily varied between 1.57 eV and 2.23 eV by halogen substitution.[3] Single crystal and powder X-ray diffraction analyses also show that the lattice constant of the obtained $(AzrH)PbBr_xI_{3-x}$ perovskites is linearly dependent on its Br^- content although it preferentially incorporates I^- over Br^- during formation.

The variations in halogen composition can influence the responses of the MCP to stressors as can be seen with $MAPbI_3Cl$ which shows a blue shift of its PL peak on exposure to an electron beam similar to $MAPbI_3$. Low electron beam dosage under cryogenic conditions can purge defect sites and enhance the stability and optical properties of the perovskites thereby increasing their photocurrent.[57] However, unlike $MAPbI_3$, the photocurrent of $MAPbI_3$:Cl is independent of the electron beam due to the existing defect purging based on the passivation effect of Cl^-. The effect of the Cl^- also stems from its synergistic interactions with I^- in the X-site of the perovskite lattice which reduces ion migration. Since lead halide perovskites are ionic materials, their ion mobility determines their device stability. Hence, a reduced ion migration is key to the device life span as rapid ion migration leads to rapid degradation of the materials and devices. High efficiency solar cells based on perovskites such as $Cs_{0.05}(FA_{0.83}MA_{0.17})_{0.95}Pb(I_{0.83}Br_{0.17})_3$ are achieved by multiple cation and anion substitutions into the parent $FAPbI_3$ structure at the A and X sites.[22] The effect of such multiple substitutions on the mobility of ions within the perovskite lattice can be unraveled through electrochemical impedance spectroscopy which can reveal the E_a of such ion diffusion.[85,86]

The crystal lattice components significantly affect the E_a. For example, electrochemical impedance spectroscopy reveals that the addition of smaller cations, i.e., Cs^+ and MA^+ into the FAPI lattice greatly reduces the E_a for iodide diffusion whereas the addition of multiple cations and anions at multiple lattice sites (i.e., A- and X-sites) to obtain triple cation perovskites such as $Cs_{0.05}(FA_{0.83}MA_{0.17})_{0.95}Pb(I_{0.83}Br_{0.17})_3$ significantly elevates the E_a of iodide diffusion and suppresses ion migration, suggesting the synergistic merits of multiple ion (i.e., cations and anions) substitution on the perovskite lattice and stability. Evidently, composition engineering, especially cation engineering influences perovskite stability. It shows that rational mixing of cations and control of lattice parameters are important
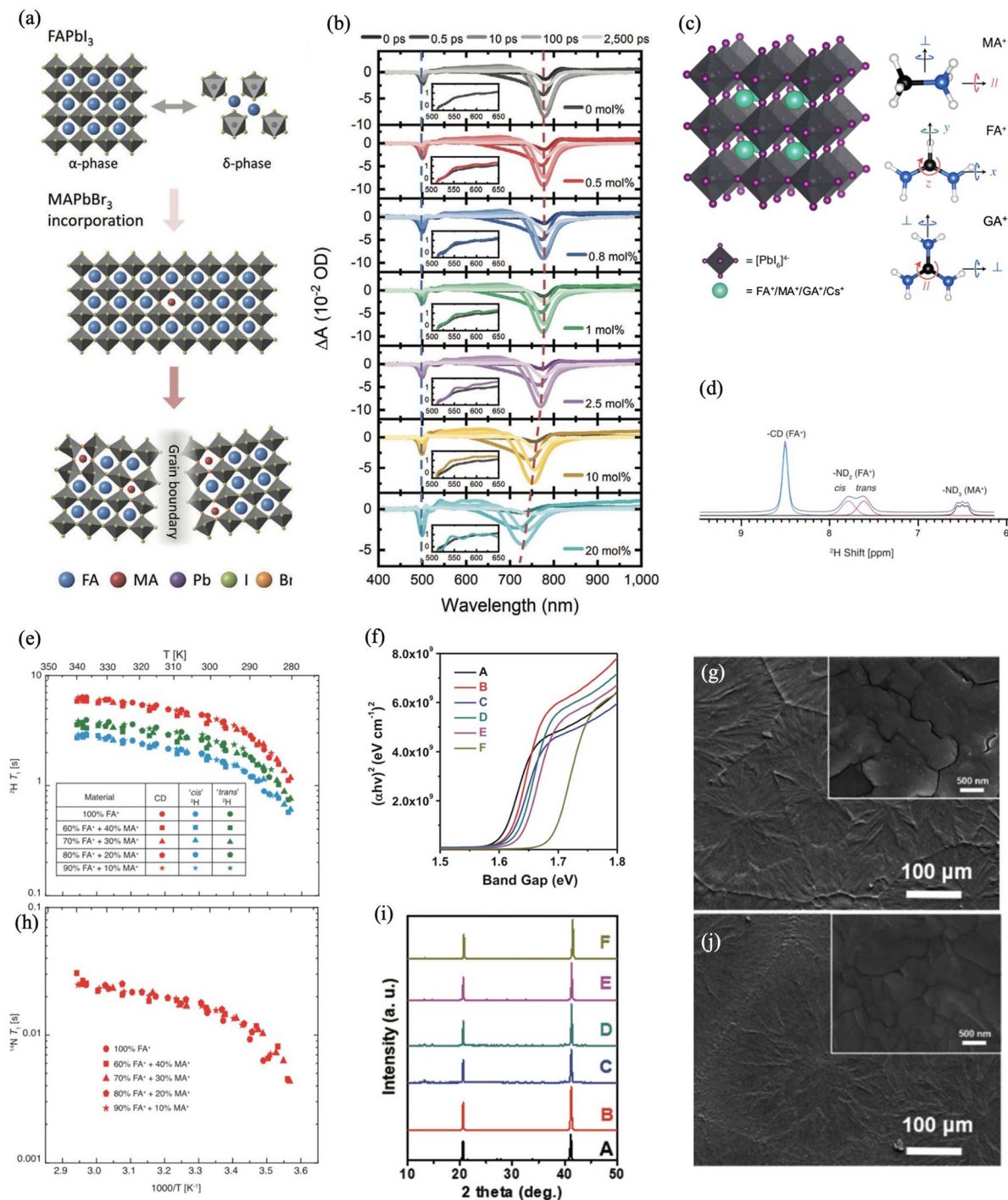
This journal is © The Royal Society of Chemistry 2025

J. Mater. Chem. A, 2025, **13**, 32964–33011 | **32975**

Fig. 2 (a) Schematic illustration of the effect of $MAPbBr_3$ on the crystalline structure of $(FAPbI_3)_{1-x}(MAPbBr_3)_x$ thin film with increasing ratio of $MAPbBr_3$. (b) Transient absorption spectra of $FAPbI_3$ and $(FAPbI_3)_{1-x}(MAPbBr_3)_x$ thin films at 0, 0.5, 10, 100, and 2500 ps time delay with two dashed lines depicting the peak positions of the photobleaching bands. Insets are the spectral responses near the photo-induced absorption band ranging from 500 to 650 nm at 10 ps time delay. Reproduced from ref. 83 with permission from Wiley-VCH GmbH, copyright 2024. (c) Perovskite crystal structure and the common A-site cations, i.e., MA^+, FA^+ and GA^+ with their principal axes of rotation. H, C and N atoms are denoted by white, black and blue balls, respectively. (d) Deconvoluted single pulse solid-state ^2H magnetic angle spinning NMR spectra of the cubic phase of $FA_{0.70}MA_{0.30}PbI_3$. (e) ^2H and (h) ^{14}N magnetic angle spinning NMR derived relaxation constants as a function of inverse temperature and ratio of MA^+ in $FA_xMA_{1-x}PbI_3$. Reproduced from ref. 27 with permission from American Chemical Society, copyright 2022. (f) Tauc plot showing bandgap tuning of $MAPbI_{3-x}Br_x$ films at A–F; $x = 0$, 0.09, 0.11, 0.14, 0.2, 0.5. (i) XRD patterns of $MAPbI_{3-x}Br_x$ films at A–F; $x = 0$, 0.09, 0.11, 0.14, 0.2, 0.5. (g) Plan-view SEM image of $MAPbI_{3-x}Br_x$ film at A; $x = 0$. (j) Plan-view SEM image of $MAPbI_{3-x}Br_x$ film at B; $x = 0.09$. Reproduced from ref. 92 with permission from Wiley-VCH GmbH, copyright 2020.

32976 | J. Mater. Chem. A, 2025, 13, 32964–33011

This journal is © The Royal Society of Chemistry 2025

prerequisites to a successful synthesis of perovskites by solution or physical processes and the realization of improved thermodynamic stability as well as electronic properties.

A-site cations in metal halide perovskites do not directly contribute to their optoelectronic properties. Moreover, they indirectly influence the optoelectronic properties through their interaction with the BX_3 sublattice.[26-29] This interaction depends on the electronegativity and size of the X-site anion. As can be seen in the parent perovskite $CsPbX_3$ with the interaction of Cs^+ and the PbX_3 sublattice ($X = Cl^-$, Br^-, I^-), Cl^- which is the most electronegative suppresses thermal atomic fluctuations which favors optoelectronic performance.[28] Hence $CsPbI_3$ quality can be improved by Cl^- doping to achieve $CsPbI_3$:Cl. As shown by nonadiabatic molecular dynamics simulations, the suppression of atomic fluctuations leads to a reduction in electron-vibrational interactions which can prolong charge carrier lifetime by ca. 1 order of magnitude. The organic cations also indirectly influence the perovskite optoelectronic properties through their rotation and dynamics in the cuboctahedra cavities of the perovskite structure as shown in Fig. 2(c). Using variable temperature ^2H and ^{14}N quadrupolar solid-state NMR relaxometry under magic angle spinning, the E_a and correlation time (τ_c) for rotation about the principal axis of a series of organic cations at room temperature can be evaluated.[27]

Considering MA^+, FA^+ and the bulky GA^+ in the FA^+/Cs^+, FA^+/MA^+, $FA^+/MA^+/Cs^+$ and MA^+/GA^+ compositions of a multi-cation perovskite structure, it can be found that MA^+, FA^+, and GA^+ have at least one component of rotation at the picosecond timescale at room temperature, with MA^+ and GA^+ exhibiting the fastest and slowest components respectively while FA^+ has a constant component. Moreover, mixing GA^+ and MA^+ in the cavity accelerates the rotations of both cations at picosecond timescale. The cation dynamics depend on the symmetry of the cuboctahedra cavity, dictated by the inorganic lattice but are independent of the degree of cation substitution. In particular, when sufficiently above the phase transition temperature, the FA^+ rotation is constant across all compositions studied. However, the addition of Cs^+ into the FA^+ matrix at room temperature significantly changes the FA^+ motion due to changes in the phase transition temperature unlike in the deuterated $FA_xMA_{1-x}PbI_3$ synthesized with all four deuterium NMR signals resolved as shown in Fig. 2(d) to allow easy measurements of ^2H and ^{14}N relaxation constants. In this series, FA^+ dynamics are largely unaltered despite the variation in MA^+ ratio (Fig. 2(e and h)). Conversely, the cation dynamics can also include a ^2H relaxation of MA^+ in $FA_xMA_{1-x}PbI_3$, which can result from its physical diffusion to paramagnetic defects. This phenomenon can provide the basis for ion migration and the formation of paramagnetic defects. Moreover, the phenomenon can be eliminated by high-purity solution-processing of the samples.

The perovskite optoelectronic properties are mainly based on the B-site cations. In fact, it is well known that the unique and fascinating properties of halide perovskites are mainly attributed to the presence of B-site Pb^{2+}.[87-89] Such properties can be further advanced by rationally doping other cations into the lattice B-site. For example, zinc (Zn)-doped all-inorganic perovskite systems $CsPb_{0.875}Zn_{0.125}X_3$ ($X = Cl$, Br, and I) have demonstrated better structural and mechanical stability than the pristine form.[90] This stems from the lattice shrinkage caused by the Zn^{2+} which alleviates lattice stress, reduces halide vacancy defects, enhances charge transport and improves stability. The doping gives the material good ductility, high mechanical strength and high corrosion resistance making it applicable in flexible PVs. Although the $CsPb_{0.875}Zn_{0.125}X_3$ perovskite possesses a low extinction coefficient and refractive index (1.45–2.00) as well as high transmittance (88.7%), these characteristics make it suitable for application in semi-transparent devices. Moreover, other properties such as absorption coefficient and transmittance which can be up to 6.11×10^5 cm^{-1} and 73% respectively in ultraviolet light, peak value of the figure of merit (at 300 K) of 0.34 and average sound transmission loss >2 dB in its ultra-thin monolayer form all make the $CsPb_{0.875}Zn_{0.125}X_3$ perovskite suitable for the construction of building envelopes, temperature difference power generators and sound insulators.

The molar ratio and chemical composition of such perovskite compounds can be controlled, to achieve better material quality through a high throughput method which combines inkjet-printing to tune the material composition by the simultaneous printing of different precursor inks using multiple printheads controlled by varying the number of droplets printed by each printhead.[91] The process is optimized through an algorithm based on the python programming language that ensures optimal mixing of the precursor inks. The compositional homogeneity of the deposited films from atomic to microscopic scale can be evaluated as a function of the amount of materials deposited and the printing resolution by micrometer-resolution X-ray fluorescence and synchrotron-based grazing-incidence wide-angle X-ray scattering (GIWAXS). Too low printing resolutions indicate poor intermix of the precursor inks while too high resolution yields a thick wet film exhibiting significant demixing of the precursor inks. Optimal printing resolution yields homogeneous films and indicates an effective mixing on the atomic scale.

The method can also yield a library of homogeneous mixed compositions of the perovskite series such as $CsPb(Br_xI_{1-x})_3$, ranging between $CsPbI_3$ and $CsPbBr_2I$ which affords bandgap tunability and application in multi-junction solar cells. The mixed composition can be optimized by adjusting the flow rate of the syringe pump in an ultrasonic spray pyrolysis deposition rather than through the traditional stoichiometric manipulation from the precursor stock solution.[92] This has been used to achieve $MAPbI_{3-x}Br_x$ mixed-halide perovskites using a ternary channel pumping system to deposit each of the MAI, PbI_2, and $PbBr_2$ precursor solutions. The method can achieve bandgap tuning as shown in the Tauc plot in Fig. 2(f) where the bandgap ranges from 1.60 to 1.69 eV for A–F (i.e., $x = 0$, 0.09, 0.11, 0.14, 0.2, 0.5) with the film obtained at $x = 0.09$ (i.e., $MAPbI_{2.91}Br_{0.09}$) being the most highly oriented and crystalline film with large clusters as indicated in the XRD peak intensity in Fig. 2(i) and the SEM image comparison with the film obtained at $x = 0$ in Fig. 2(g and j). Hence, the x ratio tuning can achieve optimal absorption, energy level alignment and PL properties. Vacuum-

This journal is © The Royal Society of Chemistry 2025

J. Mater. Chem. A, 2025, 13, 32964–33011 | 32977

assisted thermal annealing can further optimize the efficiencies of corresponding devices. The post-deposition thermal treatment must be optimized as hybrid organic–inorganic perovskites can be vulnerable to thermal stress,[50,93–95] raising issues about their thermal stability.

Compositional engineering of the materials by using multiple-cation perovskites has shown great promise for mitigating this challenge.[94,96,97] However, the thermal stabilities of different perovskite compositions and device architecture as well as nonuniform measurement protocols limit the effective evaluation of this characteristic. For example, MA is known to serve as the weakest link in mixed-cation perovskite compositions as thin films of perovskites such as CsMAFA and MAFA exhibit comparable thermal stability.[97] It suggests that although FA^+ and Cs^+ confer better thermal stability, MA exhibits similar limiting effects on the perovskite compositions and solar cell devices irrespective of the other cations present and it is advised to avoid MA during thin film growth in order to achieve thermally stable solar cells.[98] Moreover, a systematic investigation of the role that cation composition (i.e., MA^+, FA^+, Cs^+) plays in the thermal stability of perovskite thin films can be done by comparing the thermal degradation of the perovskite thin films in terms of decomposition, optical losses and optoelectronic changes at an elevated temperature such as 85 °C for a duration of up to 500 h.[97] The effect of thermal stress on the perovskite layer and how it affects the solar cell performance can also be investigated. Under these conditions, the perovskite thin films undergo degradation, with MA-based perovskite thin films showing the maximum degradation due to PbI_2 loss while the stoichiometries of MA-free perovskite thin films such as $FAPbI_3$ and $FACsPbI_3$ are largely maintained as no decomposition can be observed within the test period. The origin of the decomposition of the MA-based perovskite, e.g., $MA_{0.5}FA_{0.5}PbI_3$, is the changes in surface composition in which FA^+ is retained while MA^+ is expelled.

Nevertheless, to stabilize the α-phase of mixed-cation perovskites with high FA^+ ratios by using an MA-based precursor, a viscous solution can be used to incorporate high amounts of MA into the film since the stability of the perovskite film depends on the MA content.[99] A low MA ratio causes crystallization into 1D $FA_3(MA)PbI_5$ due to incomplete solvation of the $[PbI_6]^{4-}$ clusters while a high MA ratio leads to full solvation of the clusters, rapid crystallization and complete stabilization of the active 3D $MA_{0.2}FA_{0.8}PbI_3$ perovskite film's ∝-phase. This is due to the formation of FA^+–MA complexes which facilitate the crystallization and compatibility of the method with the one-step deposition of mixed cation perovskites suitable for large scale processing. Thermal treatment can dictate the rate of solvent evaporation during the crystallization. Although slow evaporation of solvents such as DMF or DMSO can improve the crystallization, it extends the crystallization time and may be incompatible with large scale deposition, limiting its usefulness in upscaling perovskite solar cell fabrication and their commercialization viability. Incidentally, incorporating the MA-based precursors can yield high crystallization at a shorter time.

Therefore, before post-fabrication issues such as morphological, structural, opto-electronic, device performance and stability characteristics of the MCPs and corresponding devices are considered, a careful determination of the chemical compositions and their ratios as well as the preparation protocol most suitable for the realization of high-quality MCPs must be prioritized. To achieve this, a deep knowledge of the competitions between the compositions in terms of their sensitivity to their chemical environment (i.e., other constituents) and preparation related stressors (e.g., heat generated during annealing) is required.

4   Materials engineering

Enhancing the properties of as-prepared perovskite materials is crucial to their applications in optoelectronic devices. Strategies such as post-deposition annealing,[100–102] surface and bulk passivation,[98] recrystallization[102] etc. have been reported to boost or optimize the properties and device performance of halide perovskites. Many aspects of the materials can also be better understood through various engineering strategies as presented in Table 1. For example, the simultaneous stability of CsFAMA perovskite solar cells against heat and humidity can be achieved through the use of an antisolvent, alkyl-type interfacial passivation and effective encapsulation.[103] Optical and crystallographic measurements show that Cs^+ ratio in a perovskite compound such as $Cs_x(FA_{0.91}MA_{0.09})_{1-x}Pb(I,Br)_3$ can be varied in the range $0 \leq x \leq 0.362$ with the optimal ratio being $x = 0.17$ to obtain $Cs_{0.17}(FA_{0.91}MA_{0.09})_{0.83}Pb(I,Br)_3$ perovskite, assisted by the introduction of an octyl-ammonium iodide interlayer in an alkyl-type passivation. The antisolvent casting time range can also be 8 s $\leq t \leq$ 15 s with the optimal antisolvent casting time yielding champion device efficiency with the open circuit voltage (V_{oc}) being $t = 12$ s. The stability can be further enhanced through a low-temperature vacuum lamination which effectively seals the device.

Also, by eliminating Cs^+, MA^+ and Br^- from the perovskite composition through an antisolvent quenching process, a polymeric interlayer can be in situ deposited to promote the growth of less defective and phase-pure perovskite crystals.[104] Although the strategy shows some merits such as enhanced photoexcited charge extraction and reduced defect resulting from the slow evaporation of solvents during crystal growth, achieving additive-free, MA-free triple halide perovskites offers additional merits such as the prevention of photoinduced halide segregation, improved crystal quality and compatibility with a self-assembled monolayer to yield high device performance. Introduction of a low ratio of Cl^- into the lattice also offers bandgap tunability.[105] Replacing the halide salt precursors with their organic salt analogues can ensure better structural integrity. In particular, replacing a Cs halide (e.g., CsBr) precursor with Cs formate promotes the perovskite crystallization as shown in Fig. 3(a) Compared to the CsBr, Cs formate slows down the crystallization process by breaking it down into two steps which involve the formation of $HCOO–Pb^+$ and $HCOOH–Cs^+$ complexes followed by their de-coordination and crystallization with FA^+, MA^+ and halide to form the perovskite. During the process, $HCOO^-$ is replaced by I^- or Br^- while the free $HCOO^-$ coordinates with H^+ to form HCOOH which volatilizes during

32978 | J. Mater. Chem. A, 2025, **13**, 32964–33011

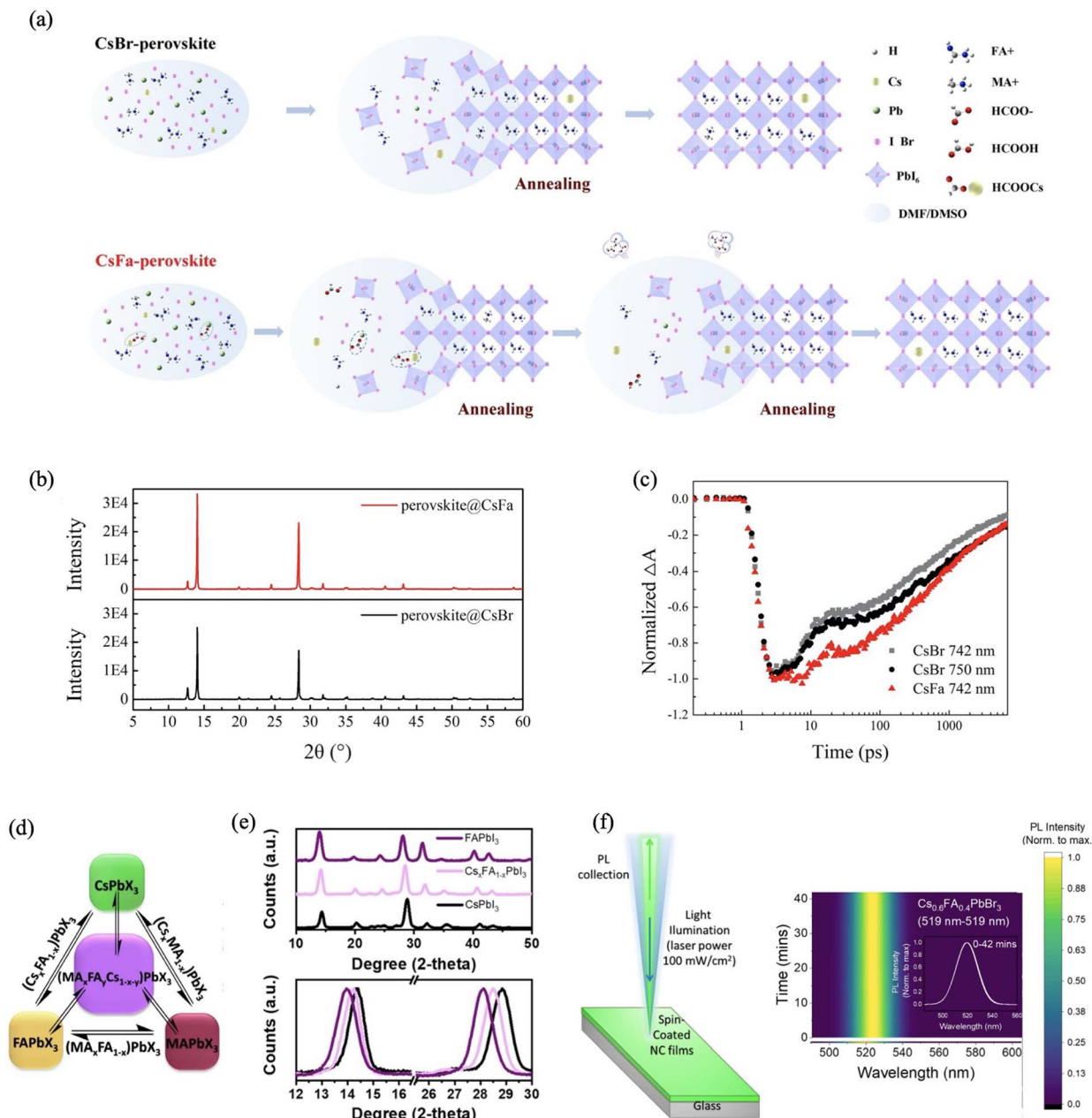This journal is © The Royal Society of Chemistry 2025

Fig. 3 (a) Schematic illustration of the crystallization processes of CsBr- and Cs formate-perovskites. (b) XRD patterns of CsBr- and Cs formate-perovskites. Cs formate denoted as CsFa. (c) Transient absorption decay kinetics of CsBr- and Cs formate-perovskites. Reproduced from ref. 106 with permission from The Royal Society, copyright 2022. (d) Schematic illustration of the multiple-cation perovskite series achievable through cation exchange between single-cation perovskite nanocrystals. (e) Comparison of the XRD patterns of $CsPbI_3$, $FAPbI_3$ and $Cs_xFA_{1-x}PbI_3$ nanocrystals to confirm the formation of $Cs_xFA_{1-x}PbI_3$ by cation exchange through peak shifts (bottom panel) resulting from changes in chemical environment. (f) Schematic illustration of the PL stability test of $Cs_{0.6}FA_{0.4}PbBr_3$ quantum dot thin layer deposited by spin-coating on a glass substrate and the corresponding 2D PL spectra over 42 min under direct illumination. The inset shows the changes in the PL spectra over the illumination period. Reproduced from ref. 23 with permission from Wiley-VCH GmbH, copyright 2022.

annealing. The process has a better control on perovskite nucleation and yields larger grain sizes compared to those of the CsBr based perovskite as indicated by the higher intensities of the XRD peaks shown in Fig. 3(b) where the Cs formate is denoted as CsFa. The charge carrier dynamics obtained from femtosecond transient absorption spectroscopic measurements in Fig. 3(c) show that such improved crystallinity results in longer time constants, indicating a lower probability of carrier trapping and recombination at the perovskite grain boundary.[106]

The realization of large grains and high crystallinity in MCPs can be advanced by an organic species such as 1,3-

bis(cyanomethyl)imidazolium bis(trifluoromethylsulfonyl) imide which is able to form an extensive network of low energy barrier H bonds as it possesses a Lewis-basic nitrile group and a hydrophobic anion. The nitrile group coordinates to the Pb^{2+}, slowing down crystallization, leading to larger crystal size formation and film passivation while the strong H bonding interactions and hydrophobicity provided by the anion contribute to the overall stability of the materials.[10] The interaction between such bulky organic species (*e.g.*, phenethyl-ammonium) and the inorganic octahedra in the perovskite structure can be harnessed by creating a series of lattice-reinforced 2D/3D perovskite structures.[107] This can address the residual stress which causes lattice distortion and undesired phase transition in the perovskite absorber. The extent of interaction depends on the steric hindrance effect based on the molecular configuration. The interaction also determines interfacial energy-level alignment as well as the 2D top layer formation.

The transition processes of α-phase to γ-phase and δ-phase can also be monitored to understand the relationship between the release of residual stress and lattice reinforcement through combined theoretical and experimental measurements. Lattice reinforcement enhances the perovskite crystals' resistance to temperature dependent lattice distortion, preventing transition to the γ-phase. It also prevents moisture induced erosion and δ-phase transition. Hence, identifying the relationship between the cation mixture and the possible structural deformation can help determine the optimum chemical compositions required for such synthesis. It can suppress the formation of local distortions and microscopic disorders which catalyze poor structural stability and phase segregation. Infusing benzyl-amine vapor into multi-cation 3D perovskites can achieve 2D structures of multi-cation perovskite materials exhibiting alternating cation interlayers on top of a 3D multi-cation perovskite.[108] The 2D/3D perovskite configuration can be confirmed by GIWAXS. The process is a fast vapor passivation strategy which reduces defects and tensile strain. It also aligns the energy levels, suppressing interfacial charge recombination. The 2D top surface is more n-type than the 2D/3D perovskite bulk, facilitating the electron transfer to the contact electron transporting layer (ETL). Theoretical analysis reveals that the alternating cation interlayer phase is thermodynamically more stable than an analogous Ruddlesden–Popper phase. The strategy is compatible with various fabrication methods involving vapor or solution techniques proving the benzylamine vapor as a universal passivator. The 2D top layer is hydrophobic and it passivates the 3D surface defects and inhibits non-radiative recombination. It acts as a blocking layer, hindering interfacial ion migration.

Moreover, as shown in Fig. 3(d), ion migration in the form of fast and spontaneous A-site cation cross-exchange can take place between $APbX_3$ perovskite nanocrystals (A = Cs^+, FA^+ and MA^+) at room temperature.[23] It is facilitated by free A-oleate complexes present in the colloidal perovskite nanocrystal solutions. The process is as fast as halide exchange and the action of the A-oleate complexes is similar to that of the alkylammonium halides in halide exchange[109,110] and can achieve double (*e.g.*, MACs, MAFA, CsFA) – and triple (MACsFA)-cation perovskite nanocrystals. For example, the XRD patterns and peak shifts in Fig. 3(e) confirm the successful formation of a CsFA double cation perovskite from the cation cross-exchange between $FAPbI_3$ and $CsPbI_3$. Notably, ion exchange commonly occurs between the liquid and solid phases.[111–113] Although solid–solid phase ion exchange has been observed between compositionally different perovskite nanostructures placed in contact to form thin film-on-thin film and quantum dot-on-thin film configurations, the ion exchange was observed between their X-site halides (*i.e.*, anion exchange).[113–115] Moreover, cation exchange is more prevalent between the liquid and solid phases, *i.e.*, a solution-quantum dot configuration.[111,113] The resulting compositionally modified nanocrystals can be deposited to form thin films for targeted characterization and device applications. An example is the normalized 2D PL measurement, shown in Fig. 3(f), of $Cs_{0.6}FA_{0.4}PbBr_3$ quantum dot thin layer on glass, showing stability (see inset) over 42 min of constant illumination, indicating the absence of phase segregation and its suitability for device application.[23]

The uniform distribution of the cations in the perovskite lattice can be confirmed by material characterization based on optical spectroscopy, XRD, atomically resolved high-angle annular dark-field scanning transmission electron microscopy (HAADF-STEM) and integrated differential phase contrast (iDPC) STEM. Unlike the halide, the A-cations do not exhibit light-induced phase-segregation as no splitting can be observed in their PL peaks. Notably, the removal of the free oleates by antisolvent purification can significantly slow down the cross-exchange process. In the same way, alkali metal cations (*i.e.*, K^+, Rb^+ or Cs^+) can be uniformly distributed in the A-site of the single-cation perovskite structure (*e.g.*, $FAPbI_3$) to boost PV performance.[116] This can be facilitated by the application of NH_4Cl additive which improves PbI_2 solubility through the formation of an intermediate which favors the transformation and pure perovskite phase formation during annealing. It also favors grain size increase, crystallinity improvement and suppression of PbI_2 formation. At a low molar ratio, K^+ is homogeneously distributed in the film, Cs^+ is more concentrated at the surface and Rb^+ is more concentrated at the bottom without NH_4Cl. With NH_4Cl, Cs^+ and Rb^+ can be more homogeneously distributed as NH_4Cl slows down the movement of Cs^+ and Rb^+ by changing the growth direction of the perovskite film from top-down to lateral, improving the distribution uniformity and the film crystallization quality.

Similarly, partial incorporation of Sn into the lattice B-site yields a mixed Sn–Pb perovskite which exhibits several degradation pathways.[117–119] Notably, the degradation can be mitigated by removing the thermally unstable MA^+ through the development of an MA-free perovskite such as $Cs_{0.2}FA_{0.8}Sn_{0.5}Pb_{0.5}I_3$ and by increasing the resistance of Sn to oxidation.[119] The quality of the MA-free perovskite films can be tuned by incorporating cations such as dipropylammonium as well as Rb^+ into the precursor solution to achieve $Rb_x(Cs_{0.2}FA_{0.8}Sn_{0.5}Pb_{0.5}I_3)_{100-x}$ ($x = 0, 1, 3, 5,$ and 10). Other steps are to add some reducing agents such as $NaBH_4$ and conduct surface engineering by the use of 4-fluorophenethylammonium chloride as

32980 | *J. Mater. Chem. A*, 2025, **13**, 32964–33011

This journal is © The Royal Society of Chemistry 2025

an interlayer material. This can lead to improved morphological, structural and optoelectronic properties (*e.g.*, enhanced exciton recombination lifetimes, carrier mobility) and suppressed recombination. The crystallization of mixed Sn–Pb perovskites is often rapid and uncontrollable, causing great amount of defects and stress.[118,120] Film deposition methods such as blade-coating also worsen this drawback.[38,121] Ammonium citrate exhibiting multiple hydroxyl, carboxyl and amino groups can control the crystal growth based on its interaction with Pb^{2+} and Sn^{2+} ions through H and coordination bonding.[38] It increases the film's crystal quality, inhibits Sn^{2+} oxidation, and alleviates interfacial stress and defects, yielding better energy level alignment. The oxidation of Sn^{2+} to Sn^{4+} and

uncontrolled crystallization kinetics can also be suppressed as illustrated in Fig. 4(a) by incorporating the 1-ethyl-3-methylimidazolium iodide (EMIMI) additive into the Sn–Pb perovskite lattice.[122] The additive shows stronger interaction with SnI_2 than PbI_2 and regulates the film growth, forming low-dimensional Sn-rich/pure-Sn perovskites ($EMIMSn_xPb_{1-x}I_3$) at the grain boundaries and interfaces which inhibit oxygen ingression, Sn vacancy and defect state formation.

Furthermore, higher throughput can be achieved in the vacuum deposition of MCPs through a combined vacuum deposition from 4 sources on a non-rotating sample holder. The method can achieve more than 100 solar cells with different perovskite absorbers in a single deposition run. The process can

Fig. 4 (a) Lattice diagram of perovskite films with and without EMIMI treatment. Reproduced from ref. 122 with permission from Elsevier B.V. and Science Press, copyright 2024. (b) Possible formation pathway of MFA$^+$, comparisons of MFA$^+$ with FA$^+$ in terms of interactions with solvent (DMF) and orientation around $[PbI_6]^{4-}$ octahedra, possible exchange of MFA$^+$ with FA$^+$, leading to the formation of δ-FAPbI$_3$. Reproduced from ref. 126 with permission from American Chemical Society, copyright 2024. (c) Coordination of tetrahydrotriazinium cation with PbI$_6$- or PbBr$_6$-octahedra of the perovskite layer by forming multiple H bonds with the I$^-$ and Br$^-$. Reproduced from ref. 136 with permission from American Association for the Advancement of Science, copyright 2024.

be fine-tuned to achieve the best-performing formulations. For example, $FA_{1-n}Cs_nPb(I_{1-x}Br_x)_3$, deposited by this method, was obtained by calculating the initial deposition rate for each precursor (*i.e.*, FAI, CsI, PbI_2, and $PbBr_2$) based on the target perovskite stoichiometry.[123] The difference in the absorber layers obtained was determined by spatially resolved high throughput characterization involving optical, morphological and structural techniques. Moreover, the drawbacks of vacuum processing of wide bandgap MCP thin films which requires a simultaneous control of several thermal sources during the deposition can be addressed through a simplified dual-source vacuum deposition method.[124] With optimized thickness, the method can yield solar cells based on mixed-halide perovskites exhibiting comparable device efficiencies as those of multiple A-cation perovskites and with better thermal stability. MA-based perovskite films can be prepared by this method through simultaneous sublimation of MAI and a pre-synthesized mixed halide Pb precursor. The bandgap of the $MAPb(I_{1-x}Br_x)_3$ perovskite film can be tuned by varying the I^-/Br^- ratios in the $Pb(I_{1-n}Br_n)_2$ precursor. The finding is in contrast to many reports discussing the limited use of MA^+ in solution processed halide perovskite thin films to ensure stability.[34,98,105,116]

Although vacuum deposition is a preferred fabrication method for PSCs, the deposited films are also plagued with imperfections, poor crystallinity and small grain sizes. Nonetheless, post-deposition treatments can mitigate this challenge. Annealing the film in the vapor of an additive can induce the recrystallization of the film. For example, vapor deposited FA-based perovskite films can be treated with MACl vapor.[102] The MACl vapor easily gets inserted into the perovskite lattice and is removed by evaporation at elevated temperatures. The insertion and evaporation steps subject the perovskite crystals to a restructuring process which favors grain size enlargement. To limit a large removal of MACl molecules at once, which can cause shrinkage and voids in the film, multiple short-time vapor treatment cycles can be done with the optimum condition being 3 cycles for 30 s each. Hence, it involves a repeated fine-tuning and control of the crystal growth rate and direction. The method can yield pinhole-free perovskite films with superior crystallinity, large (*ca.* 3 μm) and uniformly distributed grains as well as enhanced performance.

To further advance the stability and efficiency performance of perovskite films it is important to understanding their microstructural characteristics. Thin film grains can be analyzed using the GrainD software, an automatic perovskite grain analysis software developed using an image segmentation algorithm. The images can be originally obtained using SEM. The software reveals the average radius, distribution pattern, area of contact and population of the grains. For example, it shows that the grain size of polycrystalline perovskite films exhibits a lognormal distribution rather than the Gauss distribution.[125] Statistical probability theory and grain growth theory show that multiple random factors affecting film growth are responsible for the lognormal distribution. Such random factors are also seen in solution processing where spontaneous reactivity between the multiple components in the precursor solution of multi-cation mixed-halide perovskites creates

a challenge of accurately formulating a desired perovskite type as well as the determination of the actual precursor solution–film property relationship which limits the fabrication of reproducible and efficient solar cells.

Bravetti *et al.* revealed the presence of the *N*-methyl-formamidinium (MFA^+) adduct in an aged MA^+/FA^+ solution and the formation of hexagonal polytypes (6H and 4H) during $FA_{0.85}MA_{0.15}Pb(I_{0.85}Br_{0.15})_3$ perovskite crystallization.[126] The formation kinetics of the adduct depends on the solvent used which dictates the rate of the nucleophilic addition reaction between FA^+ and MA^+ as MA^+ initially undergoes deprotonation to form MA which is then added to FA^+. Hence, choice of solvent plays a role in the crystallographic, optical and compositional stability of the resultant perovskite films. The common solvents are mixed dimethylformamide (DMF)/dimethyl sulfoxide (DMSO), mixed gamma-butyrolactone (GBL)/DMSO, and DMSO.[126–130] The aging process can be monitored through nuclear magnetic resonance (NMR), optical, morphological and crystallinity characterization. In Fig. 4(b), DFT calculations show the formation of the MFA^+ adduct, its similarities to FA^+ in the orientation around $[PbI_6]^{4-}$ octahedra and interactions with the solvent (*i.e.*, DMF), the possibility of forming a range of FA^+/MFA^+ mixed cation ($MFA_xFA_{1-x}PbI_3$) perovskite configurations as well as its capacity to preferentially stabilize the undesirable δ-FAPbI₃. Strategies capable of retarding the deprotonation process and the overall reaction between the organic parts (*i.e.*, MA^+ and FA^+) can stabilize the precursor solution and make the properties of the resulting film more predictable. This may involve the addition of Cs^+ which can act as a Lewis acid, coordinating the formed MA and preventing it from adding on to FA^+. Other strategies are to add thiethylborate as well as sulfur which can effectively inhibit MA^+ deprotonation based on amine–sulfur coordination.[131,132]

Furthermore, *in situ* liquid time-of-flight secondary ion mass spectrometry of $Cs_{0.05}FA_{0.85}MA_{0.1}Pb(I_{0.97}Br_{0.03})_3$ precursor solution corroborates this finding, suggesting the interactions of Lewis base additives such as ethyl ethanesulfonate and triethyl phosphate with the cations and anions in solution.[24] Highly coordinating Lewis base additives such as the thio-semicarbazides can also be used to create a stable intermediate phase by adjusting the coordination environment of Pb^{2+} and tuning the nucleation process to achieve uniform, crystalline and pinhole-free perovskite thin films.[133] To achieve this, the tautomeric thiosemicarbazide structure is modulated with an acidic additive. Combined spectroscopic and computational analyses, evaluation of the mechanism of interactions within the solution as well as the effects of the Pb-complex structures on perovskite formation guide the thin film application as photoactive layers in PV devices. It reveals the complex colloidal chemistry of a perovskite precursor solution and its significant impact on the properties of deposited films.

The reproducibility of high-quality perovskite thin film which is related to the stability and shelf-life of the precursor solution can also be enhanced through the reactive inhibition of the perovskite precursor solution by the introduction of di-ethyl (hydroxymethyl) phosphonate which can significantly improve the stability of precursor solution and that of the

32982 | *J. Mater. Chem. A*, 2025, **13**, 32964–33011

This journal is © The Royal Society of Chemistry 2025

corresponding device.[134] The solution stability is achieved as the phosphonate inhibits the reactivity of the halide and organic cation through multiple chemical bonds. Furthermore, the chelation interaction of Pb^{2+} with the oxygen of the phosphonate improves the perovskite film quality by passivation and maintains the stoichiometry, reducing the defects and unreacted PbI_2. The diethyl (hydroxymethyl) phosphonate treatment can realize precursor solution, thin films and devices exhibiting stability under ambient conditions, excellent performance and reproducibility making the perovskite systems suitable for scalable fabrication and commercial feasibility. Crystalline phases and coordination complex intermediates formed during film preparation significantly influence the optoelectronic properties, morphology and performance of metal halide perovskite solar cells.

Therefore, it is important to understand the role the adopted preparation method and coordination solvent play during thin film growth. The gas quenching method useful for scalable deposition used in the spin coating deposition of Cs_xFA_{1-x}-$Pb(I_{0.83}Br_{0.17})_3$ perovskites and studied by *in situ* GIWAXS reveals that by comparing DMSO and 2-methyl-*n*-pyrrolidone (NMP) as coordinative solvents, the intermediates formed using DMSO depend on the perovskite composition (*e.g.*, Cs^+), while the formation of intermediates with the use of NMP is independent of the perovskite composition.[135] A small amount of Cs^+ (*e.g.*, 10% and 20%) in the perovskite composition can yield the best device efficiencies with the use of NMP. However, higher amounts (30% and 40%) are more favorable with DMSO. This stems from the disappearance of the 2H/4H hexagonal intermediate phases associated with the small amount of Cs^+ which causes irregular morphology and low device performance. However, the absence of the 2H/4H hexagonal phase at low Cs^+ ratio favors better performance when using NMP.

In situ formations can also be of benefit as can be seen with the film stability enhancement attributed to the *in situ* formation of dimethylammonium and methyl tetrahydrotriazinium cations in precursor solution by a reaction of added *N*,*N*-dimethylmethyleneiminium chloride with MA^+ and FA^+.[136] The methyl tetrahydrotriazinium cation increases the formation energy of iodine vacancies as well as the ion migration energy of I^- and Cs^+, improving film crystallinity and suppressing non-radiative recombination, thermal decomposition and phase segregation processes. Hence, crystal defects and film non-uniformity in a perovskite top cell can be minimized to achieve the full potential of monolithic perovskite/silicon tandem solar cells by such methods. The methylenediammonium dichloride additive also forms tetrahydrotriazinium *in situ* in perovskite precursor solutions.[137] The tetrahydrotriazinium cation can be incorporated into the perovskite lattice during film crystallization. As illustrated in Fig. 4(c), the tetrahydrotriazinium cation exhibits a uniform distribution of its three –NH groups which strongly coordinate with PbI_6^- or $PbBr_6^-$ octahedra by forming multiple H bonds with the I^- and Br^-, increasing the formation energies of halide vacancy defects. Fourier-transform infra-red spectroscopy shows that the tetrahydrotriazinium cation prevents the release of cations at high temperatures and illumination. This resulting structure

favors the phase stability of the perovskite film as well as the device efficiency under prolonged light and heat exposure.

Evidently, the additives' multiple interaction sites favor crystallization engineering as can be seen with cellulose derivatives developed from natural cellulose.[138] Their multiple interaction sites can mitigate inherent defects and prevent random distribution of excess PbI_2 in perovskite film. The multiple interaction sites including the cyano group, hydroxyl group, carbonyl group and chloride anion strongly bind with the perovskite *via* electrostatic interactions, H bonding and coordination bonding. In particular, the derivative with the cyano-imidazolium cation and chloride anion facilitate the perovskite crystallization process, grain growth and directional orientation while transferring excess PbI_2 to the surface of perovskite grains. The PbI_2 can also form plate-like crystallites in local domains. It leads to the suppression of ion migration and defect formation, decrease in grain boundaries, better energy level alignment, enhanced carrier extraction, inhibition of non-radiative recombination and prolonged carrier lifetimes. The directional orientation of the perovskite crystals to achieving vertical alignment as well as interface engineering can advance the charge generation, separation, transport and extraction in the film. Subjecting perovskites such as $Cs_{0.1}$-$MA_{0.3}FA_{0.6}Pb_{0.5}Sn_{0.5}I_3$ to molecular anchoring using an L-alanine methyl ester additive as well as the introduction of 2D PEA_2PbI_3SCN can realize vertical crystal growth and homogeneous crystallization through SCN^- anchoring with the perovskite cations, releasing vertical residual strains and enhancing hole extraction.[37] Post-deposition treatment with ethylenediamine dihalides ($EDA(I/Cl)_2$) also creates a gradient energy level alignment between the perovskite and the ETL.

Overall, modifying MCPs can tune their properties, leading to improved performance and stability. Materials engineering efforts have sought to advance their compositional and structural properties through solution and physical growth methods towards the realization of high-quality structures and excellent PV performance. Moreover, it is important to extend the efforts to wide area processing so as to facilitate the scalability of the technology. Therefore, new and efficient materials as well as processing techniques are essential for the large-scale production of MCPs.

5 Defect passivation

In spite of the significant strides made by halide perovskites in recent years, the challenges of device efficiency and long-term stability which can be attributed to the defect states still plague this class of materials.[98,139–141] Defects are imperfections in perovskite materials and devices which negatively impact their quality and performance. These defects (*e.g.*, grain boundaries and point defects) serve as carrier traps and recombination centers, suppressing charge separation and transport, leading to low PCE and rapid degradation.[139,142,143] The defects may emerge in perovskite systems during fabrication, operation and exposure to stressors.[143] This can also be due to their ionic and polycrystalline nature. Defect deactivation is a passivation strategy aimed at improving the material and device quality

This journal is © The Royal Society of Chemistry 2025

J. Mater. Chem. A, 2025, **13**, 32964–33011 | **32983**

through defect density suppression. It reduces non-radiative recombination and vulnerability to environmental factors, according the technology better industrial and commercial viability.[141,142] Defect deactivation is the most common passivation approach. It is based on the use of passivation agents such as additives as well as techniques such as anti-solvent treatment.[140,144] The deactivation is achieved through isolation and trap filling.

Antisolvents are commonly employed during spin-coating deposition to isolate pure phase perovskite films. Thin films of MCPs such as $Cs_{0.04}(FA_{0.83}MA_{0.17})_{0.95}Pb(I_{0.83}Br_{0.17})_3$ have been enhanced through grain boundary passivation by treating the as-deposited film with isopropanol antisolvent containing a mixture of FAI and MABr to achieve secondary grain growth as a result of controlled Ostwald ripening.[144] The use of non-toxic environmentally friendly isopropanol antisolvent is a merit over the standard and toxic chlorobenzene and toluene. Defect isolation can also involve the creation of a physical barrier to prevent external factors from inducing defects. This is achieved through surface coatings and encapsulations.[145–147] Moreover, trap filling can be facilitated with additives such as 2-hydroxyethyl acrylate, benzyl acrylate, 2-phenoxyethyl acrylate and 3-phenoxy-2-hydroxypropyl acrylate possessing functional groups such as; carbonyl (C–O), hydroxyl (–OH), alkoxy (–O–CH$_2$) and aromatic groups.[148] They bind to the defects and prevent charge trapping. In particular, C–O fills the halide vacancy by binding with under-coordinated Pb^{2+}. –OH promotes the nucleation by interacting with the positively and negatively charged defects *via* H and coordination bonding, –O–CH$_2$ forms H bonds with organic species such as MA^+ and FA^+, the lone pair of electrons on the oxygen atom act as a Lewis base passivator. The high electron cloud density on the aromatic group suppresses acceptor type trap state. A synergistic effect of the functional groups subdues the multi-type defects resulting from the ionic properties of the perovskite. It produces larger grain size and higher crystallinity. Also, the additives' hydrophobic long alkyl chain and benzene ring prevent the degradation for perovskite films. Fullerene derivatives have shown similar passivation effects. In particular, Shukla *et al.* showed that the fullerene derivative with a carboxylic group (–COOH) significantly improves the efficiency and stability of Sn-based PSCs due to its superior capacity to suppress defects and the oxidation of Sn^{2+} to Sn^{4+} in the perovskite layer.[149]

Notably, defect passivation has achieved high-quality perovskite films *via* ambient printing despite oxygen and moisture sensitivity.[150–152] Multiple H bonds and coordination interactions between the applied 2-thiazole formamidine hydrochloride additive and precursor components promotes perovskite crystallization and reduces cation and anion vacancies.[152] H bonds are usually formed between the additives' functional group (*e.g.*, formamidine and carbonyl groups) and the halides of the perovskites (*e.g.*, FAI, PbI$_2$) while the coordination bonds are formed between the electron-rich groups of the additives (*e.g.*, O, S and N atoms of furan and thiazole rings) and the electron-deficient component of perovskite (usually Pb^{2+}) in a Lewis acid/Lewis base interaction. For example, defect states in wide area devices have been passivated using zinc

trifluoromethanesulfonate.[150] The oxygen atoms in the –SO$_3$ group (electron-rich) strongly interact with uncoordinated Pb^{2+} defects (electron-poor) on the perovskite surface. These interactions slow down nucleation and crystal growth, producing less defective large and compact crystalline grains. Since perovskites are ionic compounds which exhibit multi-type defects,[48–56] some passivators act as bifunctional groups possessing both electron-donating and electron-withdrawing characteristics and can passivate multi-type defects. An example is the post-crystallization treatment based on *S*-methylisothiosemicarbazide hydroiodide which passivates both bulk and interfacial multiple defects.[142] Its sulfur (–S–) group heals undercoordinated Pb^{2+} defects through the donation of a lone pair of electrons while its –NH$_3^+$ cations and I$^-$ anions compensate for iodine and organic cation vacancy defects respectively.

Similarly, a multi-active-site Lewis base ligand such as (5-mercapto-1,3,4-thiadiazol-2-ylthio)acetic acid can modify the surface and grain boundaries of MA-free perovskite films.[98] In these regions, it forms strong chemical interactions between its multiple active sites and the less-coordinated Pb^{2+}. Based on DFT results, the multi-active-site adsorption is thermodynamically more favorable than single-active-site adsorption irrespective of the PbI$_2$ termination and organic halide termination types. Hence, as illustrated in Fig. 5(a and b), crystallization of the perovskite materials can be controlled and its non-radiative charge recombination centers reduced through such synergistic effects. This is evident in the Pb–N coordination bond formation between the –NH$_2$ group of 1-propionate-4-amino-1,2,4-triazolium tetra-fluoroborate (PATMBF$_4$) additive and Pb^{2+} of (CsFAMA) perovskite as well as the formation of H bond between the oxygen atom of the additive's carbonyl group (CO) and the –N–H group of FA^+. This effect enhances charge transfer and suppresses FA^+ ion migration.[153] The combined passivation effect of a multi-functional passivation molecule such as 4-fluorobenzamide and 4-chlorobenzamide, which contain functional groups *i.e.*, amine, carbonyl group, benzene ring and highly electronegative halogens (*i.e.*, Cl, F) further supports the passivation of positive and negative defects by the formation of H bond with organic cations (*e.g.*, FA^+) and ionic bond with Pb^{2+}.[154] The halogens induce halogenated passivation, yielding reduced trap densities and increased carrier lifetimes.

Moreover, multi-functional halogen-free cesium trifluoroacetate can also achieve such properties in MCPs.[155] The schematic illustration in Fig. 5(c) shows the presence of iodine vacancy in the $[PbI_6]^{4-}$ octahedra of the perovskite lattice due to uncoordinated Pb^{2+}. It shows that the –COO$^-$ of the additive can passivate the defects and stabilize the perovskite structures by coordinating with the Pb^{2+}. The coordination bonding is facilitated by lattice adjustments caused by the partial substitution of FA^+ and MA^+ with the smaller ionic size Cs^+ of the additive at the A-site. The trifluoride methyl (–CF$_3$) part also blocks water ingression, enhancing the perovskite's stability against moisture ambient atmosphere. Other additives such as zwitterionic 1-(3-sulfopropyl)pyridinium hydroxide[156] and succinic acid derivatives[157] follow a similar defect passivation pathway. The multiple anchor points of such additives, *e.g.*, ethylene diamine

32984 | *J. Mater. Chem. A*, 2025, **13**, 32964–33011

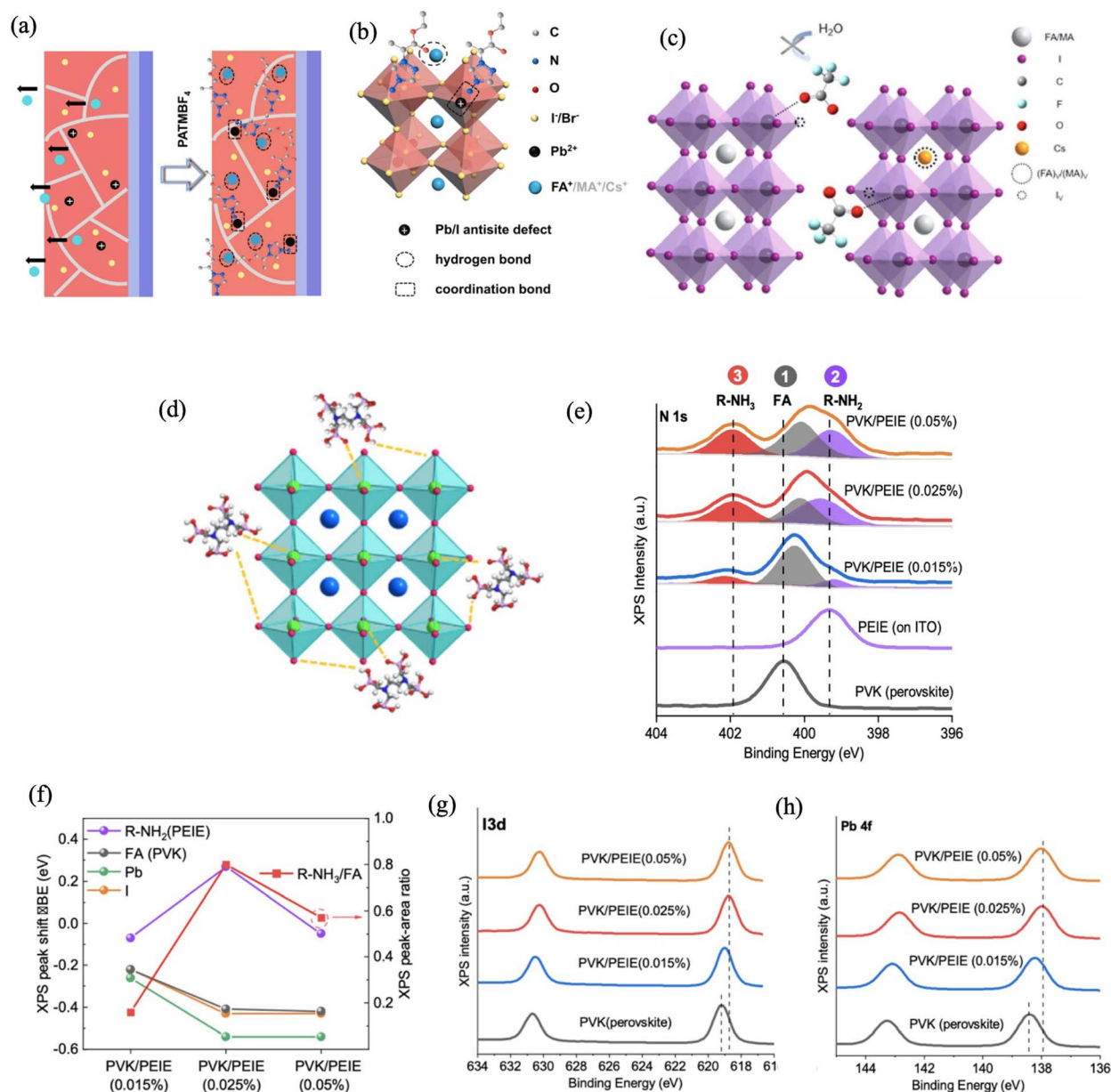This journal is © The Royal Society of Chemistry 2025

Fig. 5 (a) Schematic representation of the migration of organic cations out of the pristine perovskite film and the prevention of ion migration by immobilizing the organic cations and passivating the Pb^{2+} defects with $PATMBF_4$ additive. (b) Schematic illustration of the Pb–N coordination bonding interactions between the $-NH_2$ group of the $PATMBF_4$ additive and the Pb^{2+} of the perovskite as well as the H bonding between the oxygen atom of the additive's carbonyl group (CO) and the $-N-H$ group of FA^+. Reproduced from ref. 153 with permission from Elsevier Ltd, copyright 2021. (c) Schematic illustration of the presence of iodine vacancy in the $[PbI_6]^{4-}$ octahedra of the perovskite lattice and its passivation with the $-COO^-$ of the cesium trifluoroacetate additive. Partial substitution of FA^+ and MA^+ with the smaller ionic size Cs^+ of the additive at the A-site. Blocking of moisture ingression by trifluoride methyl ($-CF_3$). Reproduced from ref. 155 with permission from Elsevier B.V., copyright 2021. (d) Schematic illustration of the bonding interactions of the $P\!=\!O$ group (deep gray-red balls and stick) of ethylene diamine tetramethylene phosphonic sodium with the Pb^{2+} (green ball) of the perovskite as well as the formation of H bonds with the perovskite through I–H (red ball connected to the light gray ball by a broken yellow line). Reproduced from ref. 158 with permission from Elsevier B.V., copyright 2023. (e) N 1s XPS spectra of bare perovskite (depicted as PVK) on ITO, bare PEIE on ITO and perovskite capped with PEIE at 0.015%, 0.025% and 0.05% concentrations. The FA group of the perovskite in gray is depicted as peak 1. The $R-NH_2$ group of PEIE in purple is depicted as peak 2. The protonated $R-NH_3$ group of PEIE in red is depicted as peak 3. (f) XPS peak ratio of peak 3 to peak 1 extracted from N 1s XPS spectra fitting curve (red square). Shifts in binding energy of Pb 4f (green circle), I 3d (orange circle) and FA (black circle) peaks of PVK/PEIE relative to bare perovskite. Shifts in the binding energy of $R-NH_2$ peaks of PEIE/PVK (purple circle) relative to bare PEIE on ITO. Negative values indicate shifts to lower binding energy. (g) I 3d and (h) Pb 4f XPS spectra of PVK/PEIE at 0.015%, 0.025% and 0.05% concentrations. Reproduced from ref. 143 with permission from Elsevier Inc., copyright 2022.

This journal is © The Royal Society of Chemistry 2025

J. Mater. Chem. A, 2025, 13, 32964–33011 | 32985

tetramethylene phosphonic sodium can adequately secure Pb in the perovskite lattice, preventing Pb leakage.[158] As shown in Fig. 5(d), it achieves this by chelating with the Pb^{2+} (green ball) of the perovskite through its P=O group (deep gray-red balls and stick) to achieve a strong coordination interaction. It also eliminates anion vacancies and inhibits ion migration by forming H bonds with the perovskite through I–H (red ball connected to the light gray ball by a broken yellow line). Its multiple Pb^{2+} chelation sites effectively suppress various non-stoichiometric lattice defects and enhance moisture resistance.

Such strategic multiple bonding interactions can simultaneously improve the perovskite absorber layer and the ETL qualities as well as their interface which is prone to non-radiative recombination losses.[159,160] An approach is to initially add a 4-trifluoromethyl-benzamidine hydrochloride additive containing the $-CF_3$–amidine cation and Cl^- into a SnO_2 colloid solution.[161] The F^- and Cl^- passivate the oxygen vacancy. They also coordinate with the undercoordinated Sn^{4+} defects. F^- forms H bonds with the perovskite's FA^+, reducing cation migration and increasing crystallization. It coordinates with Pb^{2+} to passivate Pb defects. The additive can also passivate cation and anion vacancies through electrostatic interactions with perovskites. The modification suppresses the agglomeration of SnO_2 nanoparticles, passivates bulk and interfacial defects and releases tensile strains in perovskite films. Similar interface modification has also been achieved with ferrocenyl-bis-thiophene-2-carboxylate[162] which proved to be more effective in the n–i–p structure compared to the p–i–n structure which possesses deep-level traps of minority carriers at the perovskite surface.[79,143] Depth profiling analysis showed that such ETL/perovskite layer interaction can be facilitated by the sublimable phenylethylammonium cation which ensures better crystal orientation and compact film especially for all-inorganic perovskites (e.g., $CsPbI_{3-x}Br_x$) during film growth. X-ray photoelectron and UV-Vis spectroscopies showed that the cation ensures a near uniform distribution of the Br^- in the lattice. It yielded reduced recombination losses as evident from electrochemical impedance spectroscopy and space-charge-limited current results.[163] It reveals the defect passivation capacity of ammonium and aromatic ammonium cations which can passivate both positively and negatively charged defects in the perovskite structure. They can penetrate grain boundaries and passivate surface defects. Phenylammonium hydroiodide salts with different alkyl chain lengths have been shown to influence the perovskite thin film properties and device performance with phenylpropyl ammonium iodide making the best impact due to its most ideal alkyl chain length.[164]

Furthermore, the multifunctional characteristics of passivation agents are significantly evident in polymer additives which could be seen in terms of surface and grain boundary passivation as well as charge transport and collection improvement. The versatility of passivating agents accords them the capacity to simultaneously passivate different forms of defects which can be vacancies, interstitials, antisites, dissociative interstitials etc. This has been demonstrated in a multiple-defect management strategy using three types of chemical bonds of a pyridine-containing polymeric agent[139]

which fills the I^- vacancy by forming coordination bonds with PbI_x, reducing the perovskite's distorted octahedra. It forms H bonds with the ammonium cations, eliminating organic vacancies as well as deep-level antisite defects. It also creates supramolecular halogen bonds with dissociated interstitial I^-, blocking their action as electron traps. In addition, vinylaniline trifluoromethanesulfonate stabilizes the perovskite PbI_6 octahedra via the same mechanism.[145] It forms poly(vinylaniline) cations through UV polymerization which exerts compressive stress on the PbI_6 frameworks and inhibits interfacial ion migration under the operating conditions. To gain more insight into this, perovskite/polymer multi-mode interactions can be correlated with specific deep-trap states by combining deep-level transient spectroscopy and DFT.[143] This can be done by adopting polyethylenimine which is stable to moisture as well as thermally stable. It exhibits configurations such as linear polyethylenimine, branched polyethylenimine and ethoxylated polyethylenimine.

Unlike the N 1s X-ray photoelectron spectroscopy (XPS) spectra of bare perovskite (depicted as PVK) and poly-ethyleneimine (depicted as PEIE) coated on ITO which show single FA and $R-NH_2$ peaks at 400.57 eV and 399.3 eV respectively, the N 1s XPS spectra in Fig. 5(e) show a new XPS peak at 401.98 eV which corresponds to protonated amines ($R-NH_3$), resulting from a reaction between perovskite and PEIE (PVK/PEIE). The protonating process becomes saturated with increasing concentration of PEIE as shown in Fig. 5(f) where the XPS peak area ratio of $R-NH_3$ and FA (depicted by $R-NH_3$/FA) increases until the maxima at 0.025% PEIE. Similarly, increased PEIE ratio leads to peak shifts in the I 3d and Pb 4f XPS peaks of PVK/PEIE shown in Fig. 5(g and h) with the inflection point coinciding with the saturation point of protonation (0.025% PEIE) as shown in Fig. 5(e). The shifts of N, I, and Pb peaks can be attributed to the high density of PEIE functional groups, good coverage of PEIE polymer which reduces perovskite surface reaction sites and multi-mode interactions between PEIE and perovskite. In this process, in situ protonation can significantly passivate and reduce the deep-level traps due to inherent chemical agents at the perovskite surface unlike the use of conventional ex situ protonated and non-protonated groups which involve physisorption and metal-chelation[165–167] and are unable to create this effect. The strong bonding resulting from the perovskite/polymer interaction favors high operational stability.

Steric effects resulting from the physical size and shape of these additives play a crucial role in perovskite passivation.[168,169] In particular, molecules with specific structures and functional groups can bind to defects such as dangling bonds, vacancies and grain boundaries, eliminating their harmful effects.[169,170] The influence of the passivating agents on the perovskite surface, defect sites, charge transport, device stability and performance can be controlled by strategically choosing passivation agents with specific steric properties. This is achieved due to steric hindrance which manages their accessibility and binding to the defect sites based on size and shape. An extremely large molecule may be unable to effectively passivate certain defects due to ineffective accessibility and an extremely

32986 | J. Mater. Chem. A, 2025, **13**, 32964–33011

This journal is © The Royal Society of Chemistry 2025

small molecule may be unable to achieve adequate stabilization through passivation. Hence, the ideal size of passivating molecules must be determined to maximize defect passivation and enhance charge separation and transport within the perovskite bulk and across the interfaces. For example, due to the ideal size, guanidine iodide (GAI) can be incorporated into $FA_{0.75}MA_{0.25}SnI_3$ perovskite to achieve ionic compensation which facilitates defect healing in the lattice of the deposited thin film.[171] As shown in Fig. 6(a), GA^+ compensates the organic cation vacancies present in the pristine sample during thermal annealing and strengthens the perovskite crystal structure. It also creates an I-rich condition capable of healing the iodine vacancies. In particular, as shown in Fig. 6(b), the GAI-modified perovskite film at 15% optimal GAI ratio exhibits thermal stability as evident in the stable morphology with increasing annealing time. This can be attributed to the effective lattice incorporation of GA^+ and I^- as well as their compensation for ionic defects. GAI can also offer effective surface protection during annealing by passivating the surface halide vacancy through H bonding. Furthermore, these defects can be managed through the introduction of natural alkaloid passivation agents such as adenine and cytosine.[172] The molecular structures of the alkaloids allow for the adjustment of the electron cloud density distributions on different functional groups, boosting their passivation effect. These structures facilitate coordination bonding with uncoordinated Pb^{2+} leading to reduced Pb^{2+}-based defects. They also favor H bonding between $-NH_2$ and I^-/Br^-, reducing I^-/Br^- vacancies. A better inductive effect and electron cloud of cytosine which possesses an oxygen atom give it a more effective passivation effect than adenine.

Similarly, steric hindrance governs the optimal interaction of 2D perovskite layers with 3D perovskite films to form a 2D/3D heterostructure exhibiting passivated defects and improve stability. The heterostructure regulates interfacial properties and energy level alignments.[173] The alkyl chain length of the A-site cation can be varied to optimize this effect. Wang *et al.* found hexaneammonium bromide to be the champion A-site alkylammonium halide to optimize energy level alignment and reduce interfacial defect density. The alkyl chain length also influences the degree of hydrophobicity, charge transport and cation migration across the perovskite/HTL

Fig. 6 (a) Schematic illustrations comparing the crystallization processes of control and GAI-modified $FA_{0.75}MA_{0.25}SnI_3$ perovskite films. (b) Plane-view SEM images of 15% GAI-modified $FA_{0.75}MA_{0.25}SnI_3$ perovskite films annealed at 100 °C for 5, 10 and 15 min. Reproduced from ref. 171 with permission from Elsevier B.V., copyright 2022. (c) Schematic illustration of the energy level alignment facilitated by 4-fluoro-phenethyl-ammonium chloride. Reproduced from ref. 170 with permission from Elsevier B.V., copyright 2021.

This journal is © The Royal Society of Chemistry 2025

J. Mater. Chem. A, 2025, **13**, 32964–33011 | **32987**

interface.[164,174,175] Notably, many high-performing perovskite PV devices are based on 2D/3D interfaces. The dimensional reduction on the 3D perovskite surface due to interaction with a 2D ligand cation can be revealed by *in situ* GIWAXS and DFT simulations as seen with $(MAPbBr_3)_{0.05}(FAPbI_3)_{0.95}$ perovskite exposed to vinylbenzylammonium where the ligand cation strongly binds the perovskite fragments due to phenyl ring stacking interactions.[176] Such ligands can further passivate deep level defects by filling cation vacancies in 3D perovskite layers. Their halogenated forms such as that derived from brominated 2-bromophenethylammonium iodide can form strong H bonds with the organic cations, interact with the $[PbI_6]^{4-}$ inorganic framework to fill halide vacancies and form anion bonding based on the Br^- component.[177]

The size of organic cations in ionic liquids is also critical to their interfacial chemical interaction and defect passivation. Ionic liquids such as poly-1-vinyl benzyl-triethylammonium chloride and poly-1-vinyl benzyl-3-methylimidazole chloride passivate defects and immobilize ions by forming alkyl-based ionic polymer networks achieved through bonding interactions controlled by steric hindrance.[58] Poly-1-vinyl benzyl-triethylammonium chloride shows higher binding energy with perovskites as it can achieve stronger electronic coupling and better complexation due to its $(N(-CH_3)^{3+})$ quaternary cation. The quaternary cations can reduce interfacial trap density by filling the organic cation vacancies in the perovskite lattice.[141] Furthermore, suitable steric characteristics of polymeric passivating agents such as sterically accessible ester functional groups can effectively passivate charged defects on perovskite surface. This is evident in the investigation of the structural effects of polyvinyl acetate, polyethylene glycol and poly(9-vinylcarbazole) molecules on the PSCs which revealed that polyvinyl acetate possesses a Lewis base functional group with minimized steric hindrance and strongest electron-donating ability. It gives the most effective surface defect passivation on the perovskite film as well as the most enhanced carrier diffusion.[168] Liu *et al.* showed that such ester groups can transform into a carboxylic group during thin film annealing. This further reduces steric hindrance and enhances interactions with the perovskite components, contributing to the structural integrity and the defect passivation.[169]

Nevertheless, when designing passivating agents, it is important to consider the trade-off between steric effects and electronic effects (*e.g.*, charge distribution and electronegativity). In particular, charge transport simulation can predict the difference between the effects of passivation and charge extraction on the overall device performance. Guidelines for the rational selection of passivating molecules exhibiting optimal steric properties capable of achieving high-performance and stable PSCs must be established. Passivating agents with structures geometrically matching those of perovskites, *e.g.*, 1,3-propanediammonium diiodide and 1,4-phenyl-enediammonium diiodide have been proposed.[178] It shows that a deep understanding of the steric effects can facilitate the development of high performance and stable PSCs.

Dipole-induced energy level alignment is another crucial passivation process in PSCs. It involves a strategic manipulation of energy levels at the perovskite/CTL interface by inserting molecules with specific dipole moments to eliminate losses due to energy level mismatch and achieve stability in PSCs.[170,179,180] Depending on dipole direction, the process creates an electrical dipole layer which induces an upward or downward shift in the perovskite energy levels which can be measured *via in situ* UPS.[181,182] Such shifts eliminate surface defects, reduce non-radiative recombination and improve charge collection. Hence, a rational selection of dipole molecule and orientation is required. Such dipole molecules include triphenylphosphine oxide which induces upward surface band bending in perovskites, improving charge selectivity and stability. Used through an antisolvent process, it modifies the perovskite/HTL interface by passivating the perovskite layer defects through the formation of a Pb–O bond with undercoordinated Pb^{2+}. The π conjugated structure of its benzene rings facilitates charge transfer across the perovskite/HTL interface leading to negligible hysteresis and long-term stability.[179] Functionalizing with highly electronegative elements (*e.g.*, F) further increases the dipole moment as can be seen with ammonium salts which creates interfacial dipoles with varying directions, affecting electron and hole extraction differently. In particular, Wang *et al.* demonstrated the suppression of charge recombination in $CsPbI_2Br$ film with the fluorinated ammonium salt, 4-fluorophenethylammonium chloride. This is facilitated by the energy level alignment effect as shown in Fig. 6(c), leading to improved device parameters, *i.e.*, V_{oc} and FF. Its hydrophobicity improves the film's stability against moisture.[170]

Other dipole molecules such as alkylamines and chlorine-terminated silanes have also shown beneficial interface passivation and energy level alignment. Alkylamines can enhance stability, improve defect passivation and finetune energy levels by varying the alkyl chain length.[183] As revealed by hybrid experimental and DFT studies, chlorine-terminated silanes achieve this by decreasing perovskite WF and achieving ohmic perovskite/HTL contact.[180] This effect is further enhanced *via* ion–dipole interactions which suppress the formation of harmful interstitial iodine. The interstitial iodine can be generated through deprotonation of organic cations and oxidation of iodide due to interactions between the perovskite's organic components (*e.g.*, FAI) and Lewis acid species in metal oxide CTL (*e.g.*, NiO_x). The CTL surface is modified with self-assembled monolayers such as MeO-2PACz and 2PACz exhibiting a large dipole moment and an ultra-thin layer of metal halide such as potassium fluoride. This prevents direct contact between the perovskite and the CTL and the increased WF of the CTL enhances hole transport, suppressing non-radiative recombination.[184]

Notably, defect passivation by energy level alignment optimization significantly increases parameters, *e.g.*, V_{oc}, FF and PCE and the stability of the device under various conditions (*e.g.*, light, heat, humidity). *In situ* studies using time-resolved surface photovoltage which reveal the carrier extraction and recombination dynamics in the presence of dipole molecules give deeper insight into ways to maximize these merits.[181] As listed in Table 1, various methods have been used to realize effective passivation of the perovskite systems. However, to

32988 | *J. Mater. Chem. A*, 2025, **13**, 32964–33011

This journal is © The Royal Society of Chemistry 2025

further advance the passivation protocol, extensive research into the correlation of the multi-component nature of perovskites with existing and new passivation agents is required.

6 Phase stabilization

The PV effect is evident when the MCPs are in the α phase which has demonstrated high PCE (>25%).[15,162,185,186] Several factors commonly trigger a deviation to the non-photoactive δ phase. Such factors border on the complexity of their chemical composition which propels their poor intrinsic stability and limits their commercialization.[53,107] Studies on the perovskite degradation mechanisms have shown that the choice and ratio of the chemical components as well as environmental factors significantly influence the perovskite structural stability. Notably, the occupation of the A-, B- and X-sites of the MCP with multiple elements also heightens the vulnerability of this class of materials to phase segregation and ion migration.[34] Although strategies such as precursor material adjustment, solvent engineering, film growth method optimization, *etc.*, can effectively control the fundamental compositional and phase behavior of the materials in the presence of various stressors, it is important to further understand the mechanistic aspects of the various degradation pathways in the thin film and solar cell devices so as to address the issue.

There may not be an ideal experimental evaluation of the perovskite materials' phase composition as it may vary as a function of the probing depth. Moreover, wide area depth profile analysis can reveal the material composition and depth-dependent changes in atomic ratios at every stage of the film growth.[187] The molar phase fractions obtained from reciprocal space maps show in Fig. 7(a) that PbI_2 can be found preferentially near the film surface compared to the bulk in an FA-based perovskite. Nonetheless, the excess PbI_2 conditions, PbI_2 phase segregation and hexagonal phase formation commonly associated with the FA-based perovskites can be mitigated by stabilizing the material and enhancing the purity of the black cubic phase through the addition of Cs^+ and Rb^+ cations which possess smaller ionic radii. The azimuthal integration of the radially distributed intensity of the reciprocal space maps in Fig. 7(b) shows that the simultaneous addition of Cs^+ and Rb^+ guarantees a significant increase in the cubic phase uniformity which can be almost 100% in a quadruple FA:MA:Cs:Rb cation perovskite unlike in the triple cation perovskite obtained by the addition of only Cs^+. In general, the addition of these cations can guarantee a significant cubic phase purity improvement from about 45% to almost 100% within the resulting multi-cation material.

In order to isolate depth dependent composition variation, probing the Ga Kα hard XPS 45 nm into the bulk of the perovskites can give a more reliable chemical composition quantification and the distribution of alkali-metal than conventional XPS.[188] The addition of RbI induces nearly homogeneous distribution of both Cs^+ and Rb^+ at the surface and significantly reduces the surface I^- vacancies, mitigating the imperfections observed with the Cs-only perovskite. Although the Rb^+ may not be fully incorporated into the perovskite lattice, RbI plays an

important role in increasing the thermal stability of the perovskite material such as $FA_{1-x}Cs_xPbI_3$ as it serves as an I^- source, filling the iodine vacancy sites in the lattice. It also forms $RbPbI_3$ passivation agent at the grain boundaries of the films. This increases the ion migration barriers at the surface, stabilizes the $[PbI_6]^{4-}$ framework, reduces the lattice decomposition, suppresses the release of the organic and Cs^+ A-site cations at the surface, reduces the formation of PbI_2 and the thermal decomposition to metallic lead (Pb^0) and I_2. *In situ* XPS of the role of cations in the thermal- and moisture-induced surface degradation of mixed cation perovskites such as $FA_{1-x}Cs_xPbI_3$ and $(FA_{1-x}Cs_x)_{1-y}Rb_yPbI_3$ (x, y = 0.1, 0.05) grown under ambient conditions showed that both compositions exhibit superior moisture stability relative to the $MAPbI_3$ perovskite.

To further investigate the material composition–stress (*i.e.*, light and heat) relationships, compounds such as $MA_{0.15}$-$FA_{0.85}PbI_{2.55}Br_{0.45}$, $Cs_{0.1}MA_{0.15}FA_{0.75}PbI_{2.55}Br_{0.45}$, $Cs_{0.15}FA_{0.85}$-$PbI_{2.55}Br_{0.45}$, $MA_{0.15}FA_{0.85}PbI_3$, $Cs_{0.1}MA_{0.15}FA_{0.75}PbI_3$ and $Cs_{0.15}FA_{0.85}PbI_3$ can be evaluated.[54] A combination of analytical techniques showed that Br^--containing mixed-halide perovskites exhibit lower photostability compared to the I^- containing counterparts. Under light-induced photochemical aging, they undergo facile recrystallization which damages the surface morphology with the appearance of isolated areas of large domains and voids. In the dark and under mild heating (55 °C), δ-$FAPbI_3$ and PbI_2 can be confirmed as the main decomposition products. Metallic Pb and other volatile products such as I_2 are formed after light exposure. Notably, $Cs_{0.15}FA_{0.85}PbI_3$ demonstrated outstanding stability. DFT calculations showed that the formation of interstitial vacancy halide pair defects in the Br^--containing mixed-halide perovskites is thermodynamically driven by hole coupling. This accelerates the perovskite degradation as it reduces their barrier of diffusion relative to that of the I-only perovskite. MA^+ readily decomposes into volatile NH_3 and CH_3I, contributing to the poor stability. Therefore, achieving Br- and MA-free mixed cation halide perovskite materials may be a promising strategy to realize high material stability.

Also, the device stability is significantly jeopardized by the same stressors. In particular, moisture adversely affects PSC performance. It induces phase transition and segregation in the absorber layer.[50,188,189] Hence it is important to understand the moisture–perovskite relationship in order to gain insights into the degradation mechanisms of MCPs and to optimize their device performance and stability. Structural and chemical changes in $Cs_{0.05}(MA_{0.15}FA_{0.85})_{0.95}Pb(I_{0.84}Br_{0.16})_3$ perovskite thin film after aging under controlled humidity can be revealed through a combined microscopic, spectroscopic, diffractometric techniques and theoretical calculations.[51] In particular, degradation products from the perovskite layer and changes in optical and chemical properties reveal the formation of different phases such as PbI_2, inorganic mixed-halide $CsPb(I_{0.9}Br_{0.1})_3$ perovskite and Pb-rich $CsPb_2(I_{0.74}Br_{0.26})_5$ perovskite. These phases are stable as they exhibit high crystallinity and create unique geometrical shapes which have profound influence on the optoelectronic properties of the thin film.
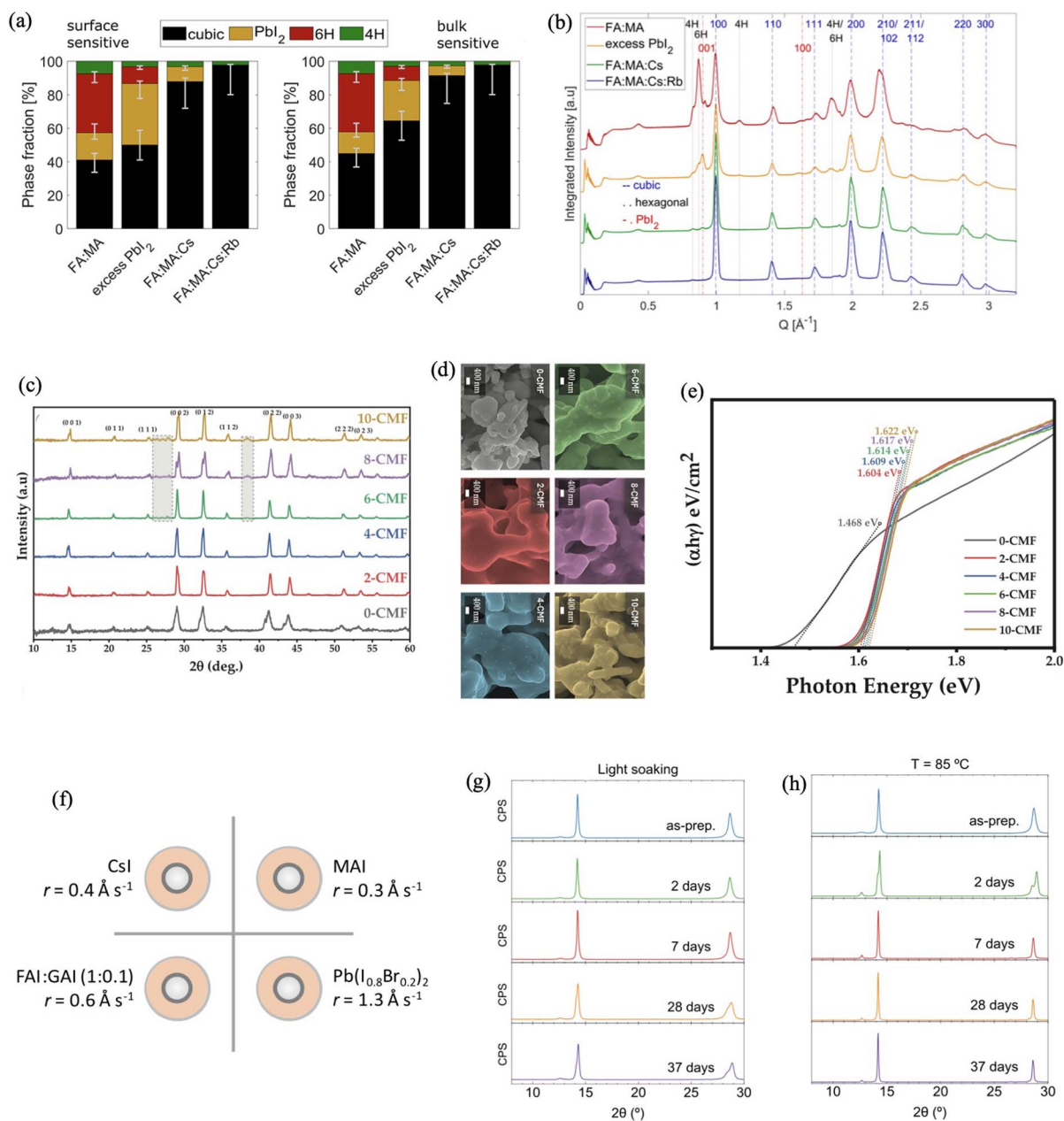
This journal is © The Royal Society of Chemistry 2025

J. Mater. Chem. A, 2025, **13**, 32964–33011 | **32989**

Fig. 7 (a) Film composition dependent cubic, PbI_2 and hexagonal phase fractions, determined by integrating peaks from radial intensity profiles of reciprocal space maps at surface-sensitive and bulk-sensitive incidence angles. The error bars are due to compositional uncertainties and experimental statistics. (b) Radial peak intensity distribution of cubic, hexagonal and PbI_2 phases of perovskite obtained from reciprocal space maps. Reproduced from ref. 187 with permission from American Chemical Society, copyright 2021. (c) Comparison of PXRD spectra, for the percentage of Cs^+ incorporated into FA^+/MA^+ mixed-cation perovskites denoted by 0, 2, 4, 6, 8, 10-CMF. (d) Comparison of high magnification FESEM images for the percentage of Cs^+ incorporated into FA^+/MA^+ mixed-cation perovskites denoted by 0, 2, 4, 6, 8, 10-CMF. (e) Comparison of Tauc plot with optical bandgap values for the percentage of Cs^+ incorporated into FA^+/MA^+ mixed-cation perovskites denoted by 0, 2, 4, 6, 8, 10-CMF. Reproduced from ref. 190 with permission from Wiley-VCH GmbH, copyright 2024. (f) Schematic illustration of the source layout for the vacuum deposition of CsMAFAGA quadruple-cation perovskite films showing precursor materials and corresponding deposition rates (r) in Å s^{-1}. XRD patterns obtained from the stability test for the quadruple-cation CsMAFAGA perovskite films by periodic *ex situ* measurements during (g) light soaking and (h) thermal stress. Reproduced from ref. 196 with permission from American Chemical Society, copyright 2022.

Notably, the moisture induced degradation mechanisms of CsMAFA perovskite is governed by ion migration, organic cation volatilization and phase transition. Microscopic and XRD analyses show that PbI_2 grows along a preferential orientation (hexagonal [001] axis). The $CsPb(I_{0.9}Br_{0.1})_3$ crystallizes into the orthorhombic ordered (*Pnma*) configuration which further transforms into tetragonal (*P4/m*) $CsPb_2(I_{0.7}Br_{0.3})_5$. Hence, beyond ion migration, escape of organic cations and phase transition, the humidity effect on CsMAFA also includes the recrystallization of the degradation residue. The phase

32990 | *J. Mater. Chem. A*, 2025, **13**, 32964–33011

This journal is © The Royal Society of Chemistry 2025

transition can be mitigated through a dry and solvent-free mechanochemical mixing of separately prepared precursor materials $FAPbI_3$, $MAPbBr_3$ and $CsPbI_3$ microcrystals at an optimized ratio to achieve a more stable triple cation perovskite.[190] The mixing and effective lattice incorporation of MA^+ and Cs^+ cations and substitution of FA^+ in the parent $FAPbI_3$ can be confirmed by the observed changes in elemental composition, morphology, lattice strains and band gap as evident from FESEM analysis, XRD patterns and UV-Vis-NIR spectroscopy. For example, the XRD patterns in Fig. 7(c) confirm successful mixing of the precursor materials. They also show that optimal mixing must be achieved to avoid the appearance of peaks attributable to δ-$CsPbI_3$ (highlighted part) after the incorporation of $\geq 6\%$ Cs^+. This can explain and control the increasing granular patches observed on the SEM images of the triple cation perovskites in Fig. 7(d). Successful mixing can also be confirmed as shown in Fig. 7(e) where the individual optical bandgaps of $FAPbI_3$, $MAPbBr_3$ and $CsPbI_3$ powders which are 1.41 eV, 2.18 eV and 2.71 eV, respectively, change to the range of 1.468–1.622 eV of the triple cation perovskites depending on the Cs^+ ratio.

The stability can be further advanced by expanding the lattice to exhibit a quadruple-cation A-site. This can be achieved by a two-step sequential deposition involving the addition of 1D polymorphs of mixed orthorhombic δ-$RbPbI_3$ and δ-$CsPbI_3$ to a PbI_2 precursor solution to form a mesostructured hexagonal film and speed up the heterogeneous nucleation as well as the percolation of additional cations such as FA^+/MA^+ within the PbI_2 film to form the desired quadruple-cation cubic α-structure.[191] Spectroscopic measurements can confirm the degree of integration and ratios of the multiple cations making up the resulting 3D perovskite lattice. Moreover, when applied as absorber layers in solar cells, the MCPs are exposed to light irradiation and the operational temperature of the device.[48,192,193] Consequently, the device stability is limited due to the thermal instability of MA^+, structural instability of Cs^+ and the phase segregation of mixed halide components of the perovskite absorber layer.[34]

The degradation of a perovskite absorber layer such as $(FA_{0.73}MA_{0.27})Pb(I_{0.945}Br_{0.055})_3$ in the presence of light and temperature is influenced by free carriers as evident from a combination of analysis based on *in situ* electron paramagnetic resonance spectroscopy, *in situ* X-ray diffraction, thermogravimetric and calorimetric analysis.[194] The effect of the free radicals on the observed structural modification and degradation can be seen in the form of gas release and heat exchange. The two-stage degradation process involves a non-radical-based degradation in the first stage with the release of MA^+ and I^-. Moreover, the impact of the free radicals is more profound towards the final (or second) stage of the thermally induced decomposition where they localize on FA^+ to release fragments of formamidine. Unlike in the dark, exposure to the light stressor also leads to a rise in spin concentration which correlates with increased degradation. The sensitivity to light and other ambient conditions prevents the suitability of simple perovskites such as the inorganic $CsPbI_3$ perovskite as the top cell absorber layer in tandem solar cells despite their ideal

bandgap. In particular, the α-phase of $CsPbI_3$ perovskite (bandgap *ca.* 1.7 eV) reverts to the δ-phase with a bandgap *ca.* 2.8 eV not suitable for PV application.

The stability issue is most commonly mitigated by the application of additives through solution processes. Such a strategy can be challenging with vacuum deposition. Moreover, vacuum deposition can yield better film quality and is more compatible with inorganic precursor materials. Therefore, Susic *et al.* demonstrated the incorporation of bulky cation dimethylammonium iodide (DMAI) during the room temperature vacuum deposition of $CsPbI_3$ perovskite films through co-sublimation of CsI and PbI_2 precursors to achieve a mixed cation $CsDMAPbI_3$ perovskite.[195] The non-ambipolar charge transport effect of the material gives it superior performance in an n–i–p device structure. The thin film quality and corresponding device performance can be further improved with the addition of a third A-site cation such as FA^+ or MA^+ in a four-source deposition process with MA^+ yielding better PV response.[196] The multi-cation perovskite forms a high-quality layer on textured silicon, making it a promising material for the top cell absorber layer in perovskite/silicon tandem solar cells. As shown in Fig. 7(f), at optimal deposition rates and precursor mixing, the multisource deposition can be used to expand the A-site to achieve quadruple cation perovskites such as the CsMAFAGA perovskite. Quadruple cation perovskites are an improvement on the triple cation analogues as they confer better thermal stability on the materials due to the presence of GA^+. The enhanced photo- and thermal-stability of the quadruple perovskite can be seen in Fig. 7(g and h), where no new diffraction peaks appear after 37 days of continuous light soaking and heating (at 85 °C) respectively.

The benefits of GA^+ is attributed to the formation of numerous H bonds with favorable orientation within the inorganic framework, ability to partially incorporate into the perovskite lattice without breaking the 3D structure due to its permissible ionic radius and the similarity in the sublimation properties of GAI and FAI making it easy to simultaneously sublime them from the same source. As revealed by microstructural analysis, GA^+ is initially not incorporated in the lattice but accumulates at the grain boundaries. However, a transition to a lower-symmetry perovskite phase takes place during thermal stressing which ultimately stabilizes the cubic phase into a larger unit cell, indicating the incorporation of some GA^+ into the lattice.

Thermally induced degradation and transition of multi-cation perovskite films can be quantitatively analyzed with respect to changes in film thickness and surface roughness using spectroscopic ellipsometry within a wide spectral range. Based on this technique, MA- and MA-free MCPs have been studied at temperatures between 80 °C and 120 °C.[197] The decomposition can be monitored based on the various compositional dynamics such as relative changes in organic cation ratios, formation of PbI_2 and non-perovskite δ-$CsPbI_3$ phases which can be evident by fitting the obtained refractive indices. It shows that MA^+ can be almost completely lost after 100 min of thermal annealing at 120 °C while the MA-free perovskite exhibits better stability under similar conditions

This journal is © The Royal Society of Chemistry 2025

J. Mater. Chem. A, 2025, **13**, 32964–33011 | **32991**

but shows faster degradation at lower temperatures, *e.g.*, 100 °C due to phase instability resulting from the formation of δ-$CsPbI_3$ and PbI_2. Varying the temperature of MCPs in the presence of light can change their compositional characteristics.[49,53] At ideal temperatures, the organic cation (*e.g.*, MA^+) otherwise known to limit perovskite stability can in fact be a stability-enhancer while the inorganic cation (*e.g.*, Cs^+/Rb^+) can be a stability limiter.[49] In particular, increasing the concentration of MA^+ or decreasing the concentration of Cs^+ in the perovskites at high temperatures (>100 °C) can jeopardize their photothermal stability. However, the effect is reversed at

temperatures <100 °C. This behavior is based on the kinetics and E_a of perovskite decomposition. The stability reversal in the perovskite films is transferable to the device as the perovskite layer made of optimized cation ratio exhibits remarkable stability at 30 °C.

These efforts have shown that the crystallinity, optoelectronic properties and stability of multi-cation perovskites strongly depend on the fabrication method with the main focus on composition ratio control and crystal growth mechanism. Furthermore, the light-induced degradation in triple-cation PSCs at a constant voltage near the maximum power point
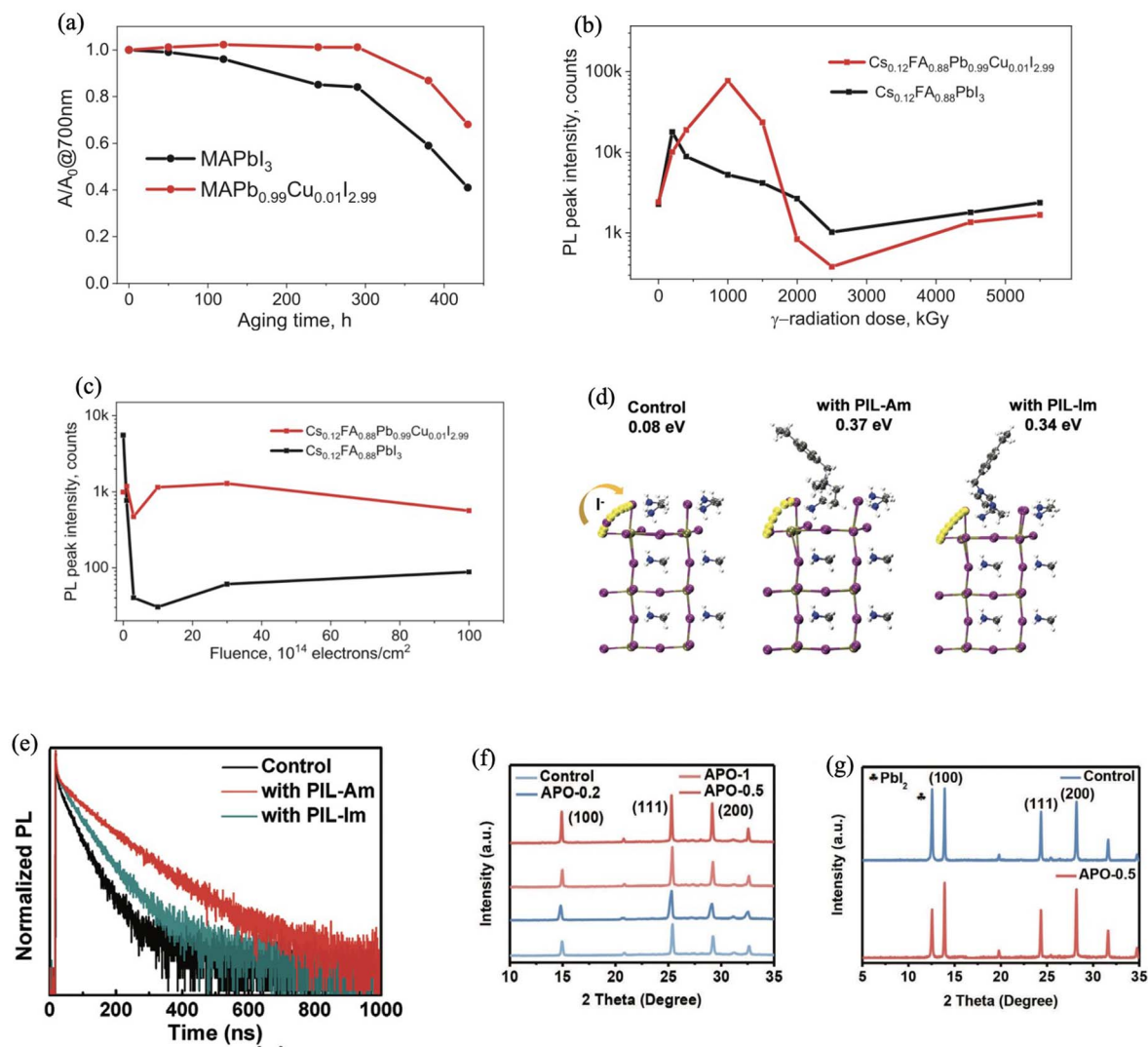

Fig. 8 (a) Photostability comparison of pristine and Cu^{2+}-doped films showing the dynamics of their normalized absorbance under illumination at 700 nm, 85 mW cm^{-2} and 32 °C. (b) Comparison plots of the PL intensity responses of $Cs_{0.12}FA_{0.88}PbI_3$ and $Cs_{0.12}FA_{0.88}Pb_{0.99}Cu_{0.01}I_{2.99}$ as a function of γ-radiation dose. (c) Comparison plots of the PL intensity responses of $Cs_{0.12}FA_{0.88}PbI_3$ and $Cs_{0.12}FA_{0.88}Pb_{0.99}Cu_{0.01}I_{2.99}$ as a function of electron fluence. Reproduced from ref. 200 with permission from The Hong Kong Polytechnic University and John Wiley & Sons Australia, Ltd, copyright 2024. (d) I-migration pathways (denoted by the yellow trajectory) and migration energies as obtained from nudged elastic band calculations for the control, poly-1-vinyl benzyl-triethylammonium chloride (PIL-Am) and poly-1-vinyl benzyl-3-methylimidazole chloride (PIL-Im) perovskite films. (e) Time-resolved photoluminescence (TRPL) spectra of the control, poly-1-vinyl benzyl-triethylammonium chloride (PIL-Am) and poly-1-vinyl benzyl-3-methylimidazole chloride (PIL-Im) perovskite films. Reproduced from ref. 58 with permission from Wiley-VCH GmbH, copyright 2022. (f) XRD patterns of annealed *N*-acetyl-L-phenylalanine treated $Cs_{0.10}MA_{0.15}FA_{0.75}PbI_3$ perovskite films showing 0.5 mg ml^{-1} of *N*-acetyl-L-phenylalanine as the optimal doping ratio. (g). XRD pattern of the buried interface for the control and *N*-acetyl-L-phenylalanine treated $Cs_{0.10}MA_{0.15}FA_{0.75}PbI_3$ perovskite films after stripping. Reproduced from ref. 212 with permission from Wiley-VCH GmbH, copyright 2024.

32992 | *J. Mater. Chem. A*, 2025, **13**, 32964–33011

This journal is © The Royal Society of Chemistry 2025

and for different regions of the solar spectrum is wavelength dependent as high-energy photons induce significant performance deterioration in the device.[198] In particular, shorter wavelengths 300–500 nm can be more harmful to the device while longer wavelengths can be less harmful over a test period of 250 h as indicated in the device efficiency as well as ideality factor which is lower in the dark and at wavelengths >500 nm but higher at full spectrum and shorter wavelength. Hence, the wavelength of the incident light must be considered so as to increase device life-span. The light-induced degradation results in device performance deterioration originating from the bulk decomposition of the perovskite absorber into PbI_2 and a decrease in the absorbance wavelength corresponding to the photoactive $\propto$-phase (650–800 nm) as revealed by XRD measurements and UV-vis-NIR spectroscopy respectively. The decomposition generates multiple trap states with low E_a values obtainable from thermally stimulated current measurements. Hence an energy-rich dose of light is injurious to PSCs.

Beyond the common stressors such as moisture, light and heat, other radiations such as gamma (γ) radiation can have profound effects on the stability of perovskite materials. Therefore, it is important to examine the radiation hardness of the materials. $(CsMA)PbI_3$, and $(CsMAFA)PbI_3$ have been shown to reasonably tolerate ultrahigh (i.e., up to 10 MGy) doses of γ rays without a major change in their absorption spectra.[199] However, they form Pb^0 after prolonged exposure. Infrared near-field optical microscopy revealed that the multication $(CsMAFA)PbI_3$ perovskite undergoes a facile phase segregation into MA^+-rich and FA^+-rich domains which is a new degradation pathway different from perovskite materials' responses to the common stressors. As shown in Fig. 8(a), partial substitution of the Pb^{2+} with Cu^+ can enhance the light and radiation hardness. The Cu^+ is spatially integrated into the $MAPbI_3$ lattice to form $MAPb_{1-x}Cu_xI_{3-x}$ and create a p-doping effect. The Cu^+ enhances the photostability of the perovskite film, preventing photolysis-induced Pb^0 formation.

As shown in Fig. 8(b), it also alters the radiation-induced degradation mechanism of double cation perovskites. While $Cs_{0.12}FA_{0.88}PbI_3$ degrades by phase segregation into δ-phase $FAPbI_3$ and a Cs-rich perovskite phase, $Cs_{0.12}FA_{0.88}Pb_{0.99}Cu_{0.01}I_{2.99}$ forms δ-$CsPbI_3$ and FA-rich perovskite phase, capable of significantly higher PL intensity at lower γ ray dosage and which exhibits better tolerance to high energy electrons as shown in Fig. 8(c).[200] High-intensity 170 keV pulsed (150 ns) proton irradiation, with a fluence of up to 10^{13} pcm^{-2} causes deterioration up to 20% and 50% specifically with low (2×10^{12} pcm^{-2}) and high (1×10^{13} pcm^{-2}) proton fluences respectively in multi-component $(Cs_{0.04}Rb_{0.04}(FA_{0.65}MA_{0.35})_{0.92}Pb(I_{0.85}Br_{0.14}Cl_{0.01})_3)$ PSCs because of non-radiative recombination losses from bulk and surface traps.[201] These irradiation fluences correspond to ca. 30 years of operation at low Earth orbit and exceeds harsh space conditions. It shows the extent to which multi-component PSCs can withstand high-intense short-pulse proton irradiation.

Other factors affecting the photo-stability of these materials can be related to bias conditions, i.e., V_{oc}, short-circuit current (I_{sc}) and maximum power.[198,202,203] Electric-field-induced ageing

reveals the cation dynamics in $Cs_{0.1}MA_{0.15}FA_{0.75}PbI_3$ perovskite films to involve the oxidation of I^- and the reduction of MA^+ and FA^+, resulting in the degradation of the film because of the depletion of the organic species and the formation of Pb^0 as evident from a combination of analytical methods such as infrared scattering scanning near-field microscopy (IR s-SNOM), PL-microscopy, SEM/EDX and ToF-SIMS.[204] The degradation also involves phase segregation with the formation of FA-, MA- and Cs-rich domains. FA^+ is more stable than MA^+ as it can be preserved in trace after 40 days of 1 V μm^{-1} field exposure unlike MA^+ which completely decomposes within a shorter period.

Also, halide mobility in the perovskite films influences the solar cell performance. Halide ion migration can occur through halide exchange within the bulk of the perovskite layer or between the perovskite and an adjacent layer. Although the bandgap can be tuned to achieve controlled absorption and emission within the visible region of the electromagnetic spectrum by varying halide ratios such as $Cl^- : Br^-$, $Br^- : I^-$, and $Cl^- : Br^- : I^-$ during the synthesis of mixed halide perovskites, the mixed halide films undergo phase segregation to form rich and poor sites under steady state illumination.[53,205,206] Interestingly, the phase segregation can be reversed to the original composition when the illumination is removed. Such segregation can be greatly suppressed by the introduction of multiple cations such as Cs^+ and FA^+ at the A site or by alloying the X site with Cl^-.[22,85,86] Although a mechanism based on the reversible Pb^{2+}/Pb^0 and I^-/I^{3-} redox photochemistry has been proposed for this phenomenon,[53] the photoinduced reversibility of the segregation can be jeopardized due to losses attributable to the volatility of I. For example, long-term irradiation of $MAPb(Br_{0.5}I_{0.5})_3$ films results in the evolution of I, leaving behind a Br-rich phases and this can be sped-up by hole trapping at I-rich sites in the perovskite lattice.

Because the photophysics of Pb-halide perovskites can be tuned via halide mixing, this class of material can be adapted for various optoelectronic applications such as simple and tandem solar cells. Their photodegradation and phase segregation into Br-rich and I-rich phases have been widely studied in order to fully understand the origin of these effects. Using a set of complementary techniques including in situ atomic force microscopy, Frolova et al. investigated the photodegradation of mixed-halide perovskite samples, i.e., $CsPbI_2Br$ and $Cs_{1.2}PbI_2Br_{1.2}$ in real time.[53] Halide phase segregation dynamics demonstrate that PbI_2-based groups are selectively displaced from the mixed halide perovskite grains and nucleate as a separate I-rich phase at the grain boundaries while the bulk assumes a Br-rich state. This effect is propelled by facile and reversible redox transitions between I^- and I^{3-} as well as Pb^{2+} and Pb^0. Excess CsBr in $Cs_{1.2}PbI_2Br_{1.2}$ improves its photostability. The photochemical decomposition of $CsPbI_2Br$ and $Cs_{1.2}PbI_2Br_{1.2}$ produces two different polymorphs of $CsPbI_3$, i.e., orthorhombic (yellow) and cubic (black) phases, respectively.

Notably, the ion migration-induced degradation can be eliminated by incorporating multifunctional polyionic liquids such as poly-1-vinyl benzyl-triethylammonium chloride and poly-1-vinyl benzyl-3-methylimidazole chloride additives which

This journal is © The Royal Society of Chemistry 2025

J. Mater. Chem. A, 2025, 13, 32964–33011 | 32993

can confer high stability on the devices.[58] The polyionic liquids create an ionic polymer network which passivates defects and immobilizes ions through the formation of physical barriers based on electrostatic interaction and steric hindrance as well as chemical bonding. Poly-1-vinyl benzyl-triethylammonium chloride can achieve this more than poly-1-vinyl benzyl-3-methylimidazole chloride as it is a quaternary ammonium-based additive exhibiting higher interaction energy with the perovskite due to stronger electronic coupling and additional complexation which raises the migration energy for the I^- ions as obtained from nudged elastic band calculations shown in Fig. 8(d). In particular, DFT calculations reveals that the higher binding energy of poly-1-vinyl benzyl-triethylammonium chloride with perovskite compared to poly-1-vinyl benzyl-3-methylimidazole chloride leads to better optoelectronic properties as supported by the prolonged carrier life-time shown in the time-resolved photoluminescence PL spectra in Fig. 8(e). This can be attributed to its cation defect passivation effect which suppresses interfacial nonradiative recombination as well as formation of a strong complex with the I^- anions, enabling ion immobilization.

Ion migration can be further suppressed by establishing entropy stabilization of the perovskite structure. This has been achieved in an all-inorganic halide perovskite nanocrystal prepared under ambient conditions by simultaneously incorporating multi-metal cations into the lattice.[207] The entropy stabilized perovskite exhibits near-unity quantum yield, excellent colloidal stability and monodispersity after prolonged ageing. This stems from the suppressed crystal defects, suppression of nonradiative recombination, stronger bond between secondary divalent ions and halide ions, increased defect formation energy and a more robust octahedral structure. In particular, low ionic migration in the perovskite semiconductor ensures stable and high device performance. The incorporation of MA^+ and Cs^+ cations as well as Br^- anions into the lattice of a precursor perovskite such as $FAPbI_3$ can achieve inch-sized stable FAMACs perovskite single crystal.[208] The cations and anion suppress the $FAPbI_3$ lattice stress as they are smaller compared to the FA^+ and I^- leading to lower ion migration, enhanced hardness, lower trap density, longer carrier lifetime and diffusion length, higher charge mobility and thermal stability and better uniformity.

Numerical analyses also validate the suppression of phase segregation in MCPs through the use of additives.[209,210] An example is the post-growth treatments of materials such as CsFAMAPbIBr thin films with formamidinium bromide (FABr).[210] Although charge carrier generation rate does not change after FABr treatment, recombination rate can be reduced by ca. 32% (e.g., from 7.27×10^{21} to 4.92×10^{21} cm^{-3} s^{-1}). Due to the suppressed phase segregation, the FABr-treated CsFAMAPbIBr-based PSC can yield higher efficiency than the pristine device. Uncontrollable crystallization and poor film quality as seen in the multi-cation perovskite made of FA-rich A-site can also catalyze the phase segregation. The creation of an intermediate phase capable of assisting the crystallization towards achieving high-quality films can be realized by the addition of phenformin hydrochloride (PFCl) into the precursor solution to form a PFCl.FAI intermediate phase which increases the nucleation rate, reduces the grain growth speed, limits the formation of the δ-phase and favors the orientational growth of the α-phase during crystallization.[142] The phenformin hydrochloride also passivates the positively and negatively charged defects through H and ionic bond formation.

The effect of the applied additives on the phase stability is dependent on the additive's molecular configuration as well as the perovskite composition. For instance, azaadamantane-based molecular modifiers such as N-methylated 1,3,5,7-tetra-azaadamantane with an iodide counterion exhibits a moderate stabilizing effect on $Cs_{0.10}MA_{0.15}FA_{0.75}PbI_3$ while it has a significant stabilizing effect on $Cs_{0.12}FA_{0.88}PbI_3$. However, 4,6,10-trihydroxy-3,5,7-trimethyl-1,4,6,10-tetraazaadamantane hydrochloride strongly enhances the stability of both Pb-halide perovskites as evident in its effective prevention of Pb^0 formation, prevention of light induced recrystallization as well as the reduction of photolysis and thermolysis reaction rates responsible for the production of PbI_2.[211] Nanoscale infrared scattering-type scanning near-field optical microscopy (IR s-SNOM) imaging reveals the difference in the stabilizing effects of both additives to be the difference in their localization within the perovskite films. In particular, 4,6,10-trihydroxy-3,5,7-trimethyl-1,4,6,10-tetraazaadamantane hydrochloride localizes at the grain boundaries, enabling effective healing of defects and suppression of degradation reactions while 1,3,5,7-tetra-azaadamantane integrates into the perovskite grains, leaving MA^+, in the form of MAI, on the grain boundaries.

DFT calculations confirm the greater effectiveness of the 4,6,10-trihydroxy-3,5,7-trimethyl-1,4,6,10-tetraazaadamantane hydrochloride to stem from a superior affinity towards undercoordinated Pb atoms on the perovskite surface, preventing the leakage of PbI_2. It can also dissociate on the perovskite surface, releasing Cl^- anion, which further stabilizes the film due to increased workfunction (WF) and suppressed triiodide (I_3^-) formation. However, 1,3,5,7-tetraazaadamantane does not undergo such dissociation as the bonding between its cation and I^- counterion is stronger on the perovskite surface than in the gas phase, a reason for its lower effectiveness as a perovskite phase stabilizer. Moreover, the optimal effects of the additives on the $Cs_{0.10}MA_{0.15}FA_{0.75}PbI_3$ and $Cs_{0.12}FA_{0.88}PbI_3$ perovskite films significantly enhance their photochemical and thermal stability. The coordination of such additives with perovskite components controls the crystallization and manages the phase segregation of mixed-cation perovskite films.

As shown in Fig. 8(f), at an optimal ratio (0.5 mg ml^{-1}), N-acetyl-L-phenylalanine achieves high crystallinity in the films. This is as a result of slowing down the crystallization process through a slow and complete reaction between the organic cations and the Pb–I framework and the formation of strong H bonds between –NH and I.[212] As shown in Fig. 8(g), the better crystallinity is also seen up to the bottom of the perovskite layer as exhibited in the strong perovskite peak intensity and a decrease in PbI_2 peak intensity, demonstrating an overall uniformity of the perovskite film. Notably, the toxicity of Pb raises environmental and health concerns and reagents such as DMF and DMSO have been used as leaching reagents to recover

32994 | J. Mater. Chem. A, 2025, 13, 32964–33011

This journal is © The Royal Society of Chemistry 2025

Pb.[213,214] The toxicity of these organic solvents has also led to their replacement with ultrasonic water leaching which can effectively recover Pb from the glass substrates of discarded PSCs.[215] With the ultrasonic water leaching, the perovskite layer undergoes rapid degradation, generating PbI_2 which wholly goes into the water or as Pb(OH)I without ionizing into the toxic Pb^{2+}. The Pb removal is highly efficient and pure PbI_2 crystals can be recovered from the water medium by evaporation. However, since Pb is crucial to the photophysics of the perovskite thin film and the device performance, it is preferable to retain it and prevent the Pb leakage-induced phase segregation. This can be achieved by the addition of the di-azapolyoxamacrobicycle structure of cryptand 222 into the perovskite lattice.[216] It prevents Pb leakage by effectively coordinating with Pb^{2+} and forming H bonds with FA^+ of the perovskite. It effectively chelates and firmly anchors Pb^{2+} through host–guest complexation. The interaction also reduces defect density and non-radiative recombination.

The numerous methods to stabilize MCPs and PSCs through additive engineering can be unified to achieve a universal approach irrespective of the perovskite absorber layer type. Comparing a standard triple cation perovskite with bandgap *ca.* 1.58 eV and a wider bandgap (*ca.* 1.63 eV) perovskite processed by a combination of additives, *i.e.*, 1-butyl-3-methylimidazolium tetrafluoroborate, oleylamine and benzylhydrazine hydrochloride shows that such additive combination leads to desirable improvements in the efficiency and stability of corresponding single junction and tandem devices of both types of MCP under standard and low light testing and operating conditions.[217]

Evidently, the phase stability of MCPs is crucial to their material quality and device applications. Although extensive efforts and significant progress have been made in the mitigation of the effects of stressors on the structural, morphological, photophysical and device-related properties of this class of compounds, many reports are based on controlled laboratory conditions. Therefore, a large room still exists for the advancement of MCPs towards achieving effective competition with other matured PV technologies. In particular, more attention must be given to developing MCPs capable of stable operational behavior under real-life conditions where there is little or no control of environmental factors affecting their phase stability. Finetuning reported experimental methods through cutting-edge computational methods can unlock unique features in the materials. Such reported methods are morphology manipulation, additive treatments, strain management, rational composition tailoring and advanced device encapsulation.

7 Photophysical property enhancement

Device design and material structural properties are profoundly related to the photophysical properties of the perovskite absorber layer.[83,84,218,219] This relationship controls the stability of the absorber layer in contact with other functional layers in the device as well as the charge generation and separation

dynamics in the perovskite bulk and the quality of charge extraction at the CTL/perovskite interface. Multi-cation perovskites consisting of Cs^+, MA^+ and FA^+ are of high interest today due to their ability to yield high PCE in solar cells.[15,78–80,186] The generation of multiple excitons (*i.e.*, electron–hole pairs) from a single high-energy photon can enhance the PCE in corresponding PV devices. However, low efficiency, high photon-energy threshold and fast Auger recombination in the halide perovskite limit its feasibility. Incidentally, multiple exciton generation can be enhanced by a partial substitution of Pb by Sn in the perovskite structure which ensures a slower cooling and reduced trapping of hot carriers as revealed by transient absorption measurements, DFT calculations and nanoscale molecular dynamics simulations.[220] This can increase the efficiency and lower the photon-energy threshold of the perovskite such as $FAPb_{1-x}Sn_xI_3$ ($x \leq 0.11$).

Ultraviolet-light illumination also facilitates an increase in internal photocurrent quantum efficiency and a low photon-energy threshold driven by multiple exciton generation. To achieve the full potential of the PSC, it is important to investigate the chemical and optoelectronic properties of the perovskite absorber layers and their interfaces with adjacent layers. Using depth-profiling photoemission spectroscopy it is possible to study these properties at different thicknesses and depths from the film surface to its bulk through etching using ionic argon beam.[60] The dependence of a material's photophysical stability on its chemical properties can be ascertained through Ar^+ sputtering thinning of the surface chemical composition. The triple-cation mixed-halide perovskite can be fabricated into a half cell, *i.e.*, glass/FTO/c-TiO_2/perovskite and subjected to the surface etching process. The half-cell can be subsequently evaluated by XPS to obtain the percentage atomic ratios as the etching time (depth of etched area) increases as shown in Fig. 9(a). The PL spectra at selected thicknesses after etching shown in Fig. 9(b) reveal a decrease in intensity as the layer is being progressively etched out. The negligible variation in the peak shapes suggests phase stability irrespective of the layer thickness. Both the XPS and PL results reveal homogeneous and reproducible elemental distribution up to depths close to the TiO_2/perovskite interface. Moreover, the drop in PL peak intensity can be attributed to the reduction in film thickness with progressive etching through Ar^+ sputtering. The perovskite layer exhibits high quasi Fermi level splitting values and largely homogeneous optoelectronic properties (*i.e.*, bandgap) at different thicknesses as shown in Fig. 9(c), suggesting a low surface recombination rate, even after Ar^+ sputtering. This is also confirmed by the negligible changes observed in the normalized PL decay shown in Fig. 9(d). To validate the compositional–structural–photophysical relationship, it is important to employ techniques which do not cause any drastic chemical and optoelectronic modifications in the perovskite materials and are reliable at determining the in-depth composition of the perovskite layer.

Although MCPs have shown fascinating photophysics, retaining such properties at low frequency is still debatable. A better understanding can be obtained by clearly distinguishing the contribution of ionic, molecular and electronic polarization
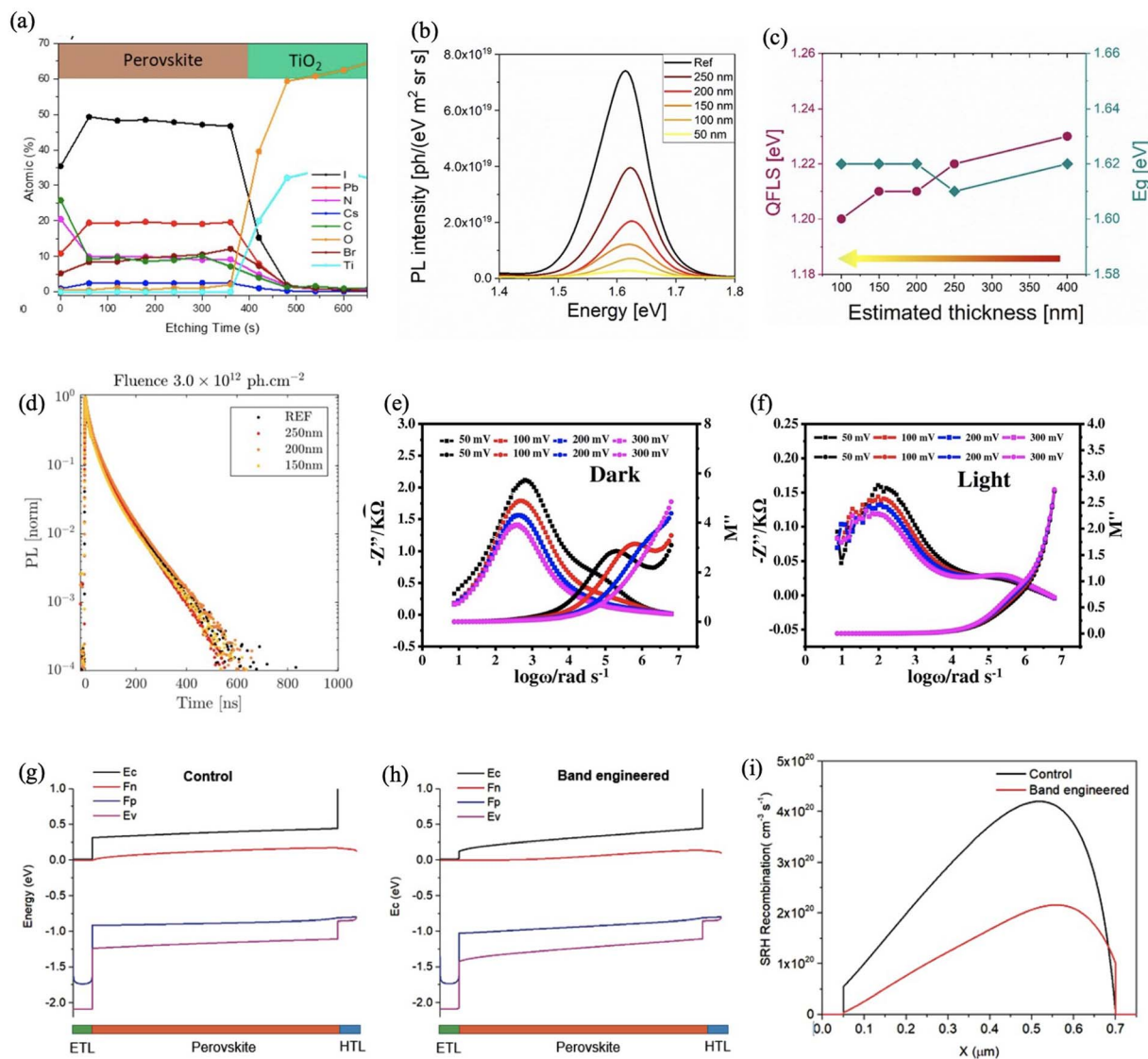
This journal is © The Royal Society of Chemistry 2025

J. Mater. Chem. A, 2025, **13**, 32964–33011 | **32995**

Fig. 9 (a) XPS depth profile showing the depth-dependent atomic ratio of etched perovskite/TiO$_2$ derived from Ar$^+$ sputtering. The atomic ratio was extracted from XPS peak fitting in the Br 3d, Cs 3d, I 3d, C 1s, N 1s, Pb 4f, O 1s, and Ti 2p regions. (b) Average PL spectra of selected post-etching thicknesses. (c) Quasi-Fermi level splitting (QFLS) and bandgap changes as a function of post-etching thickness of the perovskite layer. (d) Time-resolved PL decays at a fluence of 3.0 × 10^{12} ph cm^{-2} of unetched and three selected post-etching thicknesses. Reproduced from ref. 60 with permission from American Chemical Society, copyright 2022. Imaginary impedance (Z'') and electrical modulus (M'') plots of operational PSCs (e) in the dark and (f) under illumination. Reproduced from ref. 221 with permission from Elsevier Ltd, copyright 2021. CBMs (Ec), VBMs (Ev) and electron and hole quasi-Fermi levels (Fn and Fp) for (g) control and (h) band engineered PSCs based on SCAPS-1D simulation results. (i) Shockley−Read−Hall recombination rates of the control and band engineered PSCs. Reproduced from ref. 8 with permission from Wiley-VCH GmbH, copyright 2021.

to their charge carrier kinetics, electrical modulus and conductivity in a device through the study of the impedance response and polarization phenomenon.[221] The low-frequency carrier kinetics of the widely studied Cs$_{0.06}$FA$_{0.79}$MA$_{0.15}$-Pb(I$_{0.85}$Br$_{0.15}$)$_3$ triple cation PSCs using bias-dependent impedance and modulus spectroscopy in the dark and under illumination conditions revealed a strong dependence of dielectric permittivity on frequency within the 1 Hz and 1 MHz range with a dielectric relaxation that follows the Maxwell–Wagner type interfacial polarization attributed to grain boundary and ionic defects. A correlation of the impedance and

modulus spectra reveals the localized charge carrier relaxation, indicating a charge and ionic hopping process in the device. It shows that the impedance, dielectric relaxation and electrical modulus phenomenon involving the response of charge carriers in triple cation PSCs are dependent on the bias and frequency applied. The imaginary impedance (Z'') peak positions are mainly shifted to a lower frequency compared to the electrical modulus (M'') peak positions in the dark (Fig. 9(e)) and under light (Fig. 9(f)) conditions. It confirms short-range hopping of charge carriers, localized relaxation and deviation from ideal Debye-like behavior in the PSC.[222,223] From the Z'' peak shifts, it

32996 | J. Mater. Chem. A, 2025, 13, 32964–33011

This journal is © The Royal Society of Chemistry 2025

can be seen that the relaxation time increases with bias and under illumination indicating that bias and illumination play an important role in the electronic and ionic characteristics of perovskites.[224,225] Evidently, various competing sources of polarization in the device under illumination influence the overall conductivity of the device as well as the PCE.

MA$^+$ contributes significantly to the fascinating photophysics of this class of materials. It is also the least kinetically stable component, limiting their thermal stability. Therefore, structural plasticity such as that seen in 2D structures which allows the modifications of the optoelectronic parameters by tailoring the chemistry of the organic cations can enhance the structural integrity of the perovskite lattice.[226] It allows effective control of excitonic absorption wavelength, exciton binding energy value and phase transitions. Nevertheless, MA-free multi-cation perovskite configurations have also received significant attention. This class of compounds possesses lower carrier diffusion lengths leading to lower performance in PV devices.[227] To mitigate this drawback while maintaining thermal stability, band engineering strategies in CsFA perovskites have been pursued.[8] Combined theoretical and experimental studies have revealed that adding n-type dopants such as 4-(1,3-dimethyl-2,3-dihydro-1H-benzimidazol-2-yl)-N,N-diphenylaniline into the perovskite bulk through a gradient doping strategy favors band bending and alignment with adjacent layers. The simulation results of pure CsFA PSC (Fig. 9(g)) and modified CsFA PSC (Fig. 9(h)) show that the CBM of the perovskite layer can be bent more toward the lowest unoccupied molecular orbital (LUMO) or CBM of ETL through this method. It modifies the electric field and facilitates charge transfer and charge extraction. As shown in Fig. 9(i), it also reduces non-radiative recombination such as Shockley–Read–Hall (SRH) recombination by 50%, leading to an improved fill factor with stable PV parameters comparable to those of the flat band conditions in MA-containing mixed cation perovskites.

Notably, the FA$^+$ component contributes to the material photostability and the lack of it can limit the material application as can be seen in the moisture sensitive all inorganic CsPb$_2$I$_x$Br$_{3-x}$.[9] Structural and electronic properties can be enhanced in CsPb$_2$I$_x$Br$_{3-x}$ perovskite against moisture and heat by intercalating a chromium-based metal–organic framework group such as terpyridyl chromium with the Pb–I cavity to serve as the A-site cation. Consequently, the 3D structure of the material can be disrupted to form a structurally and electronically coupled perovskite material exhibiting delocalized electrons, multiple and interactive charge transport channels within the material. The enhanced stability and electronic properties can be attributed to high structural integrity, moisture resistance and facilitated charge transfer between the conjugated bonds of the metal organic framework and the [PbI$_6$]$^{4-}$ of the perovskite.

It is evident that perovskite materials possess remarkable photophysical properties as they exhibit efficient light absorption and charge transport. Measures discussed here have been taken to address the instability issues arising from their vulnerability to environmental factors such as moisture and heat so as to better harness their fascinating photophysical

properties. Moreover, amplifying the encapsulation processes of corresponding devices and establishing new methods to advance the photophysical properties of all-inorganic halide perovskites which already exhibit high stability compared to organic–inorganic hybrid perovskites such that they match or surpass those of the organic–inorganic hybrid perovskites will be a desired research direction.

8 Device engineering

Perovskite device engineering involves the structural and compositional optimization of PSCs towards performance and stability enhancement.[228–230] Specific strategies such as absorber layer engineering,[229] interface engineering[231] and device architecture design[232] can fine-tune the perovskite material's properties, improve charge transport, extraction and collection, reduce recombination and promote light absorption. For absorber layer engineering, measures such as rational chemical composition modification and compatible deposition techniques are prioritized.[233,234] Altering the perovskite's chemical composition at the A-, B- and X-sites and alloying/doping with suitable materials can tune its optoelectronic properties (e.g., carrier lifetime, bandgap and absorption edge) and improve its stability and performance. It can also prevent or suppress Pb leaching, mitigating the toxicity of Pb-based perovskites.[230]

The compositional inhomogeneity of MCP thin layers (e.g., (FAPbI$_3$)$_{0.85}$(MAPbBr$_3$)$_{0.15}$) contributes to their polycrystallinity. It catalyzes local lattice mismatches and residual strains. The imperfection may result from gradient thermal stress during the thin layer processing. Depth-dependent grazing incident X-ray diffraction measurements shown in Fig. 10(a) reveal a gradient distribution of the compositional inhomogeneity and the attendant in-plane strain in the perovskite film which are perpendicular to the substrate.[229] The test crystal plane corresponding to the diffraction vector N_k was fixed and the instrument tilt angle ψ corresponding to the sample normal direction was varied. It can be seen that the (001) lattice distance increases with ψ. Fig. 10(b) shows the residual strain distributions at the depths of 50, 200 and 500 nm and the slopes reveal that the largest strain is located at the film surface region. First-principles calculations show the impact of such strain on carrier dynamics in corresponding solar cells to be due to strain-induced energy band bending in the perovskite absorber layer. The evolution of energy levels under tensile strains is shown Fig. 10(c) (left panel). The downshift in the perovskite absorber layer CBM is less intense with increasing strain magnitude than it is for the VBM. It reveals a greater impact of the tensile strain at the perovskite/HTM interface as shown in the higher bending of the VBM than the CBM in Fig. 10(c) (right panel) which also creates deeper defect levels in the perovskite films. The band bending results in energy level mismatch with the contact. Incidentally, rational temperature gradient inversion by film flipping during perovskite film fabrication can mitigate the strain and its gradient over the perovskite film thickness. This leads to flattened CBM and VBM, strain reduction, enhanced carrier mobility, increased interfacial charge transport and extraction in the corresponding device.
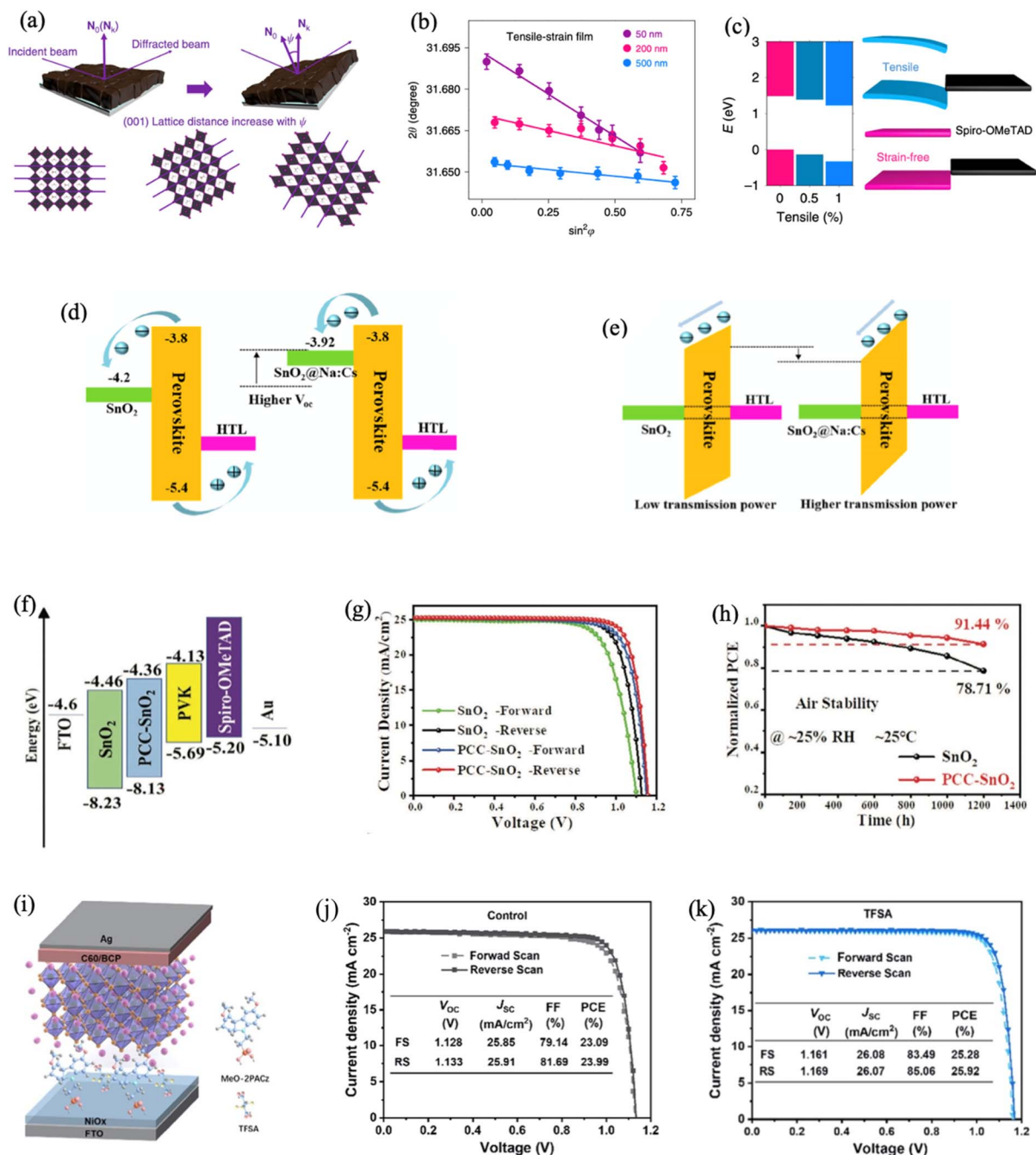
This journal is © The Royal Society of Chemistry 2025

J. Mater. Chem. A, 2025, 13, 32964–33011 | 32997

Fig. 10 (a) Gradient lattice structure characterization. Schematic illustration of the measurement of residual strain distribution in $(FAPbI_3)_{0.85}(MAPbBr_3)_{0.15}$ perovskite film. (b) Gradient strain distribution at depths of 50, 200 and 500 nm for the strained $(FAPbI_3)_{0.85}(MAPbBr_3)_{0.15}$ film. (c) Changes in CBM and VBM with increasing tensile strains in the perovskite films (left panel) and the schematic comparison of energy level alignments of the strained and strain-free films with HTL in a solar cell (right panel). Reproduced from ref. 229 with permission from Springer Nature Limited, copyright 2025. Schematic diagram of the carrier transport dynamics showing (d) WF shift of the SnO_2 ETL which yields increases in the built-in potential and V_{oc}, (e) reduction in the transport barrier of the carrier and series resistance due to the increased built-in potential. Reproduced from ref. 237 with permission from Elsevier Inc., copyright 2022. (f) The energy level diagram of the PSCs showing the lifting of the CBM of the phosphorylcholine chloride doped SnO_2 (PCC-SnO_2) ETL. (g) J–V curves obtained from reverse and forward scanning for both pristine and phosphorylcholine chloride doped SnO_2 ETL. (h) Stability test of unencapsulated devices based on both pristine and phosphorylcholine chloride doped SnO_2 ETL in air under ca. 25% RH at 25 °C. Reproduced from ref. 231 with permission from Wiley-VCH GmbH, copyright 2024. (i) Schematic diagram of the device showing tetrafluorosuccinic acid (depicted as TFSA) as the buried interfacial regulator in the presence of MeO-2PACz self-assembled molecules. (j) Forward and reverse scan J–V curves and PV parameters of the control device without tetrafluorosuccinic acid. (k) Forward and reverse scan J–V curves and photovoltaic parameters of the champion device with tetrafluorosuccinic acid. Reproduced from ref. 186 with permission from The Royal Society of Chemistry, copyright 2024.

32998 | J. Mater. Chem. A, 2025, 13, 32964–33011

This journal is © The Royal Society of Chemistry 2025

Furthermore, thin layer deposition techniques most compatible with a given perovskite type must be used to achieve controlled morphology and grain size. For example, MCP thin film deposition can be scalable, easily controlled and reproducible through a hybrid evaporation–solution method. For example, the PbI$_2$/CsBr layer can be deposited by co-evaporation and organic-halide, *i.e.*, FA- and MA-halide, solutions in a green solvent can be spin coated on it to form the film.[234] The bandgaps can be tuned between 1.55 and 1.67 eV by varying the CsBr and MABr ratios. Notably, films deposited can achieve high thermal and moisture stability, long carrier lifetime and small spectral shift with light exposure. The improved properties stem from the less residual PbI$_2$ and controlled MA$^+$ incorporation. Tuning the co-evaporation rates of CsBr and PbI$_2$ and increasing the concentrations of FAI/FABr solutions, He *et al.* demonstrated grain growth, effective bandgap optimization and defect suppression in the Cs$_x$FA$_{1-x}$PbI$_{3-y}$Br$_y$ perovskite series *via* a two-step preparation process.[228] The strategy follows a sequential thermal evaporation/spin-coating process which regulates the mismatch between sub-cells in a perovskite/Si tandem structure, decreasing voltage loss. In particular, the perovskite absorber layer composition was tuned by simultaneously evaporating CsBr and PbI$_2$ precursors at varied rates as well as varying the concentration of FAI/FABr solutions deposited by spin-coating. Varying the evaporation rate also regulates the PbI$_2$ ratio and prevents the formation of excess PbI$_2$ which may cause high series resistance. It reveals the correlations between composition and device performance including current matching in a perovskite/Si tandem structure.

Moreover, as demonstrated by Du *et al.*, the application of the perovskite absorber layer prepared by a two-step sequential deposition method in an inverted device structure yields efficiencies which significantly lag behind those of the one-step deposited films.[233] Factors such as interface imperfections and quality of PbI$_2$ film deposited in the first step mainly plague the two-step method. Incidentally, introducing RbCl and choline chloride into PbI$_2$ effectively improves the structural intercalation of both components in the second step, yielding a high quality perovskite layer exhibiting excellent energy level matching with adjacent layers. To achieve this, the –OH group of choline chloride binds with Pb^{2+} in the PbI$_2$ film and expands its [001] crystal plane. The –OH group also forms H bonds with N in FA$^+$ and MA$^+$, passivating grain boundaries and surface defects. Furthermore, the positively charged ammonium group in choline chloride passivates negatively charged defects in the perovskite films. RbCl combines with PbI$_2$, stabilizing the perovskite α-phase. These interactions slow down the perovskite crystallization, improving the film crystal quality. Simultaneous incorporation of the choline zwitterions into the SnO$_2$ ETL and the CsPbI$_2$Br absorber layer can also passivate trap defects.[235] Hence, interface engineering is achieved through passivation techniques which minimize perovskite/CTL interface defects and strains.

Numerical studies have shown that HTL makes a more profound contribution to the PSCs' degradation, especially at elevated temperatures, and the use of metal oxide/polymer (*i.e.*, NiO$_2$/PTAA) bilayer HTL was demonstrated to improve the

device performance.[48] Another strategy is the complete exclusion of HTL to achieve HTL-free PSCs.[236] However, the presence of ETL is crucial to the performance of PSCs. Therefore, enhancing the ETL and ETL/perovskite interface quality can further advance the device performance. This has been achieved by doping Na$^+$ and Cs$^+$ into SnO$_2$ ETL.[237] The Na$^+$ and Cs$^+$ improve the electron cloud density and electrochemical properties of the ETL. The improvement leads to suitable energy level alignment, enhanced transmission rate, electrical conductivity, electron mobility and surface morphology. This is achieved as shown in Fig. 10(d) due to the shift in WF of the SnO$_2$ ETL which results in an increase in built-in potential and V_{oc} in the device. As shown in Fig. 10(e), the doping further reduces the series resistance of the device, increasing charge transmission. Ammonium citrate modified SnO$_2$ ETL plays a similar role as its NH$_4^+$ forms nucleation sites which facilitate the growth of high-quality perovskite film on its surface.[159] The lone-pair of electrons on the C=O and N–H functional groups of the ammonium citrate passivates oxygen vacancy defects on the SnO$_2$ and perovskite film surfaces, significantly reducing hysteresis. As shown in Fig. 10(f), phosphorylcholine chloride enhances the electrical properties of the SnO$_2$ and ensures better energy level alignment with the perovskite layer by lifting its CBM which leads to improvements in the conductivity and electron mobility, carrier extraction and transport of SnO$_2$ as well as improved *J–V* characteristics with reduced hysteresis and better PCE retention after 1200 h as shown in Fig. 10(g and h).[231]

Notably, the suppression of interfacial stress which favors better crystallization and interfacial defect passivation can further improve these device properties. Passivating the grain boundaries of mixed FAPbI$_3$ and MAPbBr$_3$ with GA from GAI gives a smoother and more uniform grain distribution, improved crystallinity and better carrier transport.[238] The GAI is made of electron-rich and electron-poor components. DFT calculations of the GAI passivation mechanism based on different simulated perovskite surfaces such as an A-site cation vacancy defect surface, a Pb-deficient surface and an iodine-deficient surface show that GAI can effectively passivate all the surface dangling bonds and defects irrespective of their chemical and electronic properties. The ammonium group's unsaturated N atoms and I$^-$ ions in GAI synergistically repair the surface defects and suppress the trap assisted non-radiative recombination. The resulting SnO$_2$ ETL releases the residual stress of the perovskite layer.

Furthermore, self-assembled monolayers or polymers have been used as passivating agents while dipole molecules have been used to optimize the energy level alignment between the perovskite and CTLs.[179,180,182,184,186] This has been assisted by a careful selection of suitable CTLs exhibiting matching energy levels, high conductivity and good stability. In particular, the combination of self-assembled monolayers with fluorine-substituted succinic acid derivatives can achieve optimal interfacial contact and band alignment at the ETL/perovskite interface. Chen *et al.* demonstrated that tetrafluorosuccinic acid can optimize the alignment and surface contact potential of MeO-2PACz as shown in Fig. 10(i).[186] This reduces the interfacial charge transport barriers and non-radiative recombination in

This journal is © The Royal Society of Chemistry 2025

J. Mater. Chem. A, 2025, **13**, 32964–33011 | **32999**

the perovskite films. The symmetrical molecular structure of the tetrafluorosuccinic acid and strong electronegativity of its multiple active sites (*i.e.*, –COO and F) stabilize FA$^+$ *via* multi-site H bonding between FA$^+$ and F$^-$ and passivate under-coordinated Pb^{2+} defects, preventing the formation of I$^-$ vacancy defects. Comparing devices without and with tetrafluorosuccinic acid treatment, the PCE of the tetrafluorosuccinic acid treated device moves from 23.99% to 25.92% with both devices exhibiting negligible hysteresis (Fig. 10(j and k)). Although such self-assembled monolayers can form highly efficient hole-selective contacts in a transparent conductive oxide (TCO)/SAM/perovskite stack, they introduce

poor structural and performance stability into the stack.[186,239–241] Replacing them with dyes such as N719 to achieve an ITO/N719/perovskite stack can mitigate this drawback.[241] This has been demonstrated to enhance charge transport, passivate interfacial defects and act as an adhesive layer capable of preserving the structural integrity of the stack in a solar cell device based on the Cs$_{0.10}$FA$_{0.90}$PbI$_3$ perovskite absorber layer. The effectiveness of the ITO/N719/perovskite stack is attributed to its low interfacial trap density, capacity to increase ITO WF through the creation of interfacial dipole moment, UV resilience as well as strong adhesion and passivation capability as its carboxylate group strongly binds to the Pb^{2+} and FA$^+$/Cs$^+$ of the perovskite.
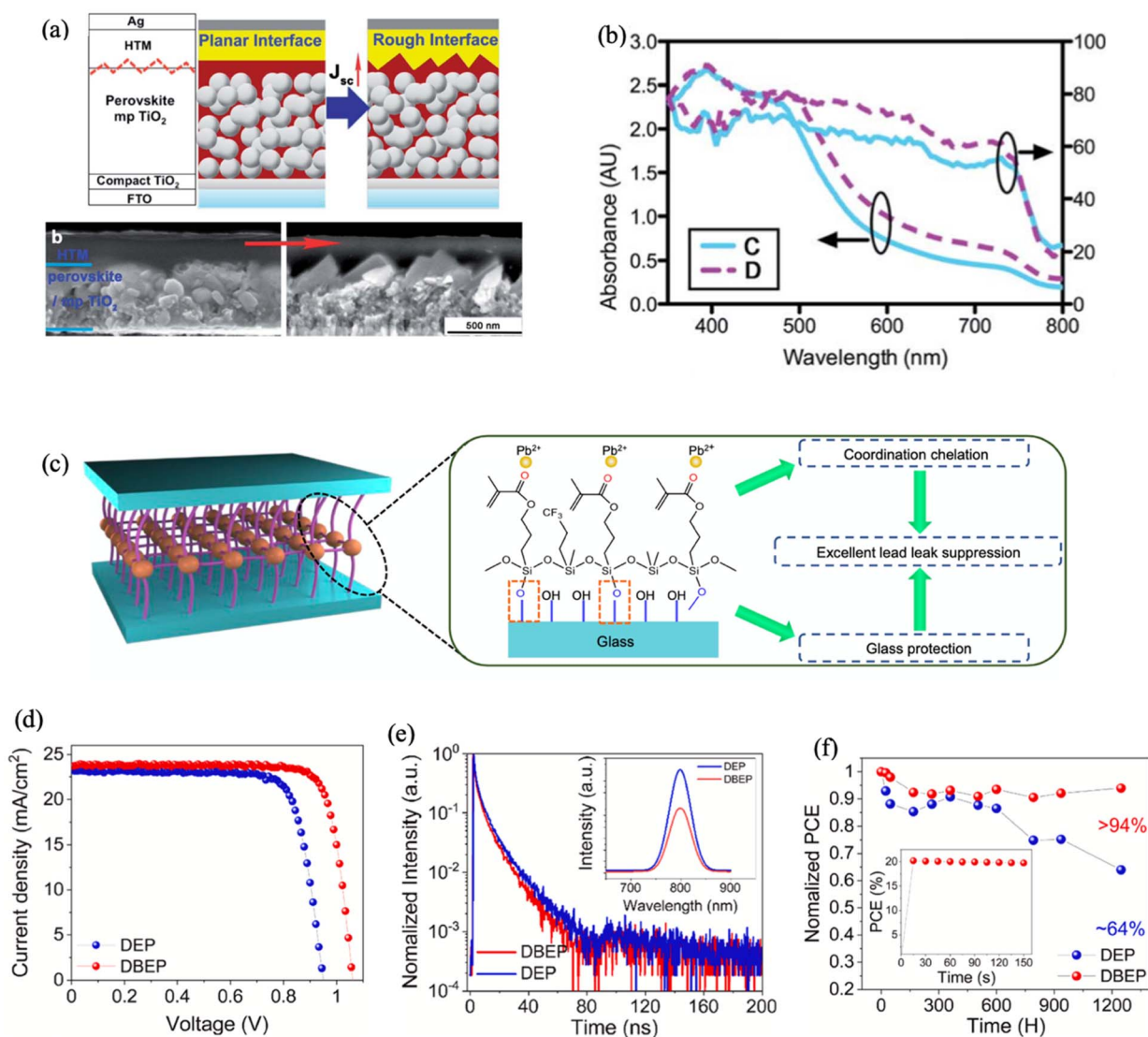

Fig. 11 (a) Schematic illustration of the transition of CH$_3$NH$_3$PbI$_{3-x}$Cl$_x$ perovskite surface and its interface with HTL from planar to rough in an n–i–p device structure. Below are the corresponding cross-sectional SEM images. (b) The absorption spectra and IPCE of the CH$_3$NH$_3$PbI$_{3-x}$Cl$_x$ device based on the smooth (C) and rough (D) interfaces showing enhanced performance for the latter. Reproduced from ref. 232 with permission from The Royal Society of Chemistry, copyright 2014. (c) Schematic illustration of Pb leakage suppression through effective glass protection and coordination bonding between C=O groups of the encapsulant and Pb^{2+} of the perovskite. Reproduced from ref. 230 with permission from Springer Nature Limited, copyright 2025. (d) J−V curves of best performing PSCs and (e) TRPL patterns (inset is the PL) of the devices, fabricated using double antisolvent denoted as DBEP and single antisolvent denoted as DEP. (f) Stability patterns of the unencapsulated PSCs under ambient conditions (40% RH, 25 °C). Inset shows the operational stability of the device based on DBEP under continuous 1 sun irradiation. Reproduced from ref. 255 with permission from Elsevier Ltd, copyright 2021.

33000 | *J. Mater. Chem. A*, 2025, **13**, 32964–33011

This journal is © The Royal Society of Chemistry 2025

Notably, N719 does not create parasitic optical absorption in the device.

Beyond the functional layers, device architecture, *e.g.*, planar and mesoporous heterojunctions, n–i–p and p–i–n structures can also determine light absorption, charge separation and overall device performance.[8,79,133,143,153,242] Various fabrication methods have been developed for PSCs. However, it is important for PSCs to make full use of incident light, improve the charge transport property and achieve high PCE without increasing the complexity of the devices such that they remain suitable for practical applications. As shown in Fig. 11(a), a continuously rough surface of densely arranged large perovskite crystallites can be obtained from a sequential deposition process at high processing temperature and short pre-wetting time.[232] Achieving a rough interface between the perovskite absorber layer and the contacts can enhance light scattering effect, improve light harvesting and charge transport as evident in the test samples obtained from smooth and rough $MAPbI_{3−x}Cl_x$ perovskite films denoted as C and D respectively in Fig. 11(b) with D showing higher absorption spectra and IPCE than C, over the wavelength range of 470–750 nm. This simultaneously enhances J_{sc} and PCE in the device. Full-wave simulation has shown the roles of PSC components in light absorption across the solar spectrum.[243] It reveals that the perovskite absorber layer absorbs mostly in the UV and visible regions. Hence, a closely spaced plasmonic silver (Ag) nanoparticle array was proposed to optically enhance perovskite absorption in the IR region. The plasmonics create hot spots which can enhance the localized light absorption in the perovskite active layers through light-flow-circulation and nonlinear absorption mechanisms.

Finetuning the thickness and morphology of the functional layers improves light absorption and charge collection. PSCs are usually based on the perovskite absorber layer exhibiting film thickness of a few hundreds of nanometres.[8,92,133,188] A thicker film (in the micrometer scale) can address critical issues bordering on the commercialization, industrial compatibility, stability, scalability and reliability of the technology. However, thicker films yield lower device efficiencies.[244] This has been attributed to the defect-induced short carrier lifetime. Hence, fabricating perovskite devices with significantly long carrier lifetime can mitigate the limitation of carrier lifetime on device performance.[244,245] This can be achieved by regulating the lattice strain and charge carrier concentration in thick films. Although SCAPS-1D based on thickness dependent *J–V* characteristics and complex impedance data reveals that ionic diffusion and recombination processes behave differently with increasing absorber layer thickness, it predicts an optimal thickness of 700 nm for maximum efficiency in PSCs.[246]

Device efficiency has also been advanced through the development of new device architecture, such as tandem or multi-junction cells.[38,247] It is known that wide-bandgap perovskite top cells coupled with Si bottom cells in a tandem configuration can yield efficiencies >28%.[137,248] SCAPS 1D shows that the tandem solar cell performance can be enhanced by film thickness and doping concentration optimization. In these structures, mixed halide perovskites with wide bandgaps are commonly used as the top cell with the bottom Si cell.[37,38,137,247–249] In particular, the Br-rich inorganic perovskite $CsPbIBr_2$ is prominent in the application[247,249] and its V_{oc} (<1.3 V), usually lower than the requirement for a top cell, can be increased by multi-source cation/anion co-doping which concurrently incorporates different ratios of Rb^+ and acetate (Ac) ions.[249] The resulting device can yield a V_{oc} of 1.37 V. The multi-source cation/anion ($Rb^+/Ac^−$) doping strategy improves film quality, it also increases the WF of the $CsPbIBr_2$ film thereby reducing V_{oc} losses. The realized improvement in thermal stability can significantly enhance the PCE of the corresponding PSC unlike that of the PSC obtained *via* single-source Rb/Ac doping. The effectiveness of Rb^+ and acetate as dopants is also evident through numerical analysis.[250] As demonstrated for $CsPbI_{1.5}Br_{1.5}$ perovskite non-radiative recombination, optical losses and energy level mismatch can be mitigated through the formation of a surface multi-cationic heterojunction.[251] A precise control of the ratios of Rb^+, FA^+ and MA^+ on the perovskite film as well as the annealing time can form high-quality heterojunction layers which can effectively passivate surface defects. Lattice distortion in the resulting mixed cation perovskites can suppress light-induced phase segregation as it ensures increase in ion-migration E_a. This enhances their function as a top cell in a multi-junction solar cell.[206]

Furthermore, post-fabrication techniques such as encapsulation can protect the devices from degradation triggers such as moisture, oxygen, light, temperature, *etc.*, and prevent Pb leakage.[147,230] The complexity, poor thermal management and inefficient lead leakage suppression associated with many encapsulation processes can be mitigated by using a self-crosslinked fluorosilicone polymer gel (*e.g.*, fluoropropyl methylsiloxane-dimethylsiloxane multiblock polymer) to achieve nondestructive encapsulation at room temperature.[230] It exhibits excellent adhesion, transparency, thermal and UV stability, water and oxygen ingression prevention properties. Its nondestructive characteristic is evident in the similarities between the PCEs of freshly fabricated encapsulated and unencapsulated devices. By doping boron nitride (BN) into the encapsulant, the strategy promotes heat dissipation, preventing the adverse effects of heat accumulation. This is evident in the finite element simulation analysis of its heat dissipation ability compared to that of the UV resin encapsulant. The UV resin encapsulated device exhibits higher temperature than the device encapsulated with the BN doped self-crosslinked fluorosilicone polymer gel, indicating better thermal management in the later. The BN doped encapsulant also significantly inhibits Pb leakage based on damp heat and thermal cycling tests in a CsMAFA perovskite-based device. As illustrated in Fig. 11(c), this can be attributed to the excellent glass protection and strong coordination interaction between the encapsulant's C=O groups and the perovskite's Pb^{2+}.

Similarly adopting an industrially compatible encapsulation process which involves the lamination of PSCs with a highly transparent and viscoelastic semi-solid/highly viscous liquid polyolefin adhesive (*e.g.*, homopolymer PIB) reduces thermo-mechanical stresses caused at the encapsulant/rear electrode

This journal is © The Royal Society of Chemistry 2025

J. Mater. Chem. A, 2025, **13**, 32964–33011 | **33001**

interface by encapsulation processes and temperature gradients during accelerated ageing. Although PIB is often reported as an encapsulant for PSCs, typical PIB-based encapsulants contain several additives which impact their properties.[252,253] A low-molecular weight homopolymer PIB matrix deposited on glass substrates and modified with 2D hexagonal BN (h-BN) (nano) flakes to achieve PIB:h-BN encapsulants was demonstrated by Mariani *et al.* to retain >80% of initial PCE after accelerated testing in $Cs_{0.08}FA_{0.80}MA_{0.12}Pb(I_{0.88}Br_{0.12})_3$ PSCs.[254] It is a solvent- and strain-free encapsulation process which does not require the use of edge sealants and is compatible with different device structures as well as testing conditions.

Beyond encapsulation, inherently stable perovskite absorber layers can also be used in device fabrication. The inherent stability of MCPs can be enhanced by exploiting the complementary properties of dibutyl ether and diethyl ether anti-solvents in a one-step mixed antisolvent washing process.[255] Dibutyl ether possesses low vapor pressure while diethyl ether exhibits low boiling point. Both antisolvents can prevent moisture ingression and ensure complete reaction during film formation. This allows the fabrication of PSCs based on $(FAPbI_3)_{0.95}(MAPbBr_3)_{0.05}$ and $Cs_{0.01}FA_{0.94}MA_{0.05}PbI_{2.85}Br_{0.15}$ absorber layers under ambient conditions (RH >40%). It prevents moisture-induced lattice expansion of the FA-based perovskites and the attendant tensile stress which may be caused by using a single antisolvent. Comparing devices fabricated based on single and double antisolvent treatments denoted as DEP and DBEP respectively in Fig. 11(d–f), the strategy achieves larger grain size and better uniformity in the DBEP treated absorber layer. The encapsulation-free devices also achieved improved *J–V* characteristic (Fig. 11(d)) and faster charge extraction (Fig. 11(e)) with DBEP treatment. In Fig. 11(f), higher stability (*i.e.*, retention of >90% of initial PCE after 1300 h ageing) can also be seen for the DBEP treated device.

Developing scalable, cost-effective and industrially viable fabrication processes for PSCs based on MCPs is crucial for their commercialization and further research is required in this area. The stability and performance of the device can be predicted through device modeling using software such as SCAPS to simulate and optimize device performance based on specific material properties and device parameters. Numerical modeling by Elmourabit *et al.* revealed that the device structure; $FTO/PCBM/Cs_{0.05}(MA_{0.17}FA_{0.83})_{0.95}Pb(I_{0.83}Br_{0.17})_3/MeO-2PACz/Au$ can achieve superior performance and durability.[256] Combining machine learning algorithms such as random forest, XGBoost and neural networks with SHAP tool correlating stability with perovskite composition, bandgap, thickness, test temperature and humidity also gives ranges of compositional ratios and perovskite thin film thicknesses suitable for realizing highly stable PSCs.[257] In particular, it predicted that the perovskite bandgap should be *ca.* 1.6 eV and the device should be tested between 20 °C and 30 °C at a relative humidity <20%. The machine learning method by Mammeri *et al.* predicts that a standard device with a structure such as TiO_2 + m-TiO_2/2D–3D perovskite active layer/LiTFSi + TBP:P_3HT/a second HTL/carbon can exhibit high stability by preparing the perovskite active layer from a mixed DMF/DMSO precursor solution followed by

chlorobenzene antisolvent treatment,[258] whereas functional layers such as BCP + PCBM, $MAPbI_{3-x}Cl_x$, NiO, DEA and Al improve stability in inverted cells. It confirms that device architecture and absorber layer preparation method can dictate the overall device performance.[79,102,133,160] These predictions can be validated experimentally and spectroscopic measurements such as PL and TRPL can be conducted to gain deeper understanding of the charge carrier dynamics and recombination processes towards further development. Overall, it is important to developing more durable perovskite materials and device architecture capable of withstanding long-term operation under real-world conditions while maintaining high performance.

9 Challenges in stability evaluation

Beyond the development of strategies for stability improvements, a critical challenge for the commercialization of PSCs is the establishment of a reliable and widely acceptable long-term stability evaluation protocol. This is commonly achieved indoor through accelerated ageing which involves the stressing of test samples under conditions harsher than the standard.[146,147,259–262] It provides a faster estimation of the standard lifetime of PSCs through acceleration factor evaluation. The acceleration factor is derived based on the assumption that the degradation mechanism under accelerated conditions is the same under standard conditions. In particular, the degradation behavior of PSCs under illumination, elevated temperature (*e.g.*, 85 °C) and humidity (*e.g.*, 85%) is used to predict their outdoor lifetime.[146,261] Comparative studies of the indoor and outdoor degradation behaviors of PSCs over several months have also been conducted.[263] It is evident that indoor conditions do not exactly reflect those of the outdoor where the PSCs are exposed to multiple stressors whose intensities can vary based on daily and seasonal changes in atmospheric parameters and can create complex degradation pathways. The dependence of PSC performance on such multiple factors must be clearly understood especially for applications as top cells in tandem devices (*e.g.*, perovskite on Si tandem solar cells) where continuously matching electrical outputs are critical. Hence, the widely used ISOS-L protocol[264,265] cannot be solely sufficient to predict device lifetime under real world conditions. A more extensive testing involving other protocols (*i.e.*, ISOS-D, ISOS-O, ISOS-L, ISOS-LT *etc.*) must be adopted. The commonly used lifetime indicators such as T80 and T50 (*i.e.*, time taken for PCE to drop to 80% and 50% of the original value) are also limited as they are dependent on atmospheric parameters and are only useful for comparative purposes under similar conditions.[260,263]

Furthermore, PCE as a performance marker also depends on the degradation stage.[260] At an early stage, fast PCE reduction can be observed under both day and night conditions. This is followed by the mid-stage which involves a rapid increase in PCE during the day (due to light soaking) which is kept stable through the night. At the late degradation stage, the light soaking has no favorable effect on PCE. Notably, the photo-induced degradation can be fully or partially reversed during the night time. The reversible processes are attributed to (i) the formation and elimination of nonradiative recombination

33002 | *J. Mater. Chem. A*, 2025, **13**, 32964–33011

This journal is © The Royal Society of Chemistry 2025

defects, (ii) forward and reverse ion migration, (iii) self-healing through bond recovery and from structural defects. Conversely, degradation can also be induced during the night (*i.e.*, dark condition) and can be reversed under optimal illumination conditions through light soaking induced trap filling. Although this trend can be observed in the same device type under outdoor and indoor light cycling, there is a difference in its intensity. For example, the light soaking achievable under 1 sun (standard outdoor condition) can be accelerated by high intensity light illumination indoor due to the flexible control of parameters as demonstrated by Ren *et al.*[262] The change in light irradiance dose changes the degradation behavior of PCSs. Therefore, it is important to ensure uniformity between outdoor and indoor parameters during light and dark cycles to enable the simulation of outdoor PSC ageing indoor. Similarly, the evident day/night (*i.e.*, light/dark) effects on the stability of PSCs raise the need for standardized stability testing under light cycling, variable irradiance and temperature.

Overall, the establishment of a reliable lifetime evaluation framework for PSCs under real-world outdoor conditions is crucial to achieving commercial standards. This requires that the stability testing follows stricter protocols involving multiple stressors. It is important as the stressors make different degrees of impact on different device structures in different seasons.[146,147,262] This is further confirmed by modelling outdoor ageing behavior using indoor temperature-dependent degradation parameters for various device architecture.[261] It includes the internal thermal changes within the device during operation. Another reason is the broad range of lifetimes ranging from days to years which have been reported for devices under outdoor conditions and have been attributed to differences in device structure and atmospheric conditions.[260,263,266] For example, Khenkin *et al.* demonstrated that season to season steady degradation is more evident in PSCs based on single cation perovskites than those based on double cation perovskites.[263] The report also shows that identical PSCs can show similar stabilities under different irradiance conditions. However, irradiation and temperature under certain conditions may prevent complete degradation reversal, causing accumulated degradation. The device structure plays a significant role in the degradation process as devices possessing TiO_2 nanoparticle ETL were shown by Farooq *et al.* to be more vulnerable to UV light-induced degradation than other devices possessing SnO_2, spin-coated compact TiO_2 and e-beam deposited TiO_2 ETLs.[267] Also as demonstrated by Jiang *et al.*, the incorporation of self-assembled monolayer-based HTLs leads to improvement in the temperature-dependent operational stability of PSCs by suppressing ion migration due to their ion-blocking properties.[252] The stability improved by 2.8 times at 50 °C and 85 °C with only 20% drop in PCE after 8200 h and 1000 h respectively. Similar stability improvement was achieved with a 2D Cs_2-PbI_2Cl_2 perovskite capping agent at the perovskite/HTL interface.[259] Moreover, the merits of these interfacial layers commonly studied indoor may not be replicable outdoor.

Furthermore, analytical modelling has been proposed to facilitate lifetime evaluation of PSCs as they can potentially predict performance degradation due to ageing.[261] Notably, to actualize reliable lifetime evaluation protocol outdoor, device encapsulation and maximum power point tracking (MPPT) must be done. Although the procedures are complex and time-consuming, they are important. Encapsulation protects the device against moisture and oxygen ingression. It also prevents the escape of volatile components. MPPT determines the most favorable atmospheric parameters for optimal device performance. It is important that the encapsulation is correctly done. For example, epoxy and ethylene–vinyl acetate encapsulants are known to be less effective due to lack of complete inertness to PSC components and possible delamination at elevated and changing temperatures.[146] Incidentally, low-temperature, glass to glass encapsulation using polyisobutylene has been investigated and proven to be an effective strategy.[146,147] It has achieved up to 200 days of stability in damp heat and thermal cycling tests with FA-based PSCs and this performance can be improved with higher PCE devices.[146] In particular, to achieve effective encapsulation, important steps which must be taken include use of a thin passivation layer, adhesive and inert encapsulant, edge sealants, transparent rigid outer casing, *e.g.*, glass for maximized optical absorption as well as better mechanical and thermal handling, advanced integrated lead leakage prevention measures suitable for different stressors which can be realized by incorporating suitable components such as cation exchange resins, metal organic frameworks and phosphate salts.

10 Summary and outlook

Both all-inorganic and hybrid MCPs are shown here to offer versatile avenues for advancement towards next-generation PV applications. Although they both possess great potentials in this regard, such potentials vary depending on compositional and property differences. For example, hybrid MCPs exhibit excellent semiconducting properties, high carrier mobility, tunable light absorption and long diffusion lengths while all-inorganic MCPs offer superior stability especially at higher temperatures and in humid environments leading to a more prolonged lifetime of devices. Notably, the multicomponent nature of both types of materials accords them flexible property tuning due to facile compositional modifications during fabrication. In particular the mixed halide X-site allows for the tuning of optical and electronic properties, broadening their applications beyond the single junction solar cell structures to the all-perovskite tandem structures. Moreover, hybrid MCPs exhibit a relatively easier synthesis protocol such as low temperature fabrication and better property tailoring due to their organic components which allow alkyl chain length adjustments. The organic cations can also exacerbate vulnerability to degradation, whereas all-inorganic MCPs offer better structural integrity.

Nevertheless, photo- and electrical bias-induced ion migration and phase segregation are still a challenge in both types of perovskites. This is due to the disorder and strain introduced by the multiple lattice site compositions. The realization of high-quality films with the desired composition and crystal structure is also more challenging in all-inorganic perovskites. Moreover, hybrid and all-inorganic MCPs exhibit a degree of

This journal is © The Royal Society of Chemistry 2025

J. Mater. Chem. A, 2025, **13**, 32964–33011 | **33003**

defect tolerance. However, certain defects acting as non-radiative recombination centers still impact their optoelectronic properties especially at high concentration. For example, the energetically favorable antisite defects can as well act as deep level defects in the band gap. Various strategies such as partial substitution of B-site Pb^{2+} with other divalent cations (*e.g.*, Sn^{2+}), careful control of halide composition, use of additives and interface optimization have been proposed to enhance defect tolerance and stability, reduce toxicity and stabilize intermediate phases. The addition of specific amounts of Cs^+ and Rb^+ cations can also promote a more uniform halide distribution in hybrid MCPs. Despite the differences, all-inorganic MCPs have shown high PCEs closing in on those of hybrid MCPs. However, further research is crucial to address the challenges associated with these complex materials. An example is the development of more advanced techniques to accurately characterize and understand the nature and impact of defects.

Notably, high throughput prediction and identification of MCPs exhibiting excellent thermodynamic stability against multiple stressors can be done through combined experimental and computational studies. The approach has shown that composition control based on a rational variation of constituent ratios can greatly suppress lattice disorder. Such a strategy improves a material's stability by increasing the E_a of ion migration. It has shown that limiting the ratio of weak links (*e.g.*, MA^+) in the lattice also enhances stability. Validating theoretical predictions with experimental processes can reveal the actual characteristics of MCPs. The predicted characteristics such as large clusters of highly oriented crystalline perovskite films, optimal absorption and energy level alignment can be actually proven and verified. This is seen, for example, with MA which is usually the weakest link of the MCP lattice as it can also be a crystallization enhancer if infused into the film from a viscous solution due to complex formation. It shows that, before any post-fabrication optimization of MCPs and corresponding device are considered, a careful consideration of constituent types, their ratios and the preparation protocol most appropriate for the realization of the desired products must be prioritized. To achieve this, a deep knowledge of the competitions between the constituents in terms of sensitivity to their chemical environment and preparation-related stressors must be pursued. It is also important that the synergistic experimental and theoretical approach be advanced beyond descriptors compatible with controlled environmental conditions to those capable of ensuring operational integrity under real-life conditions. This can facilitate the commercialization and market viability for the technology.

Many aspects of MCPs can be better understood through material engineering. These include the rapid and uncontrollable crystallization, compositional (*e.g.*, Sn) oxidation, grain boundaries and interface defects, directional orientation, *etc.* It is important to also understand how these factors affect wide area processing of MCPs towards scaling the technology. Therefore, new insights and knowledge are needed to translate the measures currently taken to a larger and industrially viable scale. This also extends to the reversible processes in MCPs.

Although photo-induced phase segregation can be reversed when the light is removed, the multiple compositions of the lattice sites must be optimally controlled to ensure phase stability. Strategies such as precursor material adjustment, solvent engineering and film growth optimization have been beneficial in this regard. However, it is important to further understand the mechanisms of the various degradation pathways so as to address the root causes. A reversible Pb^{2+}/Pb^0 and I^-/I^{3-} redox photochemistry mechanism has been proposed. However, this is limited by the loss of volatile I_2. Therefore, the best strategies to minimize compositional losses and maximize recovery of degraded MCPs back to fresh or near-fresh states must be explored. Real-life conditions with little or no control of environmental factors affecting phase stability should be considered to advance the usefulness of this class of materials. This can be done by gaining deeper insights into the inherent reversible characteristics of the materials and exploiting them accordingly.

The MCP absorber layer and corresponding device stability can also be monitored from changes in photophysical properties. The changes are influenced partly by contact with adjacent layers which determine the quality of interfacial charge extraction in the device. Therefore, the changes in chemical and optoelectronic properties of the MCP as well as their interfaces with adjacent layers can be correlated with indicators such as shifts in PL peak positions and surface recombination rates using techniques such as depth-profiling photoemission spectroscopy, XPS and PL spectroscopy. The absence of perturbation of the optical properties and phase segregation can indicate stability in the MCP. Moreover, methods to further stabilize the MCP system such that the fascinating photophysical properties can be prolonged must be amplified. Such methods include advanced encapsulation of corresponding devices, materials' compositional engineering and the enhancement of photophysical properties in all-inorganic perovskites which already possess high stability compared to hybrid perovskites.

There is no doubt that device architecture is a key determinant of the quality and performance of PSCs. It dictates the perovskite/CTL interface and energy level alignment as well as stability against stressors. However, the vast number of parameters (*e.g.*, composition, structure, fabrication methods, measurement conditions, *etc.*) to be considered makes it a challenge to establish a unified strategy for the enhancement of efficiency and stability in the MCP solar cells. Notably, organic HTL has been proposed as the most culpable layer limiting the operational stability of the devices, and recommendations to develop HTL-free solar cells or replace organic HTLs with inorganic HTLs (*i.e.*, metal oxides) have been made. Conversely, ETL is crucial to the performance of PSCs, and the enhancement of its quality (by doping) and the interface it forms with the perovskite layer (by additive engineering) can further advance the device performance. Nevertheless, simulations can simultaneously predict stability and high performance in the MCP solar cells through morphological and photophysical parameter optimization. They can also predict the best device structure and reveal the impact of device structure changes on charge-carrier dynamics and performance.

33004 | *J. Mater. Chem. A*, 2025, **13**, 32964–33011

This journal is © The Royal Society of Chemistry 2025

Hence, a synergistic experimental and computational approach which adequately processes the vast material and device parameters in correlation with degradation mitigation strategies creates the most effective pathway to achieving high efficiency and stability in MCP PVs.

Conflicts of interest

There are no conflicts of interest to declare.

Data availability

No primary research results, software or code have been included and no new data were generated or analysed as part of this review.

Acknowledgements

References

1 Y. Jiang, M. A. Green, R. Sheng and A. Ho-Baillie, *Sol. Energy Mater. Sol. Cell.*, 2015, **137**, 253.

2 J. Cao, X. Xiong and J. Zhou, *Cryst. Growth Des.*, 2024, **24**, 5294.

3 O. I. Kucheriv, D. A. Haleliuk, S. Shova and I. A. Gural'skiy, *Dalton Trans.*, 2025, **54**, 1618.

4 J. Yuan, D. Zhang, B. Deng, J. Du, W. C. H. Choy and J. Tian, *Adv. Funct. Mater.*, 2022, **32**, 2209070.

5 L. Yang, J. Shi, Y. Wu, X. Jin, T. Bie, C. Hu, W. Liang, Y. Gao, M. Xu and M. Shao, *ACS Appl. Energy Mater.*, 2022, **5**, 8930.

6 K. R. Hansen, C. E. McClure, D. Powell, H.-C. Hsieh, L. Flannery, K. Garden, E. J. Miller, D. J. King, S. Sainio, D. Nordlund, J. S. Colton and L. Whittaker-Brooks, *Adv. Opt. Mater.*, 2022, **10**, 2102698.

7 M. N. Tran, I. J. Cleveland, J. R. Geniesse and E. S. Aydil, *Mater. Horiz.*, 2022, **9**, 2191.

8 Z. Huang, M. Wei, A. H. Proppe, H. Chen, B. Chen, Y. Hou, Z. Ning and E. Sargent, *Adv. Funct. Mater.*, 2021, **31**, 2010572.

9 S. Yuan, Y. Xian, Y. Long, A. Cabot, W. Li and J. Fan, *Adv. Funct. Mater.*, 2021, **31**, 2106233.

10 X.-X. Gao, B. Ding, H. Kanda, Z. Fei, W. Luo, Y. Zhang, N. Shibayama, A. Züttel, F. F. Tirani, R. Scopelliti, S. Kinge, B. Zhang, Y. Feng, P. J. Dyson and M. K. Nazeeruddin, *Cell Rep. Phys. Sci.*, 2021, **2**, 100475.

11 L. Min, H. Sun, L. Guo, M. Wang, F. Cao, J. Zhong and L. Li, *Nat. Commun.*, 2024, **15**, 2066.

12 C. Bao, Z. Yuan, W. Niu, J. Yang, Z. Wang, T. Yu, J. Wang and F. Gao, *Nat. Electron.*, 2024, **7**, 375.

13 S. Zhou, V. Rehm, H. A. Afify, Y. Han, J. Korczak, A. Szczerbakow, T. Story, Z. Peng, A. These, A. Barabash, A. Osvet, C. J. Brabec, K. Götz, T. Unruh, F. Hilpert,

O. Brummel, J. Libuda and W. Heiss, *Adv. Funct. Mater.*, 2024, **34**, 2404700.

14 I. Fratelli, L. Basiricò, A. Ciavatti, L. Margotti, S. Cepić, M. Chiari and B. Fraboni, *Adv. Sci.*, 2024, **11**, 2401124.

15 https://www.nrel.gov/pv/cell-efficiency (accessed May 2025).

16 N. E. Kopteva, D. R. Yakovlev, E. Kirstein, E. A. Zhukov, D. Kudlacik, I. V. Kalitukha, V. F. Sapega, O. Hordiichuk, D. N. Dirin, M. V. Kovalenko, A. Baumann, J. Höcker, V. Dyakonov, S. A. Crooker and M. Bayer, *Small*, 2024, **20**, 2300935.

17 J.-C. Jhou, A. Gaurav, H.-T. Lin and C.-F. Lin, *ACS Appl. Energy Mater.*, 2023, **6**, 9434.

18 F. Sun, C. Zhang, D. Li, F. You, C. Liang and Y. Wang, *Phys. Status Solidi A*, 2025, 2400524.

19 E. Aydin, T. G. Allen, M. De Bastiani, A. Razzaq, L. Xu, E. Ugur, J. Liu and S. De Wolf, *Science*, 2024, **383**, 6679.

20 Q. A. Akkerman and L. Manna, *ACS Energy Lett.*, 2020, **5**, 604.

21 T. Wang, R. Li, H. Ardekani, L. Serrano-Luja, J. Wang, M. Ramezani, R. Wilmington, M. Chauhan, R. W. Epps, K. Darabi, B. Guo, D. Sun, M. Abolhasani, K. Gundogdu and A. Amassian, *Matter*, 2023, **6**, 2963.

22 S. R. Pering and P. J. Cameron, *Mater. Adv.*, 2022, **3**, 7918.

23 C. Otero-Martínez, M. Imran, N. J. Schrenker, J. Ye, K. Ji, A. Rao, S. D. Stranks, R. L. Z. Hoye, S. Bals, L. Manna, J. Pérez-Juste and L. Polavarapu, *Angew. Chem., Int. Ed.*, 2022, **61**, e202205617.

24 Y. Zhang, Z. Xing, B. Fan, Z. Ni, F. Wang, X. Hu and Y. Chen, *Angew. Chem.*, 2023, **135**, e202215799.

25 C. J. Bartel, C. Sutton, B. R. Goldsmith, R. Ouyang, C. B. Musgrave, L. M. Ghiringhelli and M. Scheffler, *Sci. Adv.*, 2019, **5**, 2.

26 M. P. Hautzinger, W. Mihalyi-Koch and S. Jin, *Chem. Mater.*, 2024, **36**, 10408.

27 A. Mishra, M. A. Hope, M. Grätzel and L. Emsley, *J. Am. Chem. Soc.*, 2023, **145**, 978.

28 J. Wang, H. Lu, X. Tian, R. Long and O. V. Prezhdo, *Nano Lett.*, 2025, **25**, 882.

29 X.-X. Ma and Z.-S. Li, *Comput. Mater. Sci.*, 2018, **150**, 411.

30 Z. Li, M. Yang, J.-S. Park, S.-H. Wei, J. J. Berry and K. Zhu, *Chem. Mater.*, 2016, **28**, 284.

31 J.-W. Lee, D.-J. Seol, A.-N. Cho and N.-G. Park, *Adv. Mater.*, 2014, **26**, 4991.

32 T. J. Jacobsson, J.-P. Correa-Baena, M. Pazoki, M. Saliba, K. Schenk, M. Grätzel and A. Hagfeldt, *Energy Environ. Sci.*, 2016, **9**, 1706.

33 P. Gratia, G. Grancini, J.-N. Audinot, X. Jeanbourquin, E. Mosconi, I. Zimmermann, D. Dowsett, Y. Lee, M. Grätzel, F. De Angelis, K. Sivula, T. Wirtz and M. K. Nazeeruddin, *J. Am. Chem. Soc.*, 2016, **138**, 15821.

34 S. Sun, A. Tiihonen, F. Oviedo, Z. Liu, J. Thapa, Y. Zhao, N. T. P. Hartono, A. Goyal, T. Heumueller, C. Batali, A. Encinas, J. J. Yoo, R. Li, Z. Ren, I. M. Peters, C. J. Brabec, M. G. Bawendi, V. Stevanovic, J. Fisher III and T. Buonassisi, *Matter*, 2021, **4**, 1305.

35 J. Laakso, M. Todorović, J. Li, G.-X. Zhang and P. Rinke, *Phys. Rev. Mater.*, 2022, **6**, 113801.

This journal is © The Royal Society of Chemistry 2025

J. Mater. Chem. A, 2025, **13**, 32964–33011 | **33005**

36 J. Schmidt, J. Shi, P. Borlido, L. Chen, S. Botti and M. A. L. Marques, *Chem. Mater.*, 2017, **29**, 5090.

37 G. Xing, C. Li, W. Gao, J. Yang, X. Zhao, J. Wang, X. Ran, L. Chao, H. Huang, Y. Zhou, Y. Chen, Z. Wu, C. Ran and W. Huang, *Adv. Mater.*, 2024, **36**, 2404185.

38 W. Shen, H. Fang, D. Pu, W. Zheng, X. Zhang, G. Li, L. Huang, S. Zhou, W. Chen, Y. Zhou, Z. Feng, J. Liang, J. Zhou, P. Qin, G. Fang and W. Ke, *Adv. Funct. Mater.*, 2024, **34**, 2410605.

39 W. Zhang, H. Liu, Y. Qu, J. Cui, W. Zhang, T. Shi and H.-L. Wang, *Adv. Mater.*, 2024, **36**, 2309193.

40 X. Cai, F. Liu, A. Yu, J. Qin, M. Hatamvand, I. Ahmed, J. Luo, Y. Zhang, H. Zhang and Y. Zhan, *Light: Sci. Appl.*, 2022, **11**, 234.

41 X. Liu, Z. Yang, C.-C. Chueh, A. Rajagopal, S. T. Williams, Y. Sun and A. K.-Y. Jen, *J. Mater. Chem. A*, 2016, **4**, 17939.

42 D. Chi, S. Huang, M. Zhang, S. Mu, Y. Zhao, Y. Chen and J. You, *Adv. Funct. Mater.*, 2018, **28**, 1804603.

43 Z. Zhu, N. Li, D. Zhao, L. Wang and A. K.-Y. Jen, *Adv. Energy Mater.*, 2019, **9**, 1802774.

44 R. Wang, H. Gao, R. Yu, H. Jia, Z. Ma, Z. He, Y. Zhang, J. Yang, L. Zhang and Z. Tan, *J. Phys. Chem. Lett.*, 2021, **12**, 11772.

45 J. Yang, P. Manganaris and A. Mannodi-Kanakkithodi, *Digital Discovery*, 2023, **2**, 856.

46 M. Ahmadi, M. Ziatdinov, Y. Zhou, E. A. Lass and S. V. Kalinin, *Joule*, 2021, **5**, 2797.

47 S. Jariwala, S. Burke, S. Dunfield, R. C. Shallcross, M. Taddei, J. Wang, G. E. Eperon, N. R. Armstrong, J. J. Berry and D. S. Ginger, *Chem. Mater.*, 2021, **33**, 5035.

48 A. E. Louks, R. Tirawat, M. Yang, S. N. Habisreutinger, S. P. Harvey, K. Schutt, K. Zhu, J. J. Berry and A. F. Palmstrom, *Sol. RRL*, 2023, **7**, 2300248.

49 Y. Zhao, J. Zhang, Z. Xu, S. Sun, S. Langner, N. T. P. Hartono, T. Heumueller, Y. Hou, J. Elia, N. Li, G. J. Matt, X. Du, W. Meng, A. Osvet, K. Zhang, T. Stubhan, Y. Feng, E. H. Sargent, T. Buonassisi and C. J. Brabec, *Nat. Commun.*, 2021, **12**, 2191.

50 R. Larciprete, A. Agresti, S. Pescetelli, H. Pazniak, A. Liedl, P. Lacovig, D. Lizzit, E. Tosi, S. Lizzit and A. Di Carlo, *Materials*, 2021, **14**, 3954.

51 S. Mejaouri, S. Cacovich, P. Baranek, B. Bérenguier, I. Zimmermann, A. Yaiche, D. Loisnard, J. Rousset and S. Collin, *Small Methods*, 2024, **8**, 2300901.

52 N. Folastre, M. A. A. Kazemi, K. Cherednichneko, A. Jamali, J. Rousset, F. Sauvage and A. Demortière, *Energy Environ. Sci.*, 2024, **17**, 8745.

53 L. A. Frolova, S. Y. Luchkin, Y. Lekina, L. G. Gutsev, S. A. Tsarev, I. S. Zhidkov, E. Z. Kurmaev, Z. X. Shen, K. J. Stevenson, S. M. Aldoshin and P. A. Troshin, *Adv. Energy Mater.*, 2021, **11**, 2002934.

54 A. F. Akbulatov, M. I. Ustinova, L. Gutsev, S. A. Tsarev, N. N. Dremova, I. Zhidkov, S. Y. Luchkin, B. R. Ramachandran, L. Frolova, E. Z. Kurmaev, K. J. Stevenson, S. M. Aldoshin and P. A. Troshin, *Nano Energy*, 2021, **86**, 106082.

55 D. V. Athapaththu, M. E. Kordesch and J. Chen, *J. Phys. Chem. Lett.*, 2024, **15**, 1105.

56 W. Zhu, S. Wang, X. Zhang, A. Wang, C. Wu and F. Hao, *Small*, 2022, **18**, 2105783.

57 R. Burns, D. Chiaro, H. Davison, C. J. Arendse, G. M. King and S. Guha, *Small*, 2025, **21**, 2406815.

58 J. Yang, W. Sheng, R. Li, L. Gong, Y. Li, L. Tan, Q. Lin and Y. Chen, *Adv. Energy Mater.*, 2022, **12**, 2103652.

59 C. Gong, C. Zhang, Q. Zhuang, H. Li, H. Yang, J. Chen and Z. Zang, *Micro & Nano Lett.*, 2023, **15**, 17.

60 S. Cacovich, P. Dally, G. Vidon, M. Legrand, S. Gbegnon, J. Rousset, J.-B. Puel, J.-F. Guillemoles, P. Schulz, M. Bouttemy and A. Etcheberry, *ACS Appl. Mater. Interfaces*, 2022, **14**, 34228.

61 A. Kheralla and N. Chetty, *Heliyon*, 2021, **7**, e06211.

62 W. Rehman, D. P. McMeekin, J. B. Patel, R. L. Milot, M. B. Johnston, H. J. Snaith and L. M. Herz, *Energy Environ. Sci.*, 2017, **10**, 361.

63 S. Moradi, S. Kundu, M. Awais, Y. Haruta, H.-D. Nguyen, D. Zhang, F. Tan and M. I. Saidaminov, *Small*, 2023, **19**, 2301037.

64 C. Zhu, X. Guo, S. Xiao, W. Lin, Z. Chen, L. Zhang, H. Zhang, X. Xiong and Y. Yang, *Adv. Powder Mater.*, 2025, **4**, 100264.

65 R. Sato, Y. Morikawa, K. Yoshida, M. Goto, S. Asakura, M. Kashiwagi, T. Chiba and A. Masuhara, *ACS Appl. Opt. Mater.*, 2024, **2**, 2031.

66 S. De Wolf, J. Holovsky, S.-J. Moon, P. Löper, B. Niesen, M. Ledinsky, F.-J. Haug, J.-H. Yum and C. Ballif, *J. Phys. Chem. Lett.*, 2014, **5**, 1035.

67 E. Ugur, M. Ledinský, T. G. Allen, J. Holovský, A. Vlk and S. DeWolf, *J. Phys. Chem. Lett.*, 2022, **13**, 7702.

68 J. Hieulle, X. Wang, C. Stecker, D.-Y. Son, L. Qiu, R. Ohmann, L. K. Ono, A. Mugarza, Y. Yan and Y. Qi, *J. Am. Chem. Soc.*, 2019, **141**, 3515.

69 L. McGovern, G. Grimaldi, M. H. Futscher, E. M. Hutter, L. A. Muscarella, M. C. Schmidt and B. Ehrler, *ACS Appl. Energy Mater.*, 2021, **4**, 13431.

70 A. J. Knight and L. M. Herz, *Energy Environ. Sci.*, 2020, **13**, 2024.

71 J. Yang, P. Manganaris and A. Mannodi-Kanakkithodi, *J. Chem. Phys.*, 2024, **160**, 064114.

72 H. Park, A. Ali, R. Mall, H. Bensmail, S. Sanvito and F. El-Mellouhi, *Mach. Learn.: Sci. Technol.*, 2021, **2**, 025030.

73 B. Subedi, J. Zuo, M. S. Tumusange, M. M. Junda, K. Ghimire and N. J. Podraza, *Hybrid Perovskite Solar Cells: Characteristics and Operation*, ed. H. Fujiwara, Wiley-VCH GmbH, 2021, ch. 10, pp. 253–273.

74 A. Nandy, A. Roychowdhury, D. Das and S. K. Pradhan, *Powder Technol.*, 2014, **254**, 538.

75 A. Rajagopal, R. J. Stoddard, H. W. Hillhouse and A. K.-Y. Jen, *J. Mater. Chem. A*, 2019, **7**, 16285.

76 H. Gao, D. He, Z. Chen, P. Gao, D. He, Z. Li, X. Zhang, J. Xiu, Q. Sun, S. Chen, S.-H. Wei, S.-H. Yu and Z. He, *Sci. Adv.*, 2025, **11**, eads4038.

77 X. Cai, F. Liu, A. Yu, J. Qin, M. Hatamvand, I. Ahmed, J. Luo, Y. Zhang, H. Zhang and Y. Zhan, *Light: Sci. Appl.*, 2022, **11**, 234.

33006 | *J. Mater. Chem. A*, 2025, **13**, 32964–33011

This journal is © The Royal Society of Chemistry 2025

78 S. Gong, G. Qu, Y. Qiao, Y. Wen, Y. Huang, S. Cai, L. Zhang, K. Jiang, S. Liu, M. Lin, M. C. Beard, Z.-X. Xu and X. Chen, *Energy Environ. Sci.*, 2024, **17**, 5080.

79 Y. Zheng, Y. Li, R. Zhuang, X. Wu, C. Tian, A. Sun, C. Chen, Y. Guo, Y. Hua, K. Meng, K. Wu and C.-C. Chen, *Energy Environ. Sci.*, 2024, **17**, 1153.

80 M. Li, B. Jiao, Y. Peng, J. Zhou, L. Tan, N. Ren, Y. Ye, Y. Liu, Y. Yang, Y. Chen, L. Ding and C. Yi, *Adv. Mater.*, 2024, **36**, 2406532.

81 I. M. Pavlovetc, M. C. Brennan, S. Draguta, A. Ruth, T. Moot, J. A. Christians, K. Aleshire, S. P. Harvey, S. Toso, S. U. Nanayakkara, J. Messinger, J. M. Luther and M. Kuno, *ACS Energy Lett.*, 2020, **5**, 2802.

82 G. Tang, P. Ghosez and J. Hong, *J. Phys. Chem. Lett.*, 2021, **12**, 4227.

83 J. Park, B. J. Kang, G. Seo, J. Kim, T. G. Park, S. Nam, J. J. Yoo, K. Lee, Y. U. Jeong, M. Park, S. S. Shin and F. Rotermund, *Adv. Energy Mater.*, 2025, **15**, 2400225.

84 R. M. dos Santos, I. Ornelas-Cruz, M. P. Lima and J. L. F. Da Silva, *Appl. Mater. Today*, 2025, **44**, 102712.

85 L. Polimante, T. M. G. dos Santos, D. Z. Florio and A. S. Polo, *Mater. Lett.*, 2025, **387**, 138255.

86 D. Klotz, G. Tumen-Ulzii, C. Qin, T. Matsushima and C. Adachi, *RSC Adv.*, 2019, **9**, 33436.

87 A. Mallick and I. Visoly-Fisher, *Mater. Adv.*, 2021, **2**, 6125.

88 T. A. de Souza Carvalho, L. F. Magalhaes, C. I. do Livramento Santos, T. A. Z. de Freitas, B. R. C. Vale, A. F. V. da Fonseca and M. A. Schiavon, *Chem.–Eur. J.*, 2023, **29**, e202202518.

89 Z. Zhang, Y. Liu, Q. Sun, H. Ban, Z. Liu, H. Yu, X. Li, L. Dai, W. Yang, Y. Shen and M. Wang, *Chem. Inorg. Mater.*, 2023, **1**, 100017.

90 S. Wang, C. Chen, Z. Zhang, Y. Cai, Y. Zhang, S. Gao, W. Chen, S. Guo, E. Abduryim, C. Dong, X. Guan, Y. Liu and P. Luc, *Sol. Energy*, 2024, **267**, 112240.

91 H. Näsström, O. Shargaieva, P. Becker, F. Mathies, I. Zizak, V. R. F. Schröder, E. J. W. List-Kratochvil, T. Unold and E. Unger, *J. Mater. Chem. A*, 2022, **10**, 4906.

92 A.-Z. Guo, L.-H. Chou, S.-H. Yang, D. Wang, X.-F. Wang, I. Osaka, H.-W. Lin and C.-L. Liu, *Adv. Mater. Interfaces*, 2021, **8**, 2001509.

93 L. Ma, D. Guo, M. Li, C. Wang, Z. Zhou, X. Zhao, F. Zhang, Z. Ao and Z. Nie, *Chem. Mater.*, 2019, **31**, 8515.

94 M. T. Mbumba, D. M. Malouangou, J. M. Tsiba, L. Bai, Y. Yang and M. Guli, *Sol. Energy*, 2021, **230**, 954.

95 J. Yang, X. Liu, Y. Zhang, X. Zheng, X. He, H. Wang, F. Yue, S. Braun, J. Chen, J. Xu, Y. Li, Y. Jin, J. Tang, C. Duan, M. Fahlman and Q. Bao, *Nano Energy*, 2018, **54**, 218.

96 W. Chi and S. K. Banerjee, *Chem. Mater.*, 2021, **33**, 1540.

97 J. A. Schwenzer, T. Hellmann, B. A. Nejand, H. Hu, T. Abzieher, F. Schackmar, I. M. Hossain, P. Fassl, T. Mayer, W. Jaegermann, U. Lemmer and U. W. Paetzold, *ACS Appl. Mater. Interfaces*, 2021, **13**, 15292.

98 B. Liu, H. Bi, D. He, L. Bai, W. Wang, H. Yuan, Q. Song, P. Su, Z. Zang, T. Zhou and J. Chen, *ACS Energy Lett.*, 2021, **6**, 2526.

99 M. Vásquez-Montoya, J. F. Montoya, D. Ramirez and F. Jaramillo, *J. Energy Chem.*, 2021, **57**, 386.

100 L. A. Muscarella and B. Ehrler, *Joule*, 2022, **6**, 2016.

101 F. Wen, L. Tian, W. Zhang, X. Zhou, P. Lin, S. Zhou, L. Du, T. Hou, W. Yu, L. Yu, G. Duan, C. Peng, Z. Ma, M. Zhang, H. Li and Y. Huang, *CrystEngComm*, 2021, **23**, 8553.

102 J. Fan, Y. Chen, A. Kong, Q. Tan, J. Zhong, L. Zhang, Y. Peng, G. Liang and Z. Ku, *ACS Appl. Energy Mater.*, 2024, **7**, 3740.

103 H. Kim, J. Sin, M. Kim, G. Kim, M. Kim, J. Kim, G. Park, B. Kim, M. S. Jeong and J. Y. Yang, *Sol. RRL*, 2024, **8**, 2300825.

104 M. Wang, S. Tan, Y. Zhao, P. Zhu, Y. Yin, Y. Feng, T. Huang, J. Xue, R. Wang, G. S. Han, H. S. Jung, J. Bian, J.-W. Lee and Y. Yang, *Adv. Funct. Mater.*, 2021, **31**, 2007520.

105 J. J. Jeronimo-Rendon, S.-H. Turren-Cruz, J. Pascual, D. Di Girolamo, M. A. Flatken, H. Köbler, W. Hempel, M. Li, A. Di Carlo, P. P. Boix, I. Mora-Seró, A. Abate and M. Saliba, *Adv. Funct. Mater.*, 2024, **34**, 2313928.

106 Q. Guo, Y. Ding, Z. Dai, Z. Chen, M. Du, Z. Wang, L. Gao, C. Duan, Q. Guo and E. Zhou, *Phys. Chem. Chem. Phys.*, 2022, **24**, 17526.

107 Z. Xing, X. Meng, D. Li, Z. Li, C. Gong, X. Hu, T. Hu and Y. Chen, *Sci. China Mater.*, 2023, **66**, 2573.

108 Y. Qian, J. Li, H. Cao, Z. Ren, X. Dai, T. Huang, S. Zhang, Y. Qiu, L. Yang and S. Yin, *Adv. Funct. Mater.*, 2023, **33**, 2214731.

109 H. Aqoma, S.-H. Lee, I. F. Imran, J.-H. Hwang, S.-H. Lee and S.-Y. Jang, *Nat. Energy*, 2024, **9**, 324.

110 J. Y. D. Roh, D. E. Sommer, T. J. Milstein, S. T. Dunham and D. R. Gamelin, *Chem. Mater.*, 2023, **35**, 8057.

111 J. Xi, H. Duim, M. Pitaro, K. Gahlot, J. Dong, G. Portale and M. A. Loi, *Adv. Funct. Mater.*, 2021, **31**, 2105734.

112 N. Livakas, S. Toso, Y. P. Ivanov, T. Das, S. Chakraborty, G. Divitini and L. Manna, *J. Am. Chem. Soc.*, 2023, **145**, 20442.

113 K. Gahlot, J. Meijer and L. Protesescu, *Nanoscale*, 2024, **16**, 5177.

114 Y. Liu, F. Li, Q. Li, K. Yang, T. Guo, X. Li and H. Zeng, *ACS Photonics*, 2018, **5**, 4504.

115 T. Elmelund, R. A. Scheidt, B. Seger and P. V. Kamat, *ACS Energy Lett.*, 2019, **4**, 1961.

116 D. Zheng, T. Zhu, Y. Yan and T. Pauporté, *Adv. Energy Mater.*, 2022, **12**, 2103618.

117 Y. Bai, R. Tian, K. Sun, C. Liu, X. Lang, M. Yang, Y. Meng, C. Xiao, Y. Wang, X. Lu, J. Wang, H. Pan, Z. Song, S. Zhou and Z. Ge, *Energy Environ. Sci.*, 2024, **17**, 8557.

118 Y. Xing, Z. Deng, T. Guo, Z. Zhang, Q. Tai, R. Zhao, J. Xiong, Q. Wang, L. Huang, X. Liu, Z. Hu, Y. Zhu and J. Zhang, *Chem. Eng. J.*, 2023, **462**, 142122.

119 S.-H. Turren-Cruz, J. Pascual, S. Hu, J. Sanchez-Diaz, S. Galve-Lahoz, W. Liu, W. Hempel, V. S. Chirvony, J. P. Martinez-Pastor, P. P. Boix, A. Wakamiya and I. Mora-Seró, *ACS Energy Lett.*, 2024, **9**, 432.

120 Z. Zhang, J. Liang, J. Wang, Y. Zheng, X. Wu, C. Tian, A. Sun, Y. Huang, Z. Zhou, Y. Yang, Y. Liu, C. Tang and C.-C. Chen, *Adv. Energy Mater.*, 2023, **13**, 2300181.

This journal is © The Royal Society of Chemistry 2025

J. Mater. Chem. A, 2025, **13**, 32964–33011 | **33007**

121 X. Yang, Y. Zhu, S. Yan, H. Hu, C. Chen and J. Tang, *Sol. RRL*, 2025, **9**, 2500149.

122 R. Liu, X. Zheng, Z. Wang, M. Zeng, C. Lan, S. Yang, S. Li, A. Wang, M. Li, J. Guo, X. Weng, Y. Rong and X. Li, *J. Energy Chem.*, 2025, **100**, 646.

123 I. Susic, A. Kama, L. Gil-Escrig, C. Dreessen, F. Palazon, D. Cahen, M. Sessolo and H. J. Bolink, *Adv. Mater. Interfaces*, 2023, **10**, 2202271.

124 L. Gil-Escrig, I. Susic, İ. Doğan, V. Zardetto, M. Najafi, D. Zhang, S. Veenstra, S. Sedani, B. Arikan, S. Yerci, H. J. Bolink and M. Sessolo, *Adv. Funct. Mater.*, 2023, **33**, 2214357.

125 S. Yang, Q. Song, L. Chao, D. Li and Y. Wang, *Adv. Theory Simul.*, 2024, **7**, 2300619.

126 G. Bravetti, N. Taurisano, A. Moliterni, J. M. Vicent-Luna, D. Altamura, F. Aiello, N. Vanni, A.-L. Capodilupo, S. Carallo, G. Gigli, G. Uccello-Barretta, F. Balzano, C. Giannini, S. Tao, S. Colella and A. Rizzo, *Chem. Mater.*, 2024, **36**, 3150.

127 R. Singh, S. R. Suranagi, M. Kumar and V. K. Shukla, *J. Appl. Phys.*, 2017, **122**, 235302.

128 L.-C. Chen, C.-H. Tien, Y.-C. Jhou and W.-C. Lin, *Energies*, 2020, **13**, 2438.

129 K.-W. Huang, M.-H. Li, S.-H. Wu, P.-T. Chiu, J.-A. Chen, Y.-H. Chen, C.-F. Lin, Y.-L. Tung and P. Chen, *Energy Technol.*, 2021, **9**, 2000792.

130 K.-H. Hwang, S. H. Nam, D. I. Kim, H. J. Seo and J.-H. Boo, *Sol. Energy Mater. Sol. Cell.*, 2018, **180**, 386.

131 X. Wang, Y. Fan, L. Wang, C. Chen, Z. Li, R. Liu, H. Meng, Z. Shao, X. Du, H. Zhang, G. Cui and S. Pang, *Chem*, 2020, **6**, 1369.

132 H. Min, G. Kim, M. J. Paik, S. Lee, W. S. Yang, M. Jung and S. I. Seok, *Adv. Energy Mater.*, 2019, **9**, 1803476.

133 B. Wilk, S. Öz, E. Radicchi, F. Ünlü, T. Ahmad, A. P. Herman, F. Nunzi, S. Mathur, R. Kudrawiec and K. Wojciechowski, *ACS Sustainable Chem. Eng.*, 2021, **9**, 3920.

134 Z. Li, Z. Xing, H. Peng, X. Meng, D. Li, L. Huang, X. Hu, T. Hu and Y. Chen, *Adv. Energy Mater.*, 2022, **12**, 2200650.

135 R. Szostak, S. Sanchez, P. E. Marchezi, A. S. Marques, J. C. Silva, M. S. Holanda, A. Hagfeldt, H. C. N. Tolentino and A. F. Nogueira, *Adv. Funct. Mater.*, 2021, **31**, 2007473.

136 Y. Ding, B. Ding, P. Shi, J. Romano-deGea, Y. Li, R. C. Turnell-Ritson, O. A. Syzgantseva, I. Yavuz, M. Xia, R. Yu, M. A. Syzgantseva, J.-N. Audinot, X. Miao, X. Liao, J. Li, P. Dörflinger, V. Dyakonov, C. Liu, Y. Yang, L. Tao, K. G. Brooks, A. Slonopas, J. Pan, L. Zhang, Q. An, Y. Rong, J. Peng, L. Ding, E. Shi, L. Mai, S. Dai, K. Zhao, J. Sheng, R. Wang, P. J. Dyson and M. K. Nazeeruddin, *Science*, 2024, **386**, 531.

137 E. Ugur, A. A. Said, P. Dally, S. Zhang, C. E. Petoukhoff, D. Rosas-Villalva, S. Zhumagali, B. K. Yildirim, A. Razzaq, S. Sarwade, A. Yazmaciyan, D. Baran, F. Laquai, C. Deger, I. Yavuz, T. G. Allen, E. Aydin and S. De Wolf, *Science*, 2024, **385**, 533.

138 Y. Wang, Y. Cheng, C. Yin, J. Zhang, J. You, J. Wang, J. Wang and J. Zhang, *Micro & Nano Lett.*, 2024, **16**, 183.

139 X. Yang, Y. Ni, Y. Zhang, Y. Wang, W. Yang, D. Luo, Y. Tu, Q. Gong, H. Yu and R. Zhu, *ACS Energy Lett.*, 2021, **6**, 2404.

140 C. Ma, C. Zhang, S. Chen, Y. Ye, L. Sun, L. Gao, Y. Sulaiman, T. Maa and M. Chen, *Sol. Energy Mater. Sol. Cell.*, 2023, **262**, 112499.

141 Y. Bai, T. Wang, J. Yang, X. Pu, B. Xue, H. Chen, X. He, G. Feng, S. Jia, J. Yin, C. Qi and X. Li, *J. Mater. Sci. Technol.*, 2025, **212**, 281.

142 C. Zhang, H. Li, C. Gong, Q. Zhuang, J. Chen and Z. Zang, *Energy Environ. Sci.*, 2023, **16**, 3825.

143 Z. Zhu, K. Mao, K. Zhang, W. Peng, J. Zhang, H. Meng, S. Cheng, T. Li, H. Lin, Q. Chen, X. Wu and J. Xu, *Joule*, 2022, **6**, 2849.

144 G. Al-Dainy, F. Watanabe, A. S. Biris and S. E. Bourdo, *ACS Appl. Energy Mater.*, 2021, **4**, 3297.

145 Q. Feng, X. Huang, Z. Tang, Y. Hou, Q. Chang, S. Nie, F. Cao, X. Niu, J. Yin, J. Li, N. Zheng and B. Wu, *Energy Environ. Sci.*, 2022, **15**, 4404.

146 L. Shi, T. L. Young, J. Kim, Y. Sheng, L. Wang, Y. Chen, Z. Feng, M. J. Keevers, X. Hao, P. J. Verlinden, M. A. Green and A. W. Y. Ho-Baillie, *ACS Appl. Mater. Interfaces*, 2017, **9**, 25073.

147 Y. Wang, I. Ahmad, T. Leung, J. Lin, W. Chen, F. Liu, A. M. C. Ng, Y. Zhang and A. B. Djurisǐc, *ACS Mater. Au*, 2022, **2**, 215.

148 Y.-J. Kang and S.-I. Na, *Nano Energy*, 2022, **97**, 107193.

149 A. Shukla, D. B. Khadka, C. Li, M. Rikukawa, Y. Takeoka, R. Sahara, M. Yanagida and Y. Shirai, *J. Mater. Chem. A*, 2025, **13**, 23487, Advance Article.

150 Y. Fu, W. Shao, Z. Deng and W. Wu, *Chem. Eng. J.*, 2025, **503**, 158282.

151 B. G. Krishna, D. S. Ghosh and S. Tiwari, *Sol. Energy*, 2021, **224**, 1369.

152 L. Lang, Z. Ding, Y. Du, N. Wu, P. Liu, R. Qin, S. Wang, Z. Wang, Y. Tu, X. Liu, Z. Zhang, Y. Gong, D. Liu, K. Zhao and S. Liu, *Adv. Energy Mater.*, 2025, 2405423.

153 T. Li, S. Wang, J. Yang, X. Pu, B. Gao, Z. He, Q. Cao, J. Han and X. Li, *Nano Energy*, 2021, **82**, 105742.

154 G. Liu, H. Zheng, L. Zhang, H. Xu, S. Xu, X. Xu, Z. Liang and X. Pana, *Chem. Eng. J.*, 2021, **407**, 127204.

155 W. Shao, H. Wang, F. Ye, C. Wang, C. Liu, S. Zhou, C. Tao and G. Fang, *J. Power Sources*, 2022, **520**, 230900.

156 Q. Wang, W. Tang, Y. Chen, W. Qiu, Y. Wu and Q. Peng, *J. Mater. Chem. A*, 2023, **11**, 1170.

157 Q. Wang, Y. Chen, X. Chen, W. Tang, W. Qiu, X. Xu, Y. Wu and Q. Peng, *Adv. Mater.*, 2024, **36**, 2307709.

158 Z. He, S. Zhang, Y. Gao, Q. Geng, X. Jia, S. Yang, Z. Zhang, Y. Zheng, Y. Hu, C. Yao and Q. Zhang, *J. Energy Chem.*, 2023, **87**, 390.

159 W. Zeng, X. He, H. Bian, P. Guo, M. Wang, C. Xu, G. Xu, Y. Zhong, D. Lu, Z. Sofer, Q. Song and S. Zhang, *ACS Appl. Mater. Interfaces*, 2022, **14**, 43975.

160 S. Mehmood, N. Shahzad, S. Nadeem, M. S. Qureshi, A. Sattar, H. Pervaiza, N. Iqbal, R. Liaquat and M. I. Shahzad, *J. Mol. Struct.*, 2025, **1321**, 139864.

33008 | *J. Mater. Chem. A*, 2025, **13**, 32964–33011

This journal is © The Royal Society of Chemistry 2025

161 B. Liu, R. Li, Q. Zhuang, X. Yu, S. Gong, D. He, Q. Zhou, H. Yang, X. Chen, S. Lu, Z.-X. Xu, Z. Zang and J. Chen, *J. Energy Chem.*, 2023, **76**, 277.

162 Z. Li, B. Li, X. Wu, S. A. Sheppard, S. Zhang, D. Gao, N. J. Long and Z. Zhu, *Science*, 2022, **376**, 416.

163 D.-G. Lee, P. Pandey, B. Parid, J. Ryu, S. W. Cho, J.-K. Kim and D.-W. Kang, *Energy*, 2022, **257**, 124640.

164 Q. Chen, M. Ma, W. Li, Y. Wang, Y. Gao, Y. Li and C. Liu, *ACS Appl. Mater. Interfaces*, 2025, **17**, 5193.

165 F. Z. Li, X. Deng, F. Qi, Z. Li, D. J. Liu, D. Shen, M. C. Qin, S. F. Wu, F. Lin, S. H. Jang, J. Zhang, X. Lu, D. Lei, C.-S. Lee, Z. Zhu and A. K.-Y. Jen, *J. Am. Chem. Soc.*, 2020, **142**, 20134.

166 F. Wang, W. Geng, Y. Zhou, H.-H. Fang, C.-J. Tong, M. A. Loi, L.-M. Liu and N. Zhao, *Adv. Mater.*, 2016, **28**, 9986.

167 F. H. Isikgor, F. Furlan, J. Liu, E. Ugur, M. K. Eswaran, A. S. Subbiah, E. Yengel, M. De Bastiani, G. T. Harrison, S. Zhumagali, C. T. Howells, E. Aydin, M. Wang, N. Gasparini, T. G. Allen, A. Rehman, E. V. Kerschaver, D. Baran, I. McCulloch, T. D. Anthopoulos, U. Schwingenschlög, F. Laquai and S. De Wolf, *Joule*, 2021, **5**, 1566.

168 M. Wang, Y. Zhao, X. Jiang, Y. Yin, I. Yavuz, P. Zhu, A. Zhang, G. S. Han, H. S. Jung, Y. Zhou, W. Yang, J. Bian, S. Jin, J.-W. Lee and Y. Yang, *Joule*, 2022, **6**, 1032.

169 M. Liu, J. Zhang, S. Qin, X. Miao, M. Yuan, Z. Liu, Y. Wang, Y. Feng, X. Jiang, R. Wu, L. Yi, L. Meng and Y. Li, *J. Am. Chem. Soc.*, 2024, **146**, 32105.

170 J. Wang, S. Fu, X. Liu, H. Yuan, Z. Xu, C. Wang, J. Zhang, L. Huang, Z. Hu and Y. Zhu, *J. Alloys Compd.*, 2021, **891**, 161971.

171 K. Cao, Y. Cheng, W. Zuo, B. Cai, Y. Wu, J. Zhu, Y. Zhu, H. Ning, Y. Shen, W. Shen, L. Liu and S. Chen, *J. Power Sources*, 2023, **558**, 232595.

172 W. Wu, X. Dong, G. Liu, X. Pan and H. Zheng, *Chem. Eng. J.*, 2023, **452**, 139535.

173 L. Wang, Z. Yan, J. Qiu, J. Wu, C. Zhen, K. Tai, X. Jiang and S. Yang, *Nano Energy*, 2021, **90**, 106537.

174 D. Yao, C. Zhang, S. Zhang, Y. Yang, A. Du, E. Waclawik, X. Yu, G. J. Wilson and H. Wang, *ACS Appl. Mater. Interfaces*, 2019, **11**, 29753.

175 M. Hu, S. Du, Z. Yu, G. Chen, J. Liang, Q. Cai and G. Fang, *Chem. Eng. J.*, 2025, **505**, 159453.

176 A. H. Proppe, A. Johnston, S. Teale, A. Mahata, R. Quintero-Bermudez, E. H. Jung, L. Grater, T. Cui, T. Filleter, C.-Y. Kim, S. O. Kelley, F. De Angelis and E. H. Sargent, *Nat. Commun.*, 2021, **12**, 3472.

177 M. Li, J. Zhou, L. Tan, Y. Liu, S. Wang, C. Jiang, H. Li, X. Zhao, X. Gao, W. Tress, L. Ding and C. Yi, *Energy Environ. Mater.*, 2023, **6**, e12360.

178 Z. Kong, S. Ding, X. Li, J. Xu, M. Cai, G. Jia, T. Zhang, T. Sun and C. Xiang, *Chem. Commun.*, 2025, DOI: [10.1039/D5CC01378J](https://doi.org/10.1039/D5CC01378J).

179 W. Li, X. Lai, F. Meng, G. Li, K. Wang, A. K. K. Kyaw and X. W. Sun, *Sol. Energy Mater. Sol. Cell.*, 2020, **211**, 110527.

180 B. Wang, H. Li, Q. Dai, M. Zhang, Z. Zou, J.-L. Bredas and Z. Lin, *Angew. Chem., Int. Ed.*, 2021, **60**, 17664.

181 Z. Iqbal, F. Zu, A. Musiienko, E. Gutierrez-Partida, H. Köbler, T. W. Gries, G. V. Sannino, L. Canil, N. Koch, M. Stolterfoht, D. Neher, M. Pavone, A. B. Muñoz-García, A. Abate and Q. Wang, *ACS Energy Lett.*, 2023, **8**, 4304.

182 R. Zheng, J. Li, S. Li, B. He and S. Chen, *Sustainable Energy Fuels*, 2025, **9**, 3831.

183 S. Thokala, R. K. Gupta, A. Garg and S. P. Singh, *Sol. Energy*, 2021, **226**, 483.

184 S. Wang, D. Khan, W. Zhou, Y. Sui, T. Zhang, G. Yu, Y. Huang, X. Yang, X. Chen, H. Yan, J. Tang, F. Yang, P. Han, Z. Zheng, Y. Zhang and Z. Tang, *Adv. Funct. Mater.*, 2024, **34**, 2316202.

185 Q. Zhang, Q. Zhao, H. Wang, Y. Yao, L. Li, Y. Wei, R. Xu, C. Zhang, E. O. Shalenov, Y. Tu, K. Wang and M. Xiao, *Micro & Nano Lett.*, 2025, **17**, 107.

186 X. Chen, Q. Wang, H. Wei, J. Yang, Y. Yao, W. Tang, W. Qiu, X. Xu, L. Song, Y. Wu and Q. Peng, *Energy Environ. Sci.*, 2024, **17**, 7342.

187 L. Merten, A. Hinderhofer, T. Baumeler, N. Arora, J. Hagenlocher, S. M. Zakeeruddin, M. I. Dar, M. Grätzel and F. Schreiber, *Chem. Mater.*, 2021, **33**, 2769.

188 S. Maniyarasu, J. C.-R. Ke, B. F. Spencer, A. S. Walton, A. G. Thomas and W. R. Flavell, *ACS Appl. Mater. Interfaces*, 2021, **13**, 43573.

189 B. P. Kore, M. Jamshidi and J. M. Gardner, *Mater. Adv.*, 2024, **5**, 2200.

190 B. Nambiraj, A. K. Ravindran, S. P. Muthu and R. Perumalsamy, *Small Methods*, 2025, **9**, 2400768.

191 E. A. Alharbi, T. P. Baumeler, A. Krishna, A. Y. Alyamani, F. T. Eickemeyer, O. Ouellette, L. Pan, F. S. Alghamdi, Z. Wang, M. H. Alotaibi, B. Yang, M. Almalki, M. D. Mensi, H. Albrithen, A. Albadri, A. Hagfeldt, S. M. Zakeeruddin and M. Grätzel, *Adv. Energy Mater.*, 2021, **11**, 2003785.

192 I. Mesquita, L. Andrade and A. Mendes, *ChemSusChem*, 2019, **12**, 2186.

193 W. Tress, K. Domanski, B. Carlsen, A. Agarwalla, E. A. Alharbi, M. Graetzel and A. Hagfeldt, *Nat. Energy*, 2019, **4**, 568.

194 J. Ruellou, H. Ahouari, M. Courty and H. V. F. Sauvage, *EES Sol.*, 2025, **1**, 172.

195 I. Susic, L. Gil-Escrig, K. P. S. Zanoni, C. Roldán-Carmona, M. Sessolo and H. J. Bolink, *ACS Mater. Lett.*, 2023, **5**, 3299.

196 I. Susic, L. Gil-Escrig, F. Palazon, M. Sessolo and H. J. Bolink, *ACS Energy Lett.*, 2022, **7**, 1355.

197 A. Tejada, S. Peters, A. Al-Ashouri, S. H. Turren-Cruz, A. Abate, S. Albrecht, F. Ruske, B. Rech, J. A. Guerra and L. Korte, *Adv. Opt. Mater.*, 2022, **10**, 2101553.

198 A. Farooq, M. R. Khan, T. Abzieher, A. Voigt, D. C. Lupascu, U. Lemmer, B. S. Richards and U. W. Paetzold, *ACS Appl. Energy Mater.*, 2021, **4**, 3083.

199 V. V. Ozerova, N. A. Emelianov, D. P. Kiryukhin, P. P. Kushch, G. V. Shilov, G. A. Kichigina, S. M. Aldoshin, L. A. Frolova and P. A. Troshin, *J. Phys. Chem. Lett.*, 2023, **14**, 743.

200 M. I. Ustinova, M. N. Sarychev, N. A. Emelianov, Y. Li, Y. Zhuo, T. Zheng, S. D. Babenko, E. D. Tarasov,

This journal is © The Royal Society of Chemistry 2025

J. Mater. Chem. A, 2025, **13**, 32964–33011 | **33009**

P. P. Kushch, N. N. Dremova, G. A. Kichigina, A. V. Rasmetyeva, A. I. Kukharenko, D. P. Kiryukhin, E. Z. Kurmaev, X. Xu, P. A. Troshin, L. A. Frolova and I. S. Zhidkov, *EcoMat*, 2025, **7**, e12512.

201 H. P. Parkhomenko, M. M. Solovan, S. Sahare, A. I. Mostovyi, D. Aidarkhanov, N. Schopp, T. Kovaliuk, M. Kaikanov, A. Ng and V. V. Brus, *Adv. Funct. Mater.*, 2024, **34**, 2310404.

202 A. Farooq, M. R. Khan, T. Abzieher, A. Voigt, D. C. Lupascu, U. Lemmer, B. S. Richards and U. W. Paetzold, *ACS Appl. Energy Mater.*, 2021, **4**, 3083.

203 Y. Hui, Y.-Y. Tan, L. Chen, Z.-A. Nan, J.-Z. Zhou, J.-W. Yan and B.-W. Mao, *Adv. Funct. Mater.*, 2021, **31**, 2103894.

204 N. A. Emelianov, V. V. Ozerova, Y. S. Fedotov, E. V. Shchurik, N. A. Slesarenko, M. V. Zhidkov, E. V. Golosov, R. R. Saifutyarov, L. A. Frolova and P. A. Troshin, *Sol. Energy Mater. Sol. Cells*, 2025, **282**, 113305.

205 P. V. Kamat and M. Kuno, *Acc. Chem. Res.*, 2021, **54**, 520.

206 Z. Wang, L. Zeng, T. Zhu, H. Chen, B. Chen, D. J. Kubicki, A. Balvanz, C. Li, A. Maxwell, E. Ugur, R. dos Reis, M. Cheng, G. Yang, B. Subedi, D. Luo, J. Hu, J. Wang, S. Teale, S. Mahesh, S. Wang, S. Hu, E. D. Jung, M. Wei, S. M. Park, L. Grater, E. Aydin, Z. Song, N. J. Podraza, Z.-H. Lu, J. Huang, V. P. Dravid, S. De Wolf, Y. Yan, M. Grätzel, M. G. Kanatzidis and E. H. Sargent, *Nature*, 2023, **618**, 74.

207 L. Zhang, Y. Chen, Z. Zheng, Y. Zhou, C. Li, G. Li, B. Ren, Z. Hu, H. Zhou, F. Ren, W. Ke and G. Fang, *Adv. Funct. Mater.*, 2025, 2423450.

208 Y. Liu, Y. Zhang, X. Zhu, J. Feng, I. Spanopoulos, W. Ke, Y. He, X. Ren, Z. Yang, F. Xiao, K. Zhao, M. Kanatzidis and S. Liu, *Adv. Mater.*, 2021, **33**, 2006010.

209 P. Subudhi, S. Sivapatham, R. Narasimhan A, B. Kumar and D. Punetha, *J. Power Sources*, 2025, **639**, 236639.

210 O. Hakami, J. F. Rasheed, T. Zelai, F. Khan, A. S. Alshomrany and F. Khan, *Sol. Energy*, 2024, **274**, 112590.

211 V. V. Ozerova, N. A. Emelianov, L. G. Gutsev, D. V. Korchagin, G. V. Shilov, N. N. Dremova, B. R. Ramachandran, A. Y. Sukhorukov, S. M. Aldoshin, L. A. Frolova and P. A. Troshin, *Mater. Today Chem.*, 2023, **30**, 101590.

212 Y. Ding, S. Lu, J. Chang, E. Feng, H. Li, C. Long, Y. Yang, C. Yi, Z. Zheng, L. Ding and J. Yang, *Small*, 2025, **21**, 2410601.

213 Y. Zhu, Y. Kang, H. Huang, D. Zhuang, M. Li, Z. Ling, K. Peng, L. Zhai and C. Zou, *J. Mater. Chem. A*, 2024, **12**, 2916.

214 F. Deng, S. Li, X. Sun, H. Li and X. Tao, *ACS Appl. Mater. Interfaces*, 2022, **14**, 52163.

215 G. Hu, Z. Li, Q. Zou, S. Zhou, S. Liang, L. Huang, H. Duan, J. Hu, H. Hou, L. Xu, C. Chen, J. Tang and J. Yang, *Environ. Sci. Technol. Lett.*, 2025, **12**, 1062.

216 Q. Zhuang, K. Wang, H. Li, Z. Liu, Y. Li, Y. Yang, Q. Lin, C. Gong, C. Zhang, Z. Guo, S. M. H. Qaid, I. Mora-Sero,

Z. Xu, Z. Zang and H. Wang, *Nano Energy*, 2025, **134**, 110547.

217 L. A. Castriotta, E. Calabro, F. Di Giacomoa, S. H. Reddy, D. Takhellambam, B. Paci, A. Generosi, L. Serenelli, F. Menchini, L. Martini, M. Tucci and A. Di Carlo, *Nano Energy*, 2023, **109**, 108268.

218 G. Li, X. Zou, J. Cheng, D. Chen, Y. Yao, C. Chang, X. Yu, Z. Zhou, J. Wang and B. Liu, *Molecules*, 2020, **25**, 732.

219 A. Listorti, E. J. Juarez-Perez, C. Frontera, V. Roiati, L. Garcia-Andrade, S. Colella, A. Rizzo, P. Ortiz and I. Mora-Sero, *J. Phys. Chem. Lett.*, 2015, **6**, 1628.

220 Y. Chen, J. Yin, Q. Wei, C. Wang, X. Wang, H. Ren, S. F. Yu, O. M. Bakr, O. F. Mohammed and M. Li, *Nat. Photonics*, 2022, **16**, 485.

221 N. K. Tailor, S. P. Senanayak, M. Abdi-Jalebi and S. Satapathi, *Electrochim. Acta*, 2021, **386**, 138430.

222 B. Mohanty, B. N. Parida and R. K. Parida, *Mater. Chem. Phys.*, 2019, **225**, 91.

223 M. S. Sheikh, A. P. Sakhya, A. Dutta and T. P. Sinha, *Thin Solid Films*, 2017, **638**, 277.

224 S. P. Senanayak, M. Abdi-Jalebi, V. S. Kamboj, R. Carey, R. Shivanna, T. Tian, G. Schweicher, J. Wang, N. Giesbrecht, D. Di Nuzzo, H. E. Beere, P. Docampo, D. A. Ritchie, D. Fairen-Jimenez, R. H. Friend and H. Sirringhaus, *Sci. Adv.*, 2020, **6**, eaaz4948.

225 D. W. deQuilettes, W. Zhang, V. M. Burlakov, D. J. Graham, T. Leijtens, A. Osherov, V. Bulovic, H. J. Snaith, D. S. Ginger and S. D. Stranks, *Nat. Commun.*, 2016, **7**, 11683.

226 M. Mączka, J. K. Zaręba, A. Gągor, D. Stefańska, M. Ptak, K. Roleder, D. Kajewski, A. Soszyński, K. Fedoruk and A. Sieradzki, *Chem. Mater.*, 2021, **33**, 2331.

227 M. I. Saidaminov, K. Williams, M. Wei, A. Johnston, R. Quintero-Bermudez, M. Vafaie, J. M. Pina, A. H. Proppe, Y. Hou, G. Walters, S. O. Kelley, W. A. Tisdale and E. H. Sargent, *Nat. Mater.*, 2020, **19**, 412.

228 Y. He, Z. Tang, B. He, C. Han, L. Ding, X. Gu, Y. Zhang, H. Yan and X. Xu, *RSC Adv.*, 2023, **13**, 7886.

229 C. Zhu, X. Niu, Y. Fu, N. Li, C. Hu, Y. Chen, X. He, G. Na, P. Liu, H. Zai, Y. Ge, Y. Lu, X. Ke, Y. Bai, S. Yang, P. Chen, Y. Li, M. Sui, L. Zhang, H. Zhou and Q. Chen, *Nat. Commun.*, 2019, **10**, 815.

230 T. Wang, J. Yang, Q. Cao, X. Pu, Y. Li, H. Chen, J. Zhao, Y. Zhang, X. Chen and X. Li, *Nat. Commun.*, 2023, **14**, 1342.

231 Y. Yuan, Y. Cao, Z. Yang, S. Liu and J. Feng, *Adv. Funct. Mater.*, 2024, **34**, 2405556.

232 L. Zheng, Y. Ma, S. Chu, S. Wang, B. Qu, L. Xiao, Z. Chen, Q. Gong, Z. Wu and X. Hou, *Nanoscale*, 2014, **6**, 8171.

233 Z. Du, Z. Ma, T. Yu, Z. Huang, S. Hou, Q. Liu, Y. Li, Y. Chen, Q. Yang, W. You, J. Yang, H. Du, Y. Li, Q. Zhang, F. Gou, Z. Lv, D. Xiang, C. Huang, J. Yu, Y. Xiang, K. Sun, L. Ding and F. Zhang, *Chem. Eng. J.*, 2025, **503**, 158587.

234 A. Z. Afshord, B. E. Uzuner, W. Soltanpoor, S. H. Sedani, T. Aernouts, G. Gunbas, Y. Kuang and S. Yerci, *Adv. Funct. Mater.*, 2023, **33**, 2301695.

235 J. Huang, D. Zhou, H. Yan, C. Meng, Y. Yang, J. Liu, M. Wang, P. Xu, Z. Peng, J. Chen and G. Li, *J. Mater. Chem. C*, 2024, **12**, 4112.

33010 | *J. Mater. Chem. A*, 2025, **13**, 32964–33011

This journal is © The Royal Society of Chemistry 2025

236 X. Huo, Y. Jiang, J. Lv, W. Sun, W. Liu, R. Yin, Y. Gao, K. Wang, T. You and P. Yin, *Chem. Eng. J.*, 2024, **484**, 149626.

237 B. Zong, Q. Sun, J. Deng, X. Meng, Z. Zhang, B. Kang, S. R. P. Silva and G. Lu, *J. Colloid Interface Sci.*, 2022, **614**, 415.

238 J. Su, T. Hu, X. Chen, X. Zhang, N. Fang, J. Hao, H. Guo, S. Jiang, D. Gu, J. Qiu, H. Zhang and Z. Zhou, *Adv. Funct. Mater.*, 2024, **34**, 2406324.

239 F. H. Isikgor, S. Zhumagali, L. V. T. Merino, M. De Bastiani, I. McCulloch and S. De Wolf, *Nat. Rev. Mater.*, 2023, **8**, 89.

240 H. Zhu, S. Teale, M. N. Lintangpradipto, S. Mahesh, B. Chen, M. D. McGehee, E. H. Sargent and O. M. Bakr, *Nat. Rev. Mater.*, 2023, **8**, 569.

241 F. H. Isikgor, R. R. Pradhan, S. Zhumagali, T. Maksudov, D. Naphade, C. E. Petoukhoff, J. I. Khan, V. Hnapovskyi, G. T. Harrison, C. Combe, J. Liu, A. Marsh, E. A. Alharbi, M. Heeney, F. Laquai, U. Schwingenschlögl, T. D. Anthopoulos and S. De Wolf, *Adv. Energy Mater.*, 2025, **15**, 2402630.

242 J. Liu, X. Chen, K. Chen, W. Tian, Y. Sheng, B. She, Y. Jiang, D. Zhang, Y. Liu, J. Qi, K. Chen, Y. Ma, Z. Qiu, C. Wang, Y. Yin, S. Zhao, J. Leng, S. Jin, W. Zhao, Y. Qin, Y. Su, X. Li, X. Li, Y. Zhou, Y. Zhou, F. Ling, A. Mei and H. Han, *Science*, 2024, **383**, 1198.

243 L. Yue, B. Yan, M. Attridge and Z. Wang, *Sol. Energy*, 2016, **124**, 143.

244 J. Chen, L. Zuo, Y. Zhang, X. Lian, W. Fu, J. Yan, J. Li, G. Wu, C.-Z. Li and H. Chen, *Adv. Energy Mater.*, 2018, **8**, 1800438.

245 P. Shi, J. Xu, I. Yavuz, T. Huang, S. Tan, K. Zhao, X. Zhang, Y. Tian, S. Wang, W. Fan, Y. Li, D. Jin, X. Yu, C. Wang, X. Gao, Z. Chen, E. Shi, X. Chen, D. Yang, J. Xue, Y. Yang and R. Wang, *Nat. Commun.*, 2024, **15**, 2579.

246 A. Mortadi, E. E. Hafidi, M. Monkade and R. E. Moznine, *Mater. Sci. Energy Technol.*, 2024, **7**, 158.

247 L. Liu, P. Liu, S. Ullah, S.-E. Yang, H. Guo, L. Wang, X. Wang and Y. Chen, *Sol. Energy*, 2021, **228**, 274.

248 E. Raza, Z. Ahmad, F. Aziz, M. Asif, M. Q. Mehmood, J. Bhadra and N. J. Al-Thani, *Heliyon*, 2023, **9**, e13477.

249 Y. Guo, F. Zhao, X. Wang, J. Tao, D. Zheng, J. Jiang, Z. Hu and J. Chu, *Sol. Energy Mater. Sol. Cells*, 2021, **221**, 110918.

250 O. Madkhali, J. F. Rasheed and F. Khan, *Sol. Energy*, 2024, **276**, 112674.

251 Q. Ye, W. Hu, Y. Wei, J. Zhu, B. Yao, K. Ren, C. Li, B. Shi, T. Li, F. Ye and Z. Fang, *J. Phys. Chem. Lett.*, 2023, **14**, 1140.

252 Q. Jiang, R. Tirawat, R. A. Kerner, E. A. Gaulding, Y. Xian, X. Wang, J. M. Newkirk, Y. Yan, J. J. Berry and K. Zhu, *Nature*, 2023, **623**, 313.

253 T. M. Shimpi, C. Moffett, W. S. Sampath and K. L. Barth, *Sol. Energy*, 2019, **187**, 226.

254 P. Mariani, M. Á. Molina-García, J. Barichello, M. I. Zappia, E. Magliano, L. A. Castriotta, L. Gabatel, S. B. Thorat, A. E. D. R. Castillo, F. Drago, E. Leonardi, S. Pescetelli, L. Vesce, F. D. Giacomo, F. Matteocci, A. Agresti, N. D. Giorgi, S. Bellani, A. D. Carlo and F. Bonaccorso, *Nat. Commun.*, 2024, **15**, 4552.

255 K. Jung, K. Oh, D. H. Kim, J. W. Choi, K. C. Kim and M.-J. Lee, *Nano Energy*, 2021, **89**, 106387.

256 F. Elmourabit, L. Limouny and S. Dlimi, *Results Eng.*, 2025, **25**, 103919.

257 J. Chen, Y. Zhan, Z. Yang, Y. Zang, W. Yan and X. Li, *Mater. Today Energy*, 2025, **48**, 101769.

258 M. Mammeri, L. Dehimi, H. Bencheri and F. Pezzimenti, *Sol. Energy*, 2023, **249**, 651.

259 X. Zhao, T. Liu, Q. C. Burlingame, T. Liu, R. Holley III, G. Cheng, N. Yao, F. Gao and Y.-L. Loo, *Science*, 2022, **377**, 307.

260 R. K. Gupta, D. K. Kumar, V. Sudhakar, J. M. Beckedahl, A. Abate, E. A. Katz and I. Visoly-Fisher, *Adv. Energy Mater.*, 2025, **15**, 2403844.

261 D. A. Chalkias, A. Karavioti, G. C. Papanicolaou and E. Stathatos, *Electrochim. Acta*, 2022, **427**, 140905.

262 F. Ren, Q. Lu, X. Meng, J. Zhou, R. Chen, J. Wang, H. Wang, S. Liu, Z. Liu and W. Chen, *J. Energy Chem.*, 2024, **94**, 1.

263 M. Khenkin, H. Köbler, M. Remec, R. Roy, U. Erdil, J. Li, N. Phung, G. Adwan, G. Paramasivam, Q. Emery, E. Unger, R. Schlatmann, C. Ulbrich and A. Abate, *Energy Environ. Sci.*, 2024, **17**, 602.

264 Y. Yun, Q. Chang, J. Yan, Y. Tian, S. Jiang, W. Wei, S. Li, Y. Guo, J. Yin, J. Li, M. Chen, K. Huang, C. Li and R. Zhang, *Sci. Adv.*, 2025, **11**, eadp3112.

265 X. Lu, K. Sun, Y. Wang, C. Liu, Y. Meng, X. Lang, C. Xiao, R. Tian, Z. Song, Z. Zhu, M. Yang, Y. Bai and Z. Ge, *Adv. Mater.*, 2024, **36**, 2400852.

266 V. Paraskeva, M. Norton, A. Livera, A. Kyprianou, M. Hadjipanayi, E. Peraticos, A. Aguirre, S. Ramesh, T. Merckx, R. Ebner, T. Aernouts, A. Krishna and G. E. Georghiou, *ACS Energy Lett.*, 2024, **9**, 5081.

267 A. Farooq, I. M. Hossain, S. Moghadamzadeh, J. A. Schwenzer, T. Abzieher, B. S. Richards, E. Klampaftis and U. W. Paetzold, *ACS Appl. Mater. Interfaces*, 2018, **10**, 21985.

This journal is © The Royal Society of Chemistry 2025

J. Mater. Chem. A, 2025, **13**, 32964–33011 | **33011**